CHARGE STATE DEPENDENCE OF M-SHELL X-RAY PRODUCTION IN $_{67}$Ho BY 2-12 MeV CARBON IONS

DISSERTATION

Presented to the Graduate Council of the

University of North Texas in Partial

Fulfillment of the Requirements

For the Degree of

DOCTOR OF PHILOSOPHY

By

Hsueh-Li Sun, B.S., M.A.

Denton, Texas

August, 1994

CHARGE STATE DEPENDENCE OF M-SHELL X-RAY PRODUCTION IN $_{67}$Ho BY 2-12 MeV CARBON IONS

DISSERTATION

Presented to the Graduate Council of the

University of North Texas in Partial

Fulfillment of the Requirements

For the Degree of

DOCTOR OF PHILOSOPHY

By

Hsueh-Li Sun, B.S., M.A.

Denton, Texas

August, 1994

Sun, Hsueh-Li, Charge State Dependence of M-shell X-ray Production in $_{67}$Ho by 2-12 MeV Carbon Ions. Doctor of Philosophy (physics), August, 1994, 114 pp., 6 tables, 21 illustrations, bibliography, 156 titles.

The charge state dependence of M-shell x-ray production cross sections of $_{67}$Ho bombarded by 2-12 MeV carbon ions with and without K-vacancies are reported. The experiment was performed using an NEC 9SDH-2 tandem accelerator at the Ion Beam Modification and Analysis Laboratory of the University of North Texas. The high charge state carbon ions were produced by a post-accelerator stripping gas cell. Ultra-clean holmium targets were used in ion-atom collision to generate M-shell x rays at energies from 1.05 to 1.58 keV. The x-ray measurements were made with a windowless Si(Li) x-ray detector that was calibrated using radiative sources, particle induced x-ray emission (PIXE), and the atomic field bremsstrahlung (AFB) techniques.

Experimental results are compared to the predictions of the first Born and ECPSSR theories using single-hole fluorescence yields. The theories include two ionization mechanisms, direct ionization (DI) of the target electron to the continuum and electron capture (EC) from the target to the projectile. The first Born theory describes the DI by the plane wave Born approximation (PWBA) and electron capture (EC) by the Oppenheimer-Brinkman-Kramers treatment of Nikolaev (OBKN). The ECPSSR theory accounts for the energy loss (E) and Coulomb deflection (C) of the projectile while passing the target atom as well as the perturbed stationary states (PSS) and the relativistic effects of the target electron during interaction with the projectile.

The electron capture cross sections as well as direction ionization cross sections can be extracted from the charge state dependence of the x-ray production cross section. The first Born theory overpredicts all the data for the total M-shell x-ray production cross sections and the electron capture cross sections while giving a fair agreement to the direct ionization cross sections. The first Born theory overpredicts the electron capture measurements by at least a factor of 16. The ECPSSR theory agrees well with the total M-shell x-ray production cross sections for 6-12 MeV carbon ions with charge state 3+ and 4+, but overpredicts the results of charge state 5+ and 6+ and all of the data at energies 2 and 4 MeV. The ECPSSR theory also overpredicts all the electron capture cross sections by a factor of 4-10 while it underestimates all the direct ionization cross sections by 20% to 76%.

ACKNOWLEDGEMENTS

This project would not have been possible without the help of many individuals. I would like to thank my wife Ju-Lin Feng for continuous support over the years. I am very grateful to R.B. Escue, Jianyue Jin, and Dwight Maxson for their technical assistance. The project was supported by several institutes including the National Science Foundation in Grants No. DMR-8812331, INT-8917946 and ECD-9003099, the Office of Naval Research in Grants No. N00014-89-J-1309, N00014-89-J-1344, N00014-90-1691, and N00014-91-J-1785, Texas Instruments Incorporated, Texas Utilities Electric Inc., International Digital Modeling Corp., North Texas Research Institute, and the Robert A. Welch Foundation.

TABLE OF CONTENTS

LIST OF TABLES

LIST OF TABLES--*Continued*

Table page

LIST OF ILLUSTRATIONS

LIST OF ILLUSTRATIONS--*Continued*

Figure page

LIST OF ILLUSTRATIONS--*Continued*

Figure page

CHAPTER 1

INTRODUCTION

Atomic inner-shell ionization of target atoms caused by the impact of charged particles has been the subject of extensive studies for the past decades. These studies not only have proven important in understanding the fundamental processes behind the often complicated mechanics involved in ion-atom collisions, but they also have applications in astrophysics, plasma physics, solid state physics, and chemical reactions [1]. Inner-shell ionization studies also provide a powerful tool for quantitative analysis of elemental, chemical, and structural composition of bulk and surface materials [2].

X-rays that are generated by inner-shell ionization are conventionally measured with Si(Li) x-ray detectors. These detectors classically have beryllium entrance windows that preclude the measurement of x-rays below 1 keV. For this reason, a search of the literature will reveal that very few ion-atom collision studies have been made in this 1 keV binding energy region. Several years ago a windowless Si(Li) x-ray detector was installed on the x-ray chamber beam line of 3 MV tandem accelerator at the University of North Texas. With this windowless detector it is possible to measure x-ray energies down to 185 eV. For the present study this detector was used to measure M-shell x rays (1.05 to 1.58 keV) from holmium targets that were bombarded with carbon ions. The purpose of this work is to test the current inner-shell ionization theories for this projectile-target

pair. In particular the projectile charge state dependence was studied for carbon ions with charge states 3+ to 6+. These measurements were made for a wide variety of holmium target thickness to establish the single collision realm. From the experimental measurements it was possible to extract the electron capture contribution to the interaction and compare these measurements to the theory.

In the ion-atom collision process, swift heavy ions excite and ionize the electrons of target atoms and generate vacancies. When filling these vacancies by electron transitions from higher atomic levels, characteristic x-rays (radiative) and Auger electrons (non-radiative) are generated. By measuring either the x-rays or the emitted Auger electrons, many details of the atomic excitation can be studied. The inner-shell ionization cross sections, defined as the ratio of the x-ray production cross section to the fluorescence yield that is the probability of an x-ray being emitted per vacancy, can be easily determined with high resolution Si(Li) x-ray detector measurements. In relating the inner-shell ionization to the x-ray production, single-hole fluorescence yields [3] are mostly used instead of multiple ionization fluorescence yields [4]. The Ion Beam Modification and Analysis Laboratory (IBMAL) at the University of North Texas (UNT) has, in fact, been one of the main contributors in this field.

From a theoretical point of view, three basic mechanisms may cause vacancies to be produced in the target atom during ion-atom collisions. The first one is direct ionization (DI) which occurs when projectile ions directly knock out the inner-shell electrons of the target into the continuum. This mechanism is dominant at high ion velocity, $v_1 >> v_{2e}$, and for $Z_1 << Z_2$, where Z_1 and Z_2 are the atomic numbers of the projectile and target atom, and v_1 and v_{2e} are the velocities of projectile ion and target inner-shell electron, respectively [5, 6]. The

second mechanism is electron capture (EC), in which an inner-shell electron is captured from the target atom into a vacant bound state of the incident ion. This process becomes important at lower ion velocity, $v_1 \leq v_{2e}$, and for $Z_1 \leq Z_2$ [7, 8]. In the third mechanism for slow symmetrical ion-atom collisions where $v_1 << v_{2e}$ and $Z_1 \approx Z_2$, the vacancy production is caused primarily by electron promotion. In this process, electronic excitations are due to the formation of quasi-molecular orbitals caused by the inter-penetrating electron clouds of the projectile ions and the target atoms [9-14].

Numerous experiments over the past few years have given rise to acute interest on the part of atomic theorists. At this point in time the theory, in general, is fairly well understood for some collision systems. For the DI, early theoretical calculations of direct Coulomb ionization cross sections were made through the binary-encounter approximation (BEA) [15-17], the semiclassical approximation (SCA) [18], and the plane-wave Born approximation (PWBA) [5, 6, 19].

In the BEA, ionization cross sections are obtained by treating the colliding particles classically. The BEA has evolved from the "impulse approximation" developed by Bohr [20, 21] to describe ionization occurring by the direct exchange of energy in the collision of a charged particle with the bound electron. This model gives a qualitative description of the experimental data, but has proven to be insufficient for quantitative comparison [1].

The SCA model was first formulated by Bang and Hansteen [18] to describe the inner-shell ionization processes caused by light ion impact. In the SCA model the projectile is assumed to move along a classical trajectory while the electron transition is treated quantum-mechanically. The deflection of the

projectile by the Coulomb field of the target nucleus has also been considered in the calculation of K-shell ionization of atoms [22].

By using the plane wave Born approximation (PWBA), Bethe [19] was the first to give a quantum-mechanical description of the excitation and ionization processes. Later, Merzbacher [5] extended this model and gave a complete picture of this process. In the PWBA, both the projectile and target electrons are expressed quantum-mechanically, and the Coulomb interaction between the projectile and target electrons is assumed to produce a small perturbation of target-atomic states. The PWBA is equivalent to the time-dependent SCA under assumption of a straight-line trajectory and small energy loss of the projectile. As long as their atomic wave functions are identical, both methods give the same DI cross sections. These methods have been fairly successful for high relative velocity colliding systems with $Z_1/Z_2 << 1$.

At low projectile velocities, the simple first-order Born theories, such as the SCA and the PWBA, become invalid. In order to modify these theories, one needs to take the following phenomena into account. (1) The increase in the binding energy of the inner-shell electrons due to penetration of the projectile inside the inner-shell during the collision reduces the probability for ionization. (2) The deflection of the projectile by the Coulomb field of the target atom increases the distance from projectile to the target electron and therefore reduces the ionization probability. (3) The polarization of the inner-shell electron wave function due to the projectile, which keeps the projectile and target electron in contact longer, increases the ionization probability. (4) The energy loss of the projectile reduces the ionization probability if the $v_1 < v_{2e}$. (5) The relativistic effect of the target electron increases the mass of the electron and reduces the

ionization probability. Brandt, Basbas, Lapicki, and others [7, 8, 23-27] incorporated all these effects to the ionization process to develop the so-called ECPSSR theory, where the (E) stands for the energy loss effect [23, 28], the (C) Coulomb deflection effect [29], the (PSS) for the binding energy and polarization effects caused by the perturbed stationary state [29], and the (R) is the relativistic effect [23, 28]. For these modification, the screened non-relativistic hydrogenic wavefunctions are used for calculation.

In the ECPSSR theory, the inner-shell ionization can be obtained by multiplying data from the existing universal function for the PWBA cross sections [30] by appropriate correction factors as mentioned above. The ECPSSR theory has been widely used to calculate K-shell ionization cross sections for light ions and has proved to be in good agreement with the experimental results for the region, $Z_1=1$ and 2, $6\leq Z_2\leq 92$, and $0.05<v_1/v_{2e}<5$ [31-33].

At the present time, the inner-shell ionization caused by the impact of swift light ions appears to be fairly well established for asymmetric collisions [31]. However, there is still a lack of experimental results for heavy ion-atom collisions where electron capture (EC) becomes more important.

The projectile electron capture and the contributions to the target vacancy production were first studied by Oppenheimer [34]. Brinkman and Kramers (OBK) [35] then applied quantum mechanics to EC. The OBK approximation describes the transition of an electron from a hydrogenic target to hydrogenic states of a fully stripped ion. A maximum in the EC cross section is predicted when the velocity of the ion matches the velocity of the target electron during the collision. Nikolaev (OBKN) [36] extended this model to calculate EC cross sections by utilitizing non-relativistic screened hydrogenic wavefunctions. The

PWBA together with the OBKN is referred in the present work as the first Born theory. It is this theory that is used for one comparison with the present experimental data.

Lapicki and Losonsky [7] and Lapicki and McDaniel [8] improved the OBKN formalism by incorporating the Coulomb deflection and perturbed-stationary state to low velocity ions, the second-order Born approximation to high-velocity ions, and relativistic effect term for electron capture. Thus, the prediction of the ECPSSR theory including DI and EC has been extended to the low velocity range where $Z_1/Z_2<1$, and $v_1/v_{2e}<1$. This theory has been shown to give good agreement with the measured K and L inner-shell ionization cross sections [31-33, 37, 38]. However, due to the lack of M-shell ionization measurements, the theory has yet to be tested thoroughly for the M-shell.

Fano and Lichten were the first to propose using a molecular orbital (MO) model to explain inner-shell excitation produced in heavy ion-atom collisions [9]. In this model, if the relative motion of two nuclei is much slower than the orbiting velocity of the electrons and if the perturbation potential can be comparable to the corresponding binding and the interaction energy, then the two atomic particles may be viewed as a quasi-molecule transiently formed during collision. The colliding atoms are treated as a diatomic molecule whose internuclear separation varies during the collision. An electron originally in an atomic orbital having a low principal quantum number may, when the nuclei approach, be pushed into a molecular orbital having a higher principal quantum number. Furthermore, it is possible for the electron to be left in a new excited atomic level when the nuclei separate. The pre-collision levels of these "promoted electrons" thus leave vacancies. The MO model has been confirmed

experimentally to be a major contributor to inner-shell ionization mechanisms in low velocity atomic collisions [12, 13].

Few studies have been directed to inner-shell ionization for the M-shell. The major reason for the lack of M-shell data relative to the more abundant K- and L-shell measurements is the experimental difficulty associated with these measurements. The M-shell x-rays, for $_{92}$U, are only 3 keV in energy and are lower in energy as the atomic number decreases. As was mentioned above, the conventional Si(Li) x-ray detector has a beryllium window that precludes measurements in the low energy region, hence the lack of data in the literature. The UNT laboratory has been able to resolve this experimental problem by installing a windowless Si(Li) x-ray detector in an UHV chamber. With this arrangement, x-ray energies as low as 282 eV ($_6$C-K$_\alpha$) can be measured [32, 33]. These measurements would not have been possible without the advent of the windowless Si(Li) detector.

As was explained earlier, the primary mechanisms involved in inner-shell vacancy production in energetic heavy ion-atom collisions are direct ionization (DI) and electron capture (EC). Most of the experimental measurements obtained for K-, L-, and M-shell ionization have been compared to the DI theory. This is due to the experimental difficulty in extracting the contribution of DI and EC. As a result total ionization measurement were always used to compared with the theories. By virtue of their higher energy x-rays, which are easier to measure, there is a wealth of experiments in the literature for K- and L-shell studies, for which EC contributions are considered [39-54]. The only definitive measurements for EC for the M-shell ionization were performed by our group at Oak Ridge National laboratory [43, 55-58]. The EC contribution to the ionization cross

sections can be determined by making a comprehensive study of the projectile charge state dependence of the cross sections for targets in which the single collision realm can be approximated. Our laboratory first studied the charge state dependence of inner-shell ionization cross sections for thin solid targets in 1977. For K-shell ionization, McDaniel *et al.* [39] presented a paper on $^{28}_{14}Si^{q+}$ ions incident on $_{21}Sc$, $_{22}Ti$, $_{29}Cu$, and $_{32}Ge$ targets. This work was followed by a series of others on K- and L-shell ionization measurements for a wide variety of targets and projectile charge states [40-43]. Earlier studies on charge state dependence of x-ray production were by Hopkins in 1975 [59], Gray *et al.* in 1976 [60], and Gardner *et al.* in 1977 [61]. Later studies were conducted by Tawara *et al.* in 1978 [62], Schmiedekamp *et al.* in 1979 [63], and Gray *et al.* in 1979 [64].

For the work in this thesis, $^{12}_{6}C^{q}$ ions (q=2+−6+) in the energy range from 2 to 12 MeV were used to bombard a thin $_{67}Ho$ target. This $_{67}Ho$ target was 0.34 $\mu g/cm^2$ which makes it thin enough to be in the single collision realm which is necessary for the extraction of EC cross sections. As was mentioned above measurements in this thesis are the first to test the EC theory as well as the DI theory for M-shell ionization in the range, $Z_1/Z_2=0.09$ and $0.17 \leq v_1/v_{2e} < 0.42$.

In addition to the present work, two papers [65, 66] have already been published by the author of this thesis on the energy dependence of M-shell ionization for incident protons and alpha particles bombarding eleven rare-earth targets. In these papers, the techniques for producing contaminant free rare-earth targets were discussed [67-69]. Considerable experience was obtained in producing thin rare-earth targets suitable for measurement of 0.6 to 1.8 keV x-rays.

In chapter 2, a review of the quantum and classical mechanical scattering

theories for DI as well as EC will be given. Details of the experimental procedures including a windowless Si(Li) x-ray detector efficiency determination and target preparation are given in chapter 3. In chapters 4 and 5, experimental measurements will be analyzed and the results will be presented and discussed, respectively. In the last chapter, conclusions concerning M-shell direct ionization as well as electron capture will be drawn from proceeding chapters.

CHAPTER 2

THEORY

The theoretical models for inner-shell ionization has been developed by using classical- and quantum-mechanical methods. In this chapter, the quantum mechanical scattering theories, such as the first Born and the ECPSSR, are described. Within the first Born approximation, the PWBA (Plane Wave Born Approximation) is used to calculate direct ionization (DI), and the OBKN (Oppenheimer-Brinkman-Kramers-Nikolaev) approximation is described for electron capture (EC). The ECPSSR theory is described chronologically and improves the first Born approximation by including the modifications for energy loss (E) of the projectile, Coulomb deflection (C) of projectile path, binding-polarization effects in the perturbed stationary states (PSS) of the target electron, and relativistic (R) effect of the target electron. Also mentioned in this section are the classical methods that include the SCA (semi-classical approximation), which is used for a correction factor in the ECPSSR theory, and the BEA (binary-encounter approximation). Finally, some views for improving the electron capture theory will be presented.

2.1 Quantum Mechanical Scattering Theory

The quantum method is used to evaluate the transition matrix elements by using the appropriate set of Hamiltonians and wave functions for the physical

system [70-72]. For example, the Hamiltonian of the colliding ion-atom system can be described by the form

$$H = H_{ion} + H_{atom} + V, \tag{2.1}$$

where H_{ion} and H_{atom} are the respective Hamiltonians of ion and atom, and V is their interaction potential. The initial wave function, Ψ_i, and final wave function, Ψ_f, of the system are used to define the transition matrix as

$$T_{fi} = \langle \Psi_f | V | \Psi_i \rangle \tag{2.2}$$

The differential cross section (in barns) can then be written as [5]

$$d\sigma = \left(\frac{\mu}{2\pi\hbar^2}\right)^2 \frac{v_f}{v_i} |T_{fi}|^2 d\Omega, \tag{2.3}$$

where v_i and v_f are the initial and final velocity of the incident particle, respectively; μ is the reduced mass (in amu) of the interacting particles in the system and $d\Omega$ is the element of solid angle into which the projectile is scattered.

2.2 The First Born Theory - PWBA and Direct Ionization

In the plane wave Born approximation (PWBA), the velocity of the projectile is assumed to be high enough that distortion of its wave function by the target electron can be neglected. Similarly, external perturbations on the target electron are comparatively weak and the only interaction responsible for inner-shell vacancy production (ionization) is assumed to be the Coulomb potential between the target electron and the incident projectile [5]. Therefore, by neglecting the excitation of the electron to unoccupied orbitals, the initial and

final states of the atom are described in terms of the transition of a electron from its initial bound state to the continuum state [5].

Direct ionization is applicable to a projectile incident upon an electron that is bound in the S state of an atomic system. The projectile of mass M_1 and charge Z_1 is assumed to be an incident plane wave while the electron is in a target atom of mass M_2 and charge Z_2. This interaction potential is given as

$$V = \frac{Z_1 e^2}{|\boldsymbol{R}-\boldsymbol{r}|}, \tag{2.4}$$

where $\boldsymbol{r}$ is the position vector of the relevant atomic electron and $\boldsymbol{R}$ is the position vector pointing from the atom to the projectile. The transition matrix defined in equation (2.2) can be written as

$$T_{fi}^{PWBA} = \int\int \Psi_f^*(\boldsymbol{R},\boldsymbol{r}) \frac{Z_1 e^2}{|\boldsymbol{R}-\boldsymbol{r}|} \Psi_i(\boldsymbol{R},\boldsymbol{r})\, d\boldsymbol{r} d\boldsymbol{R}, \tag{2.5}$$

where $\Psi_i(\boldsymbol{R}, \boldsymbol{r})$ is the initial state of the system, given as

$$\Psi_i(\boldsymbol{R},\boldsymbol{r}) = e^{i\boldsymbol{k}_i \cdot \boldsymbol{R}}\, \Phi_i(\boldsymbol{r}), \tag{2.6}$$

and $\Psi_f(\boldsymbol{R}, \boldsymbol{r})$ is the final state, given as

$$\Psi_f(\boldsymbol{R},\boldsymbol{r}) = e^{i\boldsymbol{k}_f \cdot \boldsymbol{R}}\, \Phi_f(\boldsymbol{r}); \tag{2.7}$$

Φ_i and Φ_f are the respective initial and final wavefunctions for the target electron; within the incident and scattered plane waves, the wave numbers $\boldsymbol{k}_i$ and $\boldsymbol{k}_f$ are related to the initial and final momenta of the projectile by $\boldsymbol{P}_i = \hbar\, \boldsymbol{k}_i$ and $\boldsymbol{P}_f = \hbar\, \boldsymbol{k}_f$. After taking the total wavefunctions into account, the transition matrix can be

written as

$$T_{fi}^{PWBA} = \int\int \Phi_f^*(\boldsymbol{r}) \frac{Z_1 e^2 \; e^{i(\boldsymbol{k}_f - \boldsymbol{k}_i)\cdot \boldsymbol{R}}}{|\boldsymbol{R}-\boldsymbol{r}|} \Phi_i(\boldsymbol{r}) \, d\boldsymbol{r} d\boldsymbol{R} \tag{2.8}$$

The momentum transfer is given as

$$\Delta \boldsymbol{p} = \hbar \boldsymbol{q} = \hbar(\boldsymbol{k}_i - \boldsymbol{k}_f). \tag{2.9}$$

After replacing $(\boldsymbol{k}_i - \boldsymbol{k}_f)$ by $\boldsymbol{q}$ and performing the integration over $\boldsymbol{R}$, equation (2.8) becomes

$$T_{fi}^{PWBA} = -\frac{4\pi Z_1 e^2}{q^2} \int \Phi_f^*(\boldsymbol{r}) e^{i\boldsymbol{q}\cdot\boldsymbol{r}} \Phi_i(\boldsymbol{r}) \, d\boldsymbol{r}. \tag{2.10}$$

By defining the "atomic form factor" as

$$F_{fi}(\boldsymbol{q}) = \int \Phi_f^*(\boldsymbol{r}) e^{i\boldsymbol{q}\cdot\boldsymbol{r}} \Phi_i(\boldsymbol{r}) \, d\boldsymbol{r} = \left\langle \Phi_f(\boldsymbol{r}) \middle| e^{i\boldsymbol{q}\cdot\boldsymbol{r}} \middle| \Phi_i(\boldsymbol{r}) \right\rangle, \tag{2.11}$$

the differential cross section given in the equation (2.3) can be written as

$$d\sigma_{fi}^{PWBA} = \left(\frac{2Z_1 e^2 \mu}{\hbar^2} \right)^2 \frac{v_f}{v_i} \left[\frac{F_{fi}(\boldsymbol{q})}{q^2} \right]^2 d\Omega, \tag{2.12}$$

where

$$\mu = \frac{M_1 M_2}{(M_1 + M_2)}. \tag{2.13}$$

The scattering angle, θ, is related to the momentum transfer in the following way:

$$q^2 = \boldsymbol{q}\cdot\boldsymbol{q} = k_i^2+k_f^2-2\boldsymbol{k}_i\cdot\boldsymbol{k}_f = k_i^2+k_f^2-2k_ik_f\cos\theta. \tag{2.14}$$

Differentiating equation (2.14) gives

$$qdq = k_ik_f\sin\theta\, d\theta. \tag{2.15}$$

Using equations (2.15) and (2.12) and knowing the differential solid angle ($d\Omega=\sin\theta d\theta d\phi$), the differential cross section then becomes

$$d\sigma_{fi}^{PWBA} = \left(\frac{2Z_1e^2}{\hbar v_i}\right)^2 \frac{|F_{fi}(\boldsymbol{q})|^2}{q^3}\, dqd\phi. \tag{2.16}$$

The complete expression for the ionization cross section can be obtained by summing over all initially filled substates. To account for the double occupancy of each orbital substates, equation (2.16) is necessarily multiplied by 2. This is done because the spin enters as a statistical factor, 2j+1, where j is the total angular momentum of the *S*-shell electron. The spin generally plays no dynamic role in heavy ion collisions. Thus, the cross section may be expressed as

$$d\sigma_{fi}^{PWBA} = \frac{16\pi Z_1^2e^4}{\hbar^2v_i^2q^3}\, |F_{fi}(\boldsymbol{q})|^2\, dq. \tag{2.17}$$

Using a hydrogenic wave function for the electron in the initial state, *S*, and a continuum wave function for the final state of the electron, the form factor may be evaluated for an energy transfer between ε and $\varepsilon+d\varepsilon$, and the cross section becomes

$$d\sigma_{\varepsilon,S}^{PWBA} = \frac{16\pi Z_1^2 e^4}{\hbar^2 v_i^2 q^3} |F_{\varepsilon,S}(q)|^2 \, dq d\varepsilon. \tag{2.18}$$

The energy transfer, ε, is given as

$$\varepsilon = E_{2S} + T, \tag{2.19}$$

where E_{2S} is the observed ionization potential (the observed binding energy) of the electron in the initial state, S, (subscript 2 represents the target atom) and T is the kinetic energy of the ejected electron.

The PWBA calculation of the cross section depends upon the exact wave functions used for the form factor. Thus, non-relativistic hydrogenic wave functions are used with screened atomic nuclei [5, 73-75]. The screening by inner-shell electrons reduces the target charge, Z_2, to the effective charge, Z_{2S}, seen by an electron in the S state. The atomic number, Z_2, has been modified by Slater [76] to give the following Z_{2S}:

$Z_{2K} = Z_2 - 0.3$, for the K-shell state;

$Z_{2L} = Z_2 - 4.15$, for the L-shell state;

$Z_{2M} = Z_2 - 11.25$, for the M1-, M2-, and M3-subshell states;

$Z_{2M} = Z_2 - 21.15$, for the M4- and M5-subshell states.

By integrating equation (2.18) over all possible momentum and energy transfer, the ionization cross section becomes

$$\sigma_{\varepsilon,S}^{PWBA} = \frac{16\pi Z_1^2 e^4}{\hbar^2 v_i^2} \int_{q_{min}}^{q_{max}} \frac{dq}{q^3} \int_{\varepsilon_{min}}^{\varepsilon_{max}} d\varepsilon |F_{\varepsilon,S}(q)|^2. \tag{2.20}$$

The limits of the momentum transfer integration may be judged from equation

(2.14) as $q_{min}=k_i-k_f$ and $q_{max}=k_i+k_f$. These limits may be expressed as

$$q_{\min} = q_0 = \frac{E_{2S}}{\hbar v_i} = \frac{\hbar\omega_{2S}}{\hbar v_i} = \frac{\omega_{2S}}{v_i}, \tag{2.21}$$

and

$$q_{\max} = \infty. \tag{2.22}$$

In order to free the electron from the initial state to a continuum state, the transferred energy must be greater than the electronic binding energy, E_{2S}. Assuming $T=0$, this gives a limit to the minimum energy transfer given as

$$\varepsilon_{\min} = E_{2S} = \frac{Z_{2S}^2 R_y}{n_{2S}^2}, \tag{2.23}$$

where R_y ($=m_e v_0^2/2 = 13.6$ eV) is the Rydberg constant and n_{2S} is the principal quantum number for the target electron in the S state. When the kinetic energy of the ejected electron is very large compared to the observed ionization potential, the maximum energy transfer may be taken to be infinity.

The following reduced (dimensionless) parameters for the energy and momentum transfer are introduced:

$$W = \frac{\varepsilon}{Z_{2S}^2 R_y} \tag{2.24}$$

and

$$Q = q^2 a_{2S}^2 = q^2 \left(\frac{n_{2S}^2 a_0}{Z_{2S}} \right)^2, \tag{2.25}$$

where a_{2S} is the target electronic radius in the S state, a_0 ($=\hbar^2/m_e e^2 = 0.529\times10^{-8}$ cm) is the hydrogenic Bohr radius, m_e is the electron mass, e is the electron charge, and v_0 ($=e^2/\hbar = 2.19\times10^8$ cm/sec) is the hydrogen Bohr velocity. The ionization cross section becomes

$$\sigma_S^{PWBA} = \frac{8\pi a_0^2 Z_1^2 e^4}{Z_{2S}^2 \hbar^2 v_i^2} \int_{W_{\min}}^{\infty} dW \int_{Q_{\min}}^{\infty} \frac{dQ}{Q} |F_{W,S}(Q)|^2, \tag{2.26}$$

where

$$W_{\min} = \frac{\varepsilon_{\min}}{Z_{2S}^2 R_y} = \frac{\hbar\omega_{2S}}{Z_{2S}^2 R_y}, \tag{2.27}$$

and

$$Q_{\min} = q_{\min}^2 a_{2S}^2 = \left(\frac{\omega_{2S}}{v_i} \frac{n_{2S}^2 a_0}{Z_{2S}} \right)^2. \tag{2.28}$$

Similarly the reduced velocity is given by

$$\eta_S = \frac{1}{Z_{2S}^2} \left(\frac{v_i}{v_0} \right)^2 = \frac{m_e E_1}{\mu Z_{2S}^2 R_y} = \frac{40.32}{Z_{2S}^2} \frac{E_1(MeV)}{M_1(amu)}, \tag{2.29}$$

where E_1 is the kinetic energy of the incident projectile. The ionization cross section for the S-shell electron becomes

$$\sigma_S^{PWBA} = \frac{8\pi a_0^2 Z_1^2}{Z_{2S}^4 \eta_S} \int_{W_{\min}}^{\infty} dW\, I(\eta_S, W), \tag{2.30}$$

where

$$I(\eta_s, W) = \int_{\frac{W^2}{4\eta_s}}^{\infty} \frac{dQ}{Q^2} |F_{W,S}(Q)|^2 \tag{2.31}$$

is the excitation function for an electron receiving a reduced energy between W and $W+dW$.

The ratio of the true binding energy to the energy calculated by treating the atom as hydrogenic atom is defined as a reduced binding energy given by

$$\theta_S = \frac{\hbar\omega_{2S}\, n_{2S}^2}{Z_{2S}^2\, R_y}. \tag{2.32}$$

Using equation (2.32), the ionization cross section can be written as

$$\sigma_S^{PWBA} = \frac{8\pi a_0^2 Z_1^2}{Z_{2S}^4 \eta_S} f_S(\theta_S, \eta_S) = \frac{\sigma_{0S}}{\eta_S} f_S(\theta_S, \eta_S), \tag{2.33}$$

where

$$f_S(\theta_S, \eta_s) = \int_{\frac{\theta_S}{n_{2S}^2}}^{\infty} I(\eta_s, W) dW, \tag{2.34}$$

and

$$\sigma_{0S} = \frac{8\pi Z_1^2 a_0^2}{Z_{2S}^4}. \tag{2.35}$$

And, the direct Coulomb ionization cross section is proportional to a universal function, $\mathcal{F}_S$, which, to a good approximation, depends only on η_S/θ_S^2 [26]. The cross section is then expressed as

$$\sigma_S^{PWBA} = \frac{\sigma_{0S}}{\theta_S}\mathcal{F}_S\left(\frac{\eta_S}{\theta_S^2}, \theta_S\right) = \frac{\Pi_{2S}^2\sigma_{0S}}{2\theta_S}\mathcal{F}_S(\xi_S, \theta_S), \tag{2.36}$$

where

$$\xi_S = \frac{1}{q_o a_{2S}} = \frac{2v_i}{\theta_S v_{2S}} = \frac{2\sqrt{\eta_S}}{\theta_S}, \tag{2.37}$$

and

$$\mathcal{F}_S\left(\frac{\eta_S}{\theta_S^2}, \theta_s\right) = \frac{\theta_S}{\eta_S} f_S(\eta_S, \theta_S). \tag{2.38}$$

2.3 The First Born Theory - OBKN and Electron Capture

The electron capture process becomes important for slowly moving ions colliding with target atoms. Oppenheimer [34] was the first to study electron capture (EC) as a three body problem. By neglecting the internuclear interaction between two nuclei, he derived an analytic expression for the electron transfer between the proton-hydrogen system. Later, Brinkman and Kramers [35] used the first Born approximation to calculate this effect. They considered the Coulomb

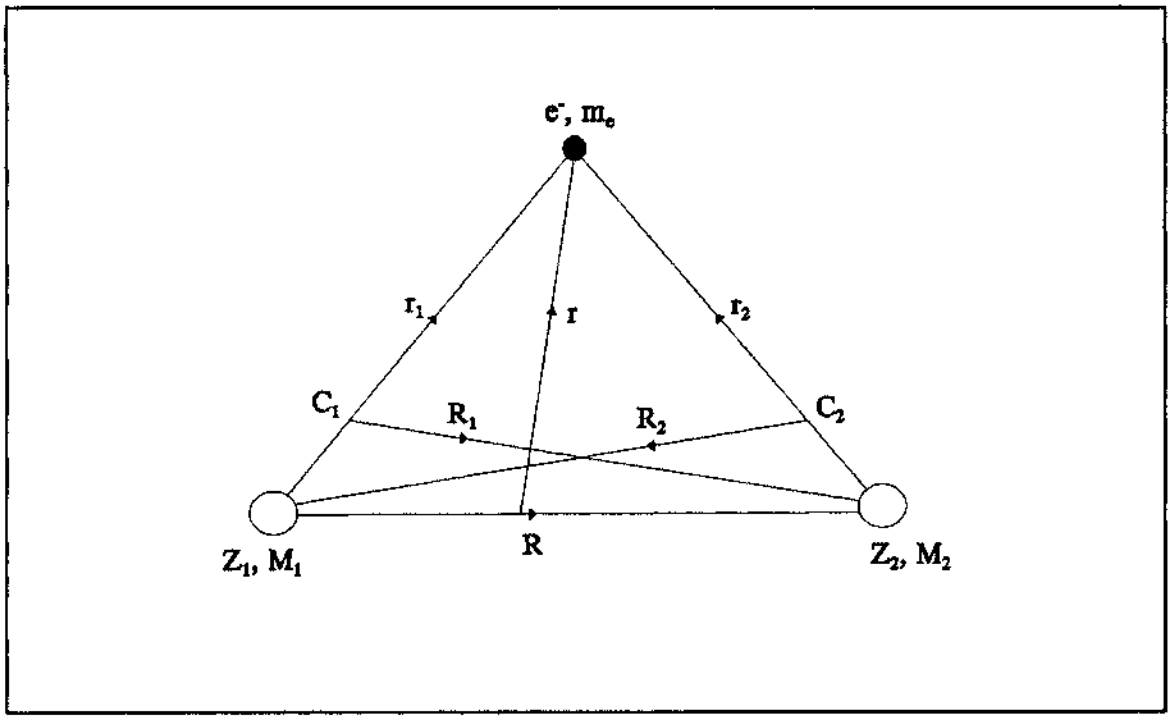

Figure 2.1 Electron capture in the OBKN approximation. The point C_2 represents the center-of-mass for the atom-electron system prior to the collision. Similarly, C_1 is the center-of-mass for the ion-electron system after capture.

attraction (i) between the target atom and its electron (before capture), and (ii) between the incident ion and the target electron (after capture). The three body problem is depicted in figure 2.1, where r_1 is the position of the electron relative to the ion, r_2 is the position of the electron relative to the target atom, and R_2 denotes the position vector between the ion and the center of mass, C_2, of the target nucleus-electron system prior to electron capture. After capture, R_1 is the position vector to the target nucleus from the center of mass, C_1, of the ion-electron system. Similarly to DI, the EC process has been evaluated using the Born approximation formalism.

Jackson and Schiff [77] have shown by perturbation theory that to first

order the nucleus-electron interaction potential can be approximated by either the interaction of the target nucleus-electron or that of the ion nucleus-electron. In the OBK approximation, the nucleus-nucleus interaction term was neglected. The Hamiltonian for this system may be expressed as in the case for direct ionization and similar to equation (2.1) where V is the ion-electron interaction potential given by

$$V = \frac{Z_1 e^2}{r_1}. \tag{2.39}$$

The initial state of the system includes a projectile of charge Z_1 and mass M_1 and an electron in the S shell of the target atom. The initial and final wave functions are defined as

$$\Psi_i = e^{i\boldsymbol{k}_i \cdot \boldsymbol{R}_2}\, \Phi_i(\boldsymbol{r}_2), \tag{2.40}$$

and

$$\Psi_f = e^{i\boldsymbol{k}_f \cdot \boldsymbol{R}_1}\, \Phi_f(\boldsymbol{r}_1), \tag{2.41}$$

where $\Phi_i(r_2)$ and $\Phi_f(r_1)$ are the respective hydrogenic wave functions of the electron in the target and the projectile atoms; the exponential terms are the plane waves for the ion with the initial momentum, $\hbar\, \boldsymbol{k}_i = \mu_i \mathbf{v}_i$, and for the ion-electron system with the momentum, $\hbar\, \boldsymbol{k}_f = \mu_f \mathbf{v}_f$, after the collision. The reduced masses, μ_i and μ_f, of the ion before and after the collision are given by

$$\mu_i = \frac{M_1(m_e+M_2)}{m_e+M_1+M_2} \tag{2.42}$$

and

$$\mu_f = \frac{M_2(m_e+M_1)}{m_e+M_1+M_2}. \tag{2.43}$$

Substituting the wave functions into equation (2.2), the transition matrix becomes

$$T_{fi}^{OBK} = \iint e^{-i\boldsymbol{k}_f\cdot\boldsymbol{R}_1}\,\Phi_f^*(\boldsymbol{r}_1)\frac{Z_1e^2}{r_1}\Phi_i(\boldsymbol{r}_2)\;e^{i\boldsymbol{k}_i\cdot\boldsymbol{R}_2}\,d\boldsymbol{R}_2d\boldsymbol{r}_2. \tag{2.44}$$

From the figure 2.1,

$$\boldsymbol{R}_2 = \left(\frac{M_2}{m_e+M_2}\right)\boldsymbol{r}_2 - \boldsymbol{r}_1 \tag{2.45}$$

and

$$\boldsymbol{R}_1 = \left(\frac{M_1}{m_e+M_1}\right)\boldsymbol{r}_1 - \boldsymbol{r}_2. \tag{2.46}$$

Inserting equations (2.45) and (2.46) into equation (2.44), the transition matrix becomes

$$T_{fi}^{OBK} = \int e^{-i\boldsymbol{B}\cdot\boldsymbol{r}_1}\,\Phi_f^*(\boldsymbol{r}_1)\frac{Z_1e^2}{r_1}d\boldsymbol{r}_1\int e^{i\boldsymbol{A}\cdot\boldsymbol{r}_2}\,\Phi_i(\boldsymbol{r}_2)d\boldsymbol{r}_2, \tag{2.47}$$

where

$$\boldsymbol{A} = \boldsymbol{k}_i - \left(\frac{M_2}{m_e+M_2}\right)\boldsymbol{k}_f \tag{2.48}$$

and

$$\boldsymbol{B} = \left(\frac{M_1}{m_e+M_1}\right)\boldsymbol{k}_i - \boldsymbol{k}_f. \tag{2.49}$$

The wave function of the electron, Φ_f, must satisfy the Schrödinger equation

$$\left[\frac{-\hbar^2}{2\mu_f}\nabla_{r_1}^2 + \frac{Z_1 e^2}{r_1}\right]\Phi_f = \epsilon_f \Phi_f, \tag{2.50}$$

where ϵ_f is the observable energy of the electron in the ion. Substituting equation (2.50) into (2.47) and integrating by parts twice yields

$$T_{fi}^{OBK} = -\left(\frac{\hbar^2 B^2}{2\mu_f}+\epsilon_f\right)\int e^{-i\boldsymbol{B}\cdot\boldsymbol{r}_1}\Phi_f^*(\boldsymbol{r}_1)d\boldsymbol{r}_1\int e^{i\boldsymbol{A}\cdot\boldsymbol{r}_2}\Phi_i(\boldsymbol{r}_2)d\boldsymbol{r}_2. \tag{2.51}$$

Noting the Fourier transforms of the above equation, the transition matrix becomes

$$T_{fi}^{OBK} = -(2\pi)^6\left(\frac{\hbar^2 B^2}{2\mu_f}+\epsilon_f\right)\Phi_i(\boldsymbol{A})\Phi_f^*(\boldsymbol{B}). \tag{2.52}$$

The OBK result [35] will be obtained when the transition matrix in equation (2.52) is substituted into the equation (2.3). This calculation is valid for

a single electron transfer to a particular shell of the ion. Nikolaev [36] generalized the OBK calculation to all projectile-target combinations (Z_1, $Z_2 \geq 1$). He used non-relativistic screened hydrogenic wave functions and observed electron binding energies for the OBKN approximation to calculate the EC contribution. By summing over all initial and final quantum states in equation (2.52), Nikolaev obtained the following scattering amplitude

$$|T_{fi}^{OBKN}|^2 = \sum_n \sum_l \sum_m (2\pi)^{12} \left(\frac{\hbar^2 B^2}{2\mu_f} + \epsilon_f \right)^2 |\Phi_i(\boldsymbol{A})|^2 |\Phi_f^*(\boldsymbol{B})|^2. \tag{2.53}$$

For a given principal quantum number, n_S, using hydrogenic wave functions for the summation over orbital and magnetic quantum numbers, the following expression was obtained earlier by May [78]:

$$\sum_{l=0}^{n-1} \sum_{m=-l}^{l} |\Phi_{nlm}(\boldsymbol{q})|^2 = \frac{2^6 \pi \left(\frac{Z_S}{n_S a_0} \right)^5}{\left[q^2 + \left(\frac{Z_S}{n_S a_0} \right)^2 \right]^4}. \tag{2.54}$$

Substituting equation (2.54) into equation (2.53) and performing the appropriate summations for the probability of an electron transition from the S shell of the target atom to the S' shell of the ion, the scattering amplitude becomes

$$|T_{SS'}^{OBKN}|^2 = \frac{2^{12} \pi^2 n_{2S}^2 n_{1S'}^2 \left(\frac{Z_{1S'}}{n_{1S'} a_0} \right)^5 \left(\frac{Z_{2S}}{n_{2S} a_0} \right)^5 \left[\frac{\hbar^2 B^2}{2m_e} + \epsilon_f \right]^2}{\left[B^2 + \left(\frac{Z_{1S'}}{n_{1S'} a_0} \right)^2 \right]^4 \left[A^2 + \left(\frac{Z_{2S}}{n_{2S} a_0} \right)^2 \right]^4}, \tag{2.55}$$

where n_{2S} and $n_{1S'}$ are the principal quantum numbers of the S shell in the target atom and the S' shell in the ion, respectively. The binding energy of a hydrogenic electron in the ion can be given as

$$\epsilon_f = E_{1S'} = \frac{m_e v_{1S'}^2}{2} = \frac{m_e Z_{1S'}^2 e^4}{2n_{1S'}^2 \hbar^2}, \tag{2.56}$$

where $v_{1S'}$ is the orbital velocity of the electron in the ion. After inserting equation (2.55) into (2.3), the differential cross section for EC is expressed as

$$d\sigma = \left(\frac{\mu}{2\pi\hbar^2}\right)^2 \left(\frac{v_f}{v_i}\right) \frac{2^{10}\pi^2 n_{2S}^2 n_{2S'}^2 \left(\frac{\hbar^2}{m_e}\right)^2 \left(\frac{Z_{1S'}}{n_{1S'} a_o}\right)^5 \left(\frac{Z_{2S}}{n_{2S} a_0}\right)^5}{\left[B^2 + \left(\frac{Z_{1S'}}{n_{1S'} a_0}\right)^2\right]^2 \left[A^2 + \left(\frac{Z_{2S}}{n_{2S} a_0}\right)^2\right]^4} d\Omega \tag{2.57}$$

The momenta in equation (2.48) and (2.49) may be expanded to give

$$A^2 = \left[\frac{(E_{1S'} - E_{2S})}{\hbar v_i} + \frac{m_e v_i}{2\hbar}\right]^2 + 4\mu^2 v_i^2 \frac{\sin^2\theta}{2}, \tag{2.58}$$

and

$$B^2 = \left[\frac{(E_{1S'} - E_{2S})}{\hbar v_i} - \frac{m_e v_i}{2\hbar}\right]^2 + 4\mu^2 v_i^2 \frac{\sin^2\theta}{2}. \tag{2.59}$$

Substituting equations (2.58)-(2.59) and the relation $1/a_0 = m_e e^2/\hbar^2 = v_0 m_e/\hbar$ into equation (2.57), the OBKN cross section for an electron transition from the initial state, S, in the target atom to a final bound state, S', in the incident ion is given as

$$\sigma_{EC-SS'}^{OBKN} = \frac{2^9\pi a_0^2}{5}\left(\frac{n_{2S}n_{1S'}}{v_i}\right)^2\left(\frac{v_{1S'}}{v_{2S}}\right)^5 \xi_{SS'}^{10}(\theta_S)\frac{\Phi_4[(1-\theta_S)\xi_{SS'}^2(\theta_S)]}{[1+(1-\theta_S)\xi_{SS'}^2(\theta_S)]^3}, \qquad (2.60)$$

where

$$\xi_{SS'}(\theta_S) = \frac{v_{2S}}{\sqrt{v_{1S'}^2+q_{SS'}^2(\theta_S)}}, \qquad (2.61)$$

and

$$q_{SS'} = \frac{1}{2}\left[v_i+\frac{(v_{2S}^2\theta_S-v_{1S'}^2)}{v_i}\right]. \qquad (2.62)$$

The quantity $q_{SS'}$ is an approximation to the minimum momentum transferred by the capture process. The function $\Phi_4(x)$ is given by

$$\Phi_4[x] \equiv \frac{5}{x}\left\{1-\frac{4}{x}\left[\left(1+\frac{1}{x}\right)^3\ln(1+x)-\left(1+\frac{1}{x}\right)^2-\frac{1}{2}\left(1+\frac{1}{x}\right)-\frac{1}{3}\right]\right\}. \qquad (2.63)$$

Equation (2.63) can be approximated to within 2% by $(1+0.3x)^{-1}$ for $x<3$, i.e., for the values of x which are available in experiments.

The cross section calculated for equation (2.60) was found to be greater than the experimental cross sections by a large factor. Briggs [79] mentioned that the first-order Born approximations does not provide the correct limit for the high-energy behavior of charge transfer. In particular, for ground state to ground state charge transfers the asymptotic first-order cross section is

$$\sigma_{B1} = \frac{2^{18}\pi Z_{1S}^5 \cdot Z_{2S}^5}{5v_i^{12}} \quad (a.u.) \tag{2.64}$$

The leading terms of the second Born approximation however provide a different limit

$$\sigma_{B2} = \sigma_{B1}\left[0.295 + \frac{5\pi v_i}{2^{11}(Z_{1S}+Z_{2S})}\right]. \tag{2.65}$$

Drisko [80] and Shakeshaft and Spruch [81] show that the second Born term dominates over the first Born term (the OBK approximation [34, 35]) at asymptotically high impact velocities. Belkić *et al.* [82] have discussed the various second order theories for charge transfer and the comparison with second Born term at asymptotically high velocities.

2.4 The ECPSSR Theory and Direct Ionization

The PWBA has been found to be fairly successful in predicting direct ionization cross sections for high projectile velocities [83]. However, the PWBA generally overpredicts the inner-shell ionization by heavy charged particles with smaller velocity (v_i). This discrepancy is caused by a number of effects that are not considered for high velocity ions. During the slow collision, the low velocity ion feels the effects of the target charge while the target electrons have time to adjust their orbits adiabatically to the presence of the ion. The ECPSSR theory was developed to include those several factors by using PWBA calculations as the basis [23-27].

Increasing Binding Energy Effects

When the projectile velocity is low, the initial state of the target electron is distorted by the presence of the projectile. In slow collisions, this effect can be thought as an effective increase in the projectile-target nuclear charge and therefore also in the binding energy of the target electron. This effect has the consequence that the electrons are temporarily more tightly-bound to the target atom, thus reducing the inner-shell ionization cross section. This binding energy effect has been treated in the perturbed stationary state (PSS) approach [26, 27].

The binding energy can be taken into account by replacing the reduced binding energy, θ_S, by $\epsilon_{2S}^{B}\theta_S$. The total binding energy factor is defined as

$$\epsilon_{2S}^{B} = 1+\frac{\Delta E_{2S}}{E_{2S}}, \tag{2.66}$$

where E_{2S} is the observed S-shell binding energy and ΔE_{2S} is the average change in the S-shell binding energy during the collision.

In first order perturbation theory, the change in the binding energy is given as

$$\Delta E_{2S} = \left\langle \Phi_i^*(r) \left| \frac{Z_1 e^2}{|\boldsymbol{R}-\boldsymbol{r}_2|} \right| \Phi_i(r) \right\rangle, \tag{2.67}$$

where R is the position vector to the target atom from the projectile and r_2 is the position of the electron relative to the target atom (see figure 2.1).

Using non-relativistic hydrogenic wavefunction, equation (2.67) can be written analytically as a function of $y=R/a_{2S}$ for the S-shell. If the projectile moves along a straight line with an impact parameter b, the average binding

energy change, ΔE_{2S}, can be evaluated at the closest internuclear distance, $R_{min}=b$, and y can be written as $y=b/a_{2S}$. The average value of ΔE_{2S} is therefore defined as

$$\Delta E_{2S} = \frac{\int_0^\infty \Delta E_{2S}(y)\left(\frac{d\sigma_S}{d\varepsilon_f}\right)_b y\,dy}{\int_0^\infty \left(\frac{d\sigma_S}{d\varepsilon_f}\right) y\,dy} = 2\left(\frac{Z_1}{Z_{2S}}\right)\frac{Z_{2s}^2 R_y}{y} g_S(y), \tag{2.68}$$

where $(d\sigma_S / d\varepsilon_f)_b$ is the S-shell ionization cross section for the impact parameter b and ε_f is the energy of the electron in the final state. The impact parameter dependent ionization cross section and a weighting function, $g_S(y)$, can be obtained from the SCA [18, 84] scattering amplitude for the S-shell ionization probability function.

Using the dimensionless quantity, ξ_S, of equation (2.37), equation (2.66) can be written as

$$\epsilon_{2S}^B = 1+\left(\frac{2Z_1}{\theta_S Z_{2S}}\right) g_S(\xi_S). \tag{2.69}$$

When the binding effect is included, the cross section then becomes

$$\sigma_S^{PWBA\text{-}B} = \sigma_S^{PWBA}(\eta_S, \epsilon_{2S}^B \theta_S). \tag{2.70}$$

Polarization Effects

When the projectile is outside of the orbital radius of the target inner-shell electron, the positive charge of the projectile tends to draw the target electron away from its nucleus. This process is referred to as the polarization effect. The

polarization effect is important for medium and high energy projectiles, where collisions with large impact parameters play a dominant role. The polarization effect increase the ionization cross section because the electron and the ion are in contact longer.

Basbas *et al.* [27, 29] estimated the polarization effect in the PSS approximation. The unperturbed initial electron state is expressed by an isotropic harmonic oscillator and the energy transfer is calculated as a function of impact parameter, using classical [85] and quantum-mechanical methods [86]. The potential between the ion and the electron is given and expanded in a Taylor series as

$$V(t) = -\frac{Z_1 e^2}{|\boldsymbol{r}-\boldsymbol{R}(t)|} = -Z_1 e^2\left\{\frac{1}{R(t)}+\frac{\boldsymbol{r}\cdot\boldsymbol{R}(t)}{R^3(t)}+\frac{1}{2}\left[\frac{3\boldsymbol{r}\cdot\boldsymbol{R}(t)}{R^5(t)}-\frac{r^2}{R^3(t)}\right]+\cdots\right\}. \quad (2.71)$$

The Hamiltonian of the system can be defined as

$$\begin{aligned} H &= H_0+V_1+V_2 \\ &= \left(\frac{p^2}{2\mu_e}+\frac{\mu_e\omega^2 r^2}{2}\right)+\left[\frac{-Z_1 e^2 r}{R^2}P_1(\boldsymbol{r}\cdot\boldsymbol{R})\right]+\left[\frac{-Z_1 e^2 r^2}{R^3}P_2(\boldsymbol{r}\cdot\boldsymbol{R})\right], \end{aligned} \quad (2.72)$$

where H_0 is the unperturbed harmonic oscillator Hamiltonian; V_1 and V_2 are the respective dipole and quadrupole terms of equation (2.71) for the perturbation to the Hamiltonian, which can be expressed in terms of spherical polar coordinates and the Legendre polynomials, $P_1(\boldsymbol{r}\cdot\boldsymbol{R})$ and $P_2(\boldsymbol{r}\cdot\boldsymbol{R})$.

The transition amplitude from the ground state to a state designated by quantum number *nlm* is then given by

$$T_{nlm} = -\frac{i}{\hbar}\int_{-\infty}^{\infty} dt \langle nlm|\, V'(t)\,|000\rangle e^{-i\omega_{n0}t} - \frac{1}{\hbar^2}\int_{-\infty}^{\infty} dt \int_{-\infty}^{t} dt' \sum_{n'l'm'} \langle nlm|\, V'(t)\,|n'l'm'\rangle \times \langle n'l'm'|\, V'(t)\,|nlm\rangle e^{i\omega_{nl,n'l'}t + i\omega_{n'l'00}t}, \tag{2.73}$$

where $V'(t)=V_1+V_2$ and $\hbar\omega_{nl,n'l'}=E_{nlm}- E_{n'l'm'}$.

The transition probability, $|T_{nlm}|^2$, caused by the perturbation is limited by the selection rules for the dipole and quadrupole transitions. Similarly to the PWBA method for calculating the ionization cross section, the dipole transition will yield a probability proportional to Z_1^2. The dipole-quadruple interference term related to the oscillator model will be proportional to Z_1^3.

After correcting for the polarization effect [27], the cross section may be written as

$$\sigma_S^{PWBA-P} = \sigma_S^{PWBA} + \int d\omega\, s_k(\omega_{2S}) \left[2\pi \int_0^{\infty} P_3(\omega_{2S}, b)\, b\, db \right] = \sigma_S^{PWBA} + \int d\omega\, s_k(\omega_{2S}) \left[\frac{4\pi (Z_1 e^2)^3}{\hbar m_e^2 v_i^5} I\left(\frac{\omega_{2S} a_\omega}{v_i} \right) \right], \tag{2.74}$$

where $\hbar\omega$ is the energy transferred, $s_k(\omega_{2S})$ is the differential oscillator strength, $P_3(\omega_{2S}, b)$ is the ionization probability, and $I(x)$ is the polarization function [85]. $a_\omega = (\hbar/2m_e\omega_{2S})^{1/2}$, a harmonic oscillator radius limiting the collision to distant impact parameters [27].

Similarly to the definition of the binding energy factor, the polarization factor is defined as

$$\epsilon_{2S}^{P}(\xi_S,\theta_S;\, c_S) = 1-\left(\frac{2Z_1}{\theta_S Z_{2S}}\right) h_S(\xi_S;\, c_S)$$
$$= 1-\left(\frac{2Z_1}{\theta_S Z_{2S}}\right)\left(\frac{2n_{2S}}{\theta\xi_S^3}\right) I\left(\frac{c_S n_{2S}}{\xi_S}\right), \qquad (2.75)$$

where $c_S \equiv b_S/a_{2S}$ is a cutoff constant limiting the binding energy correction to low ion energy and the polarization correction to high ion energy. The value of the cutoff impact parameter is chosen to be $b_S = \langle r \rangle_S$, equal to the mean radial distance of the *S*-shell electron from the target nucleus.

The binding energy and polarization effects are combined together to form the binding-polarization factor, ζ_S, given as

$$\zeta_S(\xi_S) = 1+\left(\frac{2Z_1}{Z_{2S}\theta_S}\right)[g_S(\xi_S; c_S)-h_S(\xi_S; c_S)]. \qquad (2.76)$$

After including the increasing binding and polarization effect, the cross section becomes

$$\sigma_S^{PWBA\text{-}PSS} = \sigma_S^{PWBA}(\eta_S, \zeta_S\theta_S), \qquad (2.77)$$

where PSS stands for perturbed stationary state calculation including increased binding and polarization effects.

Coulomb Deflection Effect

At low velocity, the influence of the Coulomb deflection by the target nucleus slows down the projectile and deflects its trajectory. Both effects tend to reduce the inner-shell ionization cross section. Basbas *et al.* [23, 26, 87] extracted

a factor from the SCA [18, 88] by comparing the cross section calculated with a hyperbolic trajectory caused by the Coulomb deflection to the cross section calculated with a straight line trajectory,

$$C = e^{-\pi d q_0} = \frac{\left(\frac{d\sigma}{d\varepsilon_f}\right)^{hyp}}{\left(\frac{d\sigma}{d\varepsilon_f}\right)^{sl}}, \tag{2.78}$$

where q_0 is the minimum momentum transfer defined in equation (2.21) and d is the half distance of closest approach in a head-on collision, $d=Z_1Z_2e^2/2E_1$. In the slow collision limit, the leading term of the differential ionization cross section is given by

$$\left(\frac{d\sigma}{d\varepsilon_f}\right)^{sl} \propto q_0^{-(10+2l_2)}, \tag{2.79}$$

where l_2 is the orbital angular momentum of the S-shell electron.

Inserting equation (2.79) into equation (2.78) gives the Coulomb deflection factor as

$$C_S(\pi d q_0) = (9+2l_2)\mathscr{E}_{10+2l_2}(\pi d q_0), \tag{2.80}$$

where

$$\mathscr{E}_{10+2l_2}(x) = \int_1^\infty t^{-(10+2l_2)} e^{-xt} dt = \frac{e^{-x}}{9+2l_2+x}, \tag{2.81}$$

and

$$x = \pi dq_0 = \left(\frac{\pi Z_1 m_e}{2\mu}\right) \theta_S^{-2} \left(\frac{\eta_S}{\theta_S^2}\right)^{-\frac{3}{2}} \tag{2.82}$$

When the correction for Coulomb deflection is taken into account, the cross section becomes

$$\sigma_S^{PWBA-CPSS} = C_S[\pi dq_0(\zeta_S)]\, \sigma_S^{PWBA}(\eta_S, \zeta_S\theta_S). \tag{2.83}$$

where C stands for Coulomb deflection and PSS was defined in equation (2.77).

For $C_S < 1$, the Coulomb deflection term approaches unity as v_i approaches infinity. Thus, in the high energy limit, the Coulomb deflection as well as the binding energy effect become minimal, so that the ionization cross section becomes close to the PWBA. The Coulomb deflection factor lowers the cross section at low ion velocities. Furthermore, the dq_0 introduces a dependence upon the mass of the incident particle. The presence of Coulomb deflection explains the isotopic effect, and it also improves the theory at low ion velocity.

Relativistic Effects

The electronic relativistic effect becomes important in two regions: heavy target elements and low projectile velocity. For heavy elements it is necessary to use the relativistic wave function for the target electrons. Also, when the projectile energy is low, the collision takes place at a position near the target nucleus. Since the relativistic wave function for the target electron is larger than the non-relativistic one, the relativistic calculation has a larger momentum component than the non-relativistic one [1]. This fact indicates that the probability of the momentum transfer from the projectile to the target electron

during the interaction is larger for the relativistic wave function. Thus, the relativistic effect increases the ionization probability.

Since the PWBA calculation with relativistic wave functions is tedious, Brandt and Lapicki [23] developed a simple relativistic correction to the PWBA in the manner similar to the method used for the increased binding energy modification. The electron's mass in a central potential Z_{2S}/r at a distance r from the target nucleus is replaced by a effective mass that accounts for the relativistic speed. The relativistic mass takes the form

$$m^{R}(r) = m_e\left[1+\left(\frac{Z_{2S}}{2rc^2}\right)^2\right]^{\frac{1}{2}}+\frac{Z_{2S}}{2rc^2}. \tag{2.84}$$

The term $1/r$ represents the mean value of the inverse of the projectile distance to the target nucleus, $R(t)$. The mean value is related to the impact parameter by

$$\frac{1}{r} = \left\langle\frac{1}{R(t)}\right\rangle = \frac{1}{\alpha b}, \tag{2.85}$$

where α=sinh1=1.1752.

The relativistic mass averaged over all impact parameters with weighting functions $W_S(bq_0)$ [23, 87], derivable from the SCA, becomes

$$m_S^{R}(\xi_S) = \int_0^{\infty} m^{R}(\alpha b)\, W_S(bq_0)\, bq_0\, d(bq_0). \tag{2.86}$$

The relativistic correction can be found by replacing η_S by $m_S^R\eta_S$ in the non-relativistic PWBA cross section. The ionization cross section becomes

$$\sigma_S^{CPSSR} = \sigma_S^{CPSS}(m_S^R \eta_S, \zeta_S \theta_S) = C_S[\pi d q_0(\zeta_S)]\ \sigma_S^{PWBA}(m_S^R \eta_S, \zeta_S \theta_S). \tag{2.87}$$

Energy Loss Effect

For low energy ions, the energy loss of the projectile during a collision becomes significant and hence should be considered in the theory. A simple correction method for this energy loss effect was developed by Brandt and Lapicki [29]. From the low velocity formulae for the SCA, the differential cross section including energy loss yields

$$\left(\frac{d\sigma_S}{d\varepsilon_f}\right)^{E\text{-}PWBA} = \left(\frac{d\sigma_S}{d\varepsilon_f}\right)^{PWBA}\left[\left(\frac{q_0}{q_{\min}}\right)^{\nu+1} - \left(\frac{q_0}{q_{\max}}\right)^{\nu+1}\right], \tag{2.88}$$

where ν is equal to $q+2l_2$ and q_0, $q_{\min}$, and $q_{\max}$ are the momentum transfers corresponding to the approximate Q_0, the exact $Q_{\min}$, and the exact $Q_{\max}$, respectively.

Integrating over all possible final states, equation (2.88) yields the following ionization cross section:

$$\sigma_S^{E\text{-}PWBA} = \sigma_S^{PWBA}\left(\frac{\nu \Delta_S^{\nu}}{2^{\nu+1}}\right)\int_{\Delta_S}^{1}\left[\frac{1+\sqrt{(1-\Delta)}}{\Delta} - \frac{1-\sqrt{(1-\Delta)}}{\Delta}\right]d\Delta, \tag{2.89}$$

where $\Delta_S = \hbar\omega_{2S}(M_1/E_1\mu)$ is the minimum kinetic energy loss. After extracting the integral, equation (2.89) becomes

$$\sigma_S^{E\text{-}PWBA} = f_S(z_S)\,\sigma_S^{PWBA}, \tag{2.90}$$

where $f_S(z_S)$ is the energy loss correction, given by

$$f_S(z_S) = \frac{1}{2^{\nu}(\nu-1)}\left[(\nu z_S-1)(1+z_S)^{\nu}+(\nu z_S+1)(1-z_S)^{\nu}\right], \tag{2.91}$$

and $z_S=(1-\Delta_S)^{1/2}=(1-E_S M_1/\mu E_1)^{1/2}$.

The energy loss also affects the Coulomb deflection term. Multiplying the argument of equation (2.80) by $2/[z_S(1+z_S)]$ gives

$$C_S^E = C_S\left(\frac{2\pi dq_{0S}}{z_S(1+z_S)}\right). \tag{2.92}$$

With the above corrections, the ECPSSR theory for ionization gives the following result

$$\sigma_S^{ECPSSR} = C_S^E\left(\frac{2\pi dq_0(\zeta_S)}{z_S(\zeta_S)[1+z_S(\zeta_S)]}\right) f_S[z_S(\zeta_S)]\,\sigma_S^{PWBA}(m_S^R\eta_S, \zeta_S\theta_S). \tag{2.93}$$

2.5 The ECPSSR Theory and Electron Capture

Although the OBKN theory provides a convenient way to calculate the EC contribution to the inner-shell ionization cross section, the calculation yield results larger than the experimental results by a substantial factor. Actually, there is no model that can predict the EC at all velocities [89]. Nikolaev introduced a correction factor to the OBKN approximation to scale down the prediction [36]. Also, Gray *et al.* [63, 64, 90] have suggested the use of various empirical scaling factors with the OBKN in order to accurately describe experimental data. In developing the ECPSSR theory, Lapicki and Losonsky [7] argued against the use of these empirical scaling factors, but used instead the OBKN approach as the

mathematical framework to account for EC and include the increased binding energy, the Coulomb deflection, and the relativistic effects.

To correct for the increased binding energy effect, the parameter multiplied by the reduced binding energy, θ_S, was given as

$$\epsilon_S^B(\xi_{SS'}; c_S) = 1 + \left(\frac{2Z_1}{\theta_S Z_{2S}}\right) g_S(\xi_{SS'}; c_S), \tag{2.94}$$

where c_S is a cut off value based on the fact that the binding increase only occurs for impact parameters less than the mean radius of the *S*-shell electron.

For low energy ions, the Coulomb deflection factor, given as

$$C_{SS'} = e^{-\pi d q_{SS'}(\epsilon_S^B \theta_S)}, \tag{2.95}$$

can be multiplied by the OBKN cross section to give the EC cross section,

$$\sigma_{EC}^{<} = C_{SS'}\, \sigma_{EC}^{OBKN}[\xi_{SS'}(\epsilon_S^B \theta_S), \epsilon_S^B \theta_S]. \tag{2.96}$$

For high energy ions, the EC cross section is given as [7]

$$\sigma_{EC}^{>} = \frac{1}{3}\, \sigma_{EC}^{OBKN}[\xi_{SS'}(\theta_S), \theta_S], \tag{2.97}$$

where the 1/3 factor was obtained from the second Born approximation for arbitrary Z_1 and Z_2 by the Eikonal calculations of Eichler *et al.* [91] and Reading *et al.* [92]. Equation (2.97) has also been suggested by Shevelko [93] and by Shakeshaft [94].

Lapicki and McDaniel [8] also noted that the two formulae (2.96) and (2.97) may be connected through the use of the following:

$$\sigma_{EC}^{CPSS} = \frac{\sigma_{EC}^{<}\,\sigma_{EC}^{OBKN}}{2\sigma_{EC}^{<}+\sigma_{EC}^{OBKN}}. \tag{2.98}$$

When the incident projectile velocity, v_i, is slower than the orbital electron velocity, v_{2S}, the EC cross section from OBKN, σ_{EC}^{OBKN}, is larger than the EC cross section after modification for increased binding and Coulomb deflection, σ_{EC}^{CPSS}. However, when $v_i >> v_{2S}$, σ_{EC}^{OBKN} is close to σ_{EC}^{CPSS} if $\epsilon_S^B \rightarrow 1$ and $C_{SS} \rightarrow 1$.

Referring to equation (2.86), the relativistic effect can also be taken into account giving the following EC cross section:

$$\sigma_{EC}^{ECPSSR} = C_{SS}\cdot\,\sigma_{EC}^{OBKN}[\xi_{SS}^{R}\cdot(\epsilon_S^B\theta_S), \epsilon_S^B\theta_S] \tag{2.99}$$

where

$$\xi_{SS}^{R}\cdot(\epsilon_S^B\theta_S) = \xi_{SS}\cdot(\epsilon_S^B\theta_S)\sqrt{m_S^R[\xi_{SS}\cdot(\epsilon_S^B\theta_S)]}. \tag{2.100}$$

Thus, using a modified OBKN approach, Lapicki and Losonsky [7] and Lapicki and McDaniel [8] developed a more suitable theory that predicts the experimental data without the need for a multitude of empirical scaling factors.

2.6 Semi-Classical Approximation (SCA)

In the SCA, Bang and Hansteen [18] have approximately treated the effects of nuclear repulsion for atomic collision models involving the use of a classical trajectory. The major effects are due to (i) the change in the path of the incident particle, which is almost always negligible for heavy particles; and (ii) the decrease in kinetic energy of the incident particle, which becomes important near threshold. They carried out their approximation by means of an impact

parameter formulation in which they inserted appropriate deflection corrections. The resulting changes are negligible for high velocity ions. Without these corrections, the SCA result is identical to the Born approximation.

In the SCA calculation, the total ionization cross section is obtained by integrating a suitable ionization probability $I(b)$ over all impact parameters. Thus,

$$\sigma^{SCA} = \int_0^\infty I(b) 2\pi b db, \tag{2.101}$$

where $I(b)$ is given by

$$I(b) = \int_0^{\varepsilon_f^{max}} \frac{dI(b)}{d\varepsilon_f} d\varepsilon_f . \tag{2.102}$$

Here, the differential ionization probability, $dI(b)/d\varepsilon_f$, is found by squaring the transition amplitude. The transition amplitude can be defined in a similar way to the first Born transition amplitude, and the interaction potential between the ion and the target electron is taken as the time-dependent term, $V(t) = Z_1 e^2/|r - R(t)|$, where $R(t)$ represents the radius vector to the projectile. Either using a standard multipole expansion of the potential or its Fourier transform [70] leads to a useful factorization of the SCA transition amplitude into a classical trajectory factor [95].

2.7 Binary Encounter Approximation (BEA)

The BEA, a classical method for ionization, arises from the "impulse approximation" [20, 21] that exactly treats the interaction between the incident particle and the bound electron. On the other hand, the Born approximation treats the interaction between the incident particle and the target atom as a

perturbation. The derivation of the BEA is based upon an energy transfer process in which a projectile with energy E_1 collides with an inner-shell electron having binding energy E_{2S} [15-17, 96-100]. By integrating over all allowed energy-transfers and considering a weighting function of the distribution of the bound electron momenta, the ionization cross section is defined by

$$\sigma^{BEA} = \frac{n_{2S}^2 Z_1^2}{E_{2S}^2} f\left(\frac{E_1}{\lambda E_{2S}}\right), \tag{2.103}$$

where λ is ratio of the projectile mass to the target electron mass and $f(E_1/\lambda E_{2S})$ is a universal function, the dynamics of which can be expressed in terms of the following scaled-velocity parameter:

$$\frac{E_1}{\lambda E_{2s}} = \left(\frac{v_i}{v_{2S}}\right)^2 = n_{2S}^2\left(\frac{\eta_S}{\theta_S}\right) = \frac{1}{4}(\theta_S \xi_S^2). \tag{2.104}$$

If $\lambda \gg 1$, and the universal function $f(E_1/\lambda E_{2S})$ is nearly independent of λ, then the universal function for the BEA is analogous to the function $f_S(\theta_S, \eta_S)$ of the PWBA.

2.8 Other Views Related to Electron Capture

The dynamics of electron capture are actually still not well understood. Since the EC and ionization require a three body Coulomb description, these processes are much harder to treat theoretically than the elastic and excitation problem. Fragmentary results, mainly at low velocity in nearly symmetric collisions where a molecular representation provides an adequate framework and at asymptotically high velocities where the Thomas double-collision mechanism

dominates, exist but no comprehensive pictures emerged [101].

Several theoretical models have been developed to predict EC for high velocity ions [102]. Shakeshaft and Spruch [81] discuss three different mechanisms for capture of an electron from a heavy nucleus by another bare heavy nucleus which is incident with a very high relative velocity. The first mechanism is knock-on capture [103], where the two nuclei have equal masses and simply switch places in the lab frame (in which the target nucleus is initially at rest). The incident nucleus gives up all of its kinetic energy to the target nucleus, which is therefore knocked forward, but the electron remains behind and becomes bound to the incident nucleus, which has come to rest. The second mechanism is radiative capture, which occurs with the emission of a photon while the target nucleus plays no role. This mechanism was first analyzed by Oppenheimer [34], and the cross section was calculated by the impulse approximation [104]. The third mechanism is the double collision mechanism, first suggested within the framework of classical mechanics by Thomas in 1927 [105] and later analyzed by Drisko [80] within the framework of quantum mechanics. In this mechanism the target electron undergoes two collisions, first with the incident nucleus, and then with the target nucleus; as a result, the electron finally attains almost the same velocity as the incident ion and, therefore, has a reasonable probability of being captured. This double collision mechanism is the dominant mechanism at high velocities for non-radiative electron capture [77, 106]. It corresponds to a second Born term. Hence at least a second order theory is required to describe nonradiative electron capture at high velocities. The first Born, or any theory based upon the first Born, will fail adequately to describe electron capture at high velocity. The second Born approximation behaves as v_i^{-11} at asymptotically high

velocities which is the correct behavior. However, the first Born behaves as v_i^{-12} at asymptotically high velocities. Both the impulse approximation and the strong potential Born tend to the second Born at asymptotically high velocities [79].

Lin and Tunell [107-109] developed a two-state atomic-expansion method for electron capture, which is useful in the intermediate velocity region $v_i \sim v_{2s}$. Retaining only the two states that are relevant to the capture process, the initial state of the target and the final state of the projectile, they expanded the time-dependent electronic eigenfunctions in terms of the traveling eigenstates of the two collision partners. Capture occurs primarily at large impact parameters, comparable to or greater than the typical orbital radius of the electron in the initial state, for which the wave functions can easily be approximated by a two-state atomic expansion.

Recently, Fritsch and Lin [110] gave a review of the semiclassical close-coupling description of atomic collision in an energy range of roughly 0.1 up to a few hundred keV per nucleon of the projectile, with emphasis in its application to a wide range of electron transition phenomena.

CHAPTER 3

EXPERIMENT

3.1 Experimental Process

Figure 3.1 shows a schematic of the accelerator, magnets, beamline, and target chamber that were used for the experiments in this thesis. The SNICS (Source of Negative Ion by Cesium Sputtering) produces negative ions at 69 keV. These ions are first analyzed for momentum/charge by 30° and 90° magnets and then injected into the tandem accelerator. The negative ions are accelerated to the terminal at the center of the tandem where the voltage can be as high as 3 MV. At the accelerator terminal the ions enter a gas stripping canal and are stripped to a positive charge states. The positive ions are then accelerated back down to ground potential and gain an additional energy qV_T where q is the charge state of the ion that leaves the stripping canal, and V_T is the terminal voltage of the accelerator. The charge state distribution of ions that pass through a foil or gas stripper depends on the initial energy of the ion [102, 111]. In general, high energy ions can be stripped to higher charge states. The graph in the publication of Marion and Young [112] shows the calculated equilibrium charge state fractions for the carbon ion beam passing through a carbon foil. The charge state fraction for the carbon ions as a function of ion velocity helps determine the available charge states in the gas canal and in the post-accelerator gas cell. But, carbon ions do not reach equilibrium in the gas stripper. The actual processes

involved in stripping calculations are still subject to debate [102]. At the maximum terminal voltage, 3 MV, of the UNT tandem accelerator, it is not possible to produce usable quantities of the charge state 5+ and 6+ carbon ions from stripping in the gas canal inside the accelerator. In this experiment it was desirous to obtain x-ray cross section data for all charge states (3+, 4+, 5+ and 6+) for carbon energies between 2 and 12 MeV. The only way that this was possible was to place a post accelerator gas cell stripper after the ions had been accelerated to high velocities (see figure 3.1). The detailed description of this gas

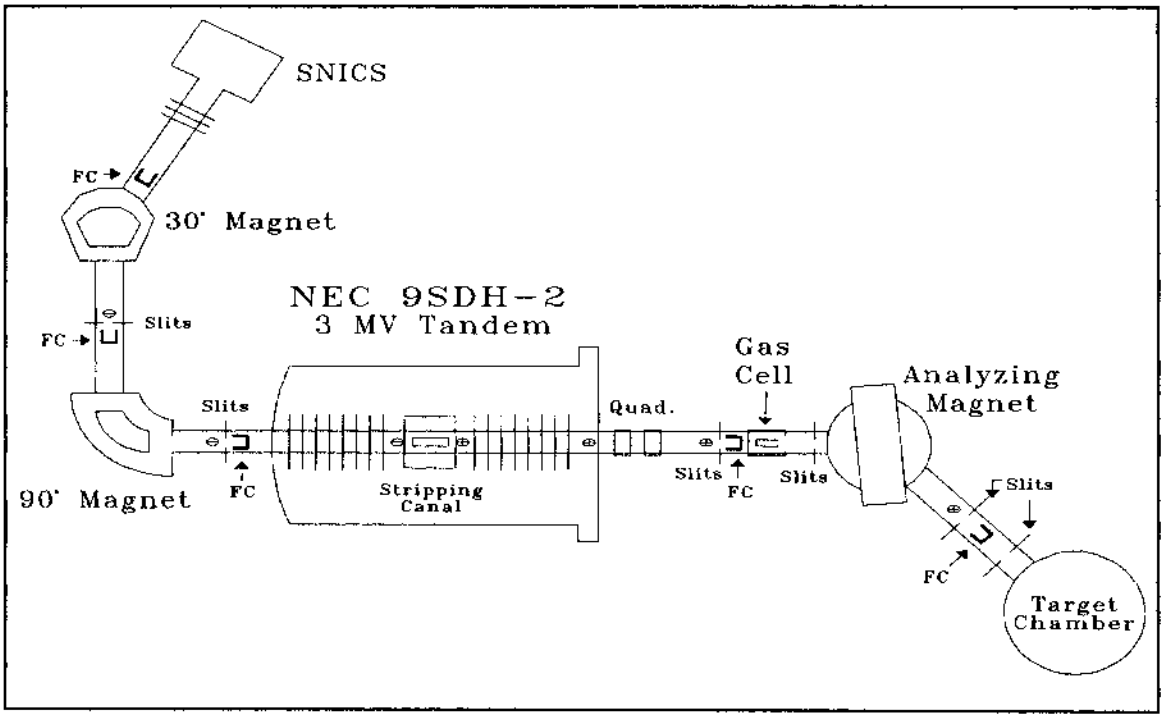

Figure 3.1 Schematic diagram of the experimental apparatus used for Ion-Atom collision measurements. The apparatus includes the SNICS (Source of Negative Ion by Cesium Sputtering), FC (Faraday Cup), 30° and 90° magnets, slits, NEC 9SDH-2 3 MV tandem accelerator with its gas stripping canal inside, Quadruple focus lens, gas cell, high resolution magnetic spectrometer, and target chamber.

cell can be found in the literature [113]. Before installing the gas cell, carbon foil strippers were tried in the same location on figure 3.1 as the gas cell. Figure 3.2 shows the diagram of the carbon stripper designed by Marble [67]. The carbon foils were self supported and about 15 $\mu g/cm^2$ thick. The two major problems with the carbon foils were: (i) The foils gradually became weakened and eventually would break under beam bombardment. Many of the experimental data points took in excess of ten hours; renormalizing with a new foil was very time consuming. (ii) The solid foils produced an energy loss ΔE that would be different from foil to foil and also time dependent as the foil thinned under beam bombardment. The installation of the gas cell tended to solve most of the problems. A diagram of this gas cell, which was designed by Kim [113], is shown in figure 3.3. In the figure the ions are stripped in region P_A. The nitrogen stripping gas is introduced into the region P_A through a precision metering valve 1. The pressure in the region P_A is constantly monitored with a capacitance manometer. The system is pumped by a turbopump that is just below the stripping canal. The dilute stripper gas produced very little ΔE for even the low energy ^{12}C ions, and hence the renormalization problem was also solved. After the stripping gas cell, the beam was analyzed with the 40° HVEC magnet and directed into the analysis chamber. Figure 3.4 shows a magnet scan of typical ^{12}C beams that are produced with the post-accelerator gas stripper. The labeled beams are all ^{12}C beams. In the figure the notation (1,4) means the beam came into the stripping gas cell with charge 1+ and left with 4+. With the aid of scans like these it was possible to select the proper charge state and energy of the carbon ions that were used for the experiment. Table 3.1 shows the typical beam currents that were produced at various energies and charge states. In the table,

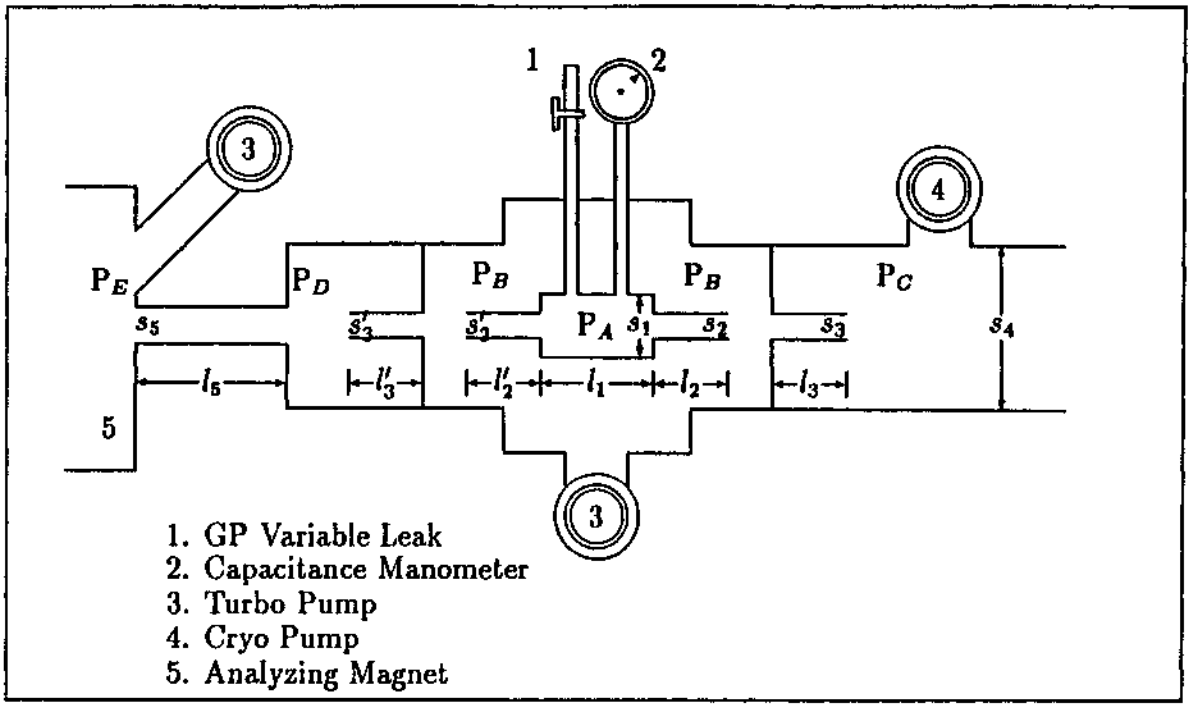

Figure 3.2 Drawing of the post-acceleration stripping chamber that was designed for solid stripper foils (ref: [61]).

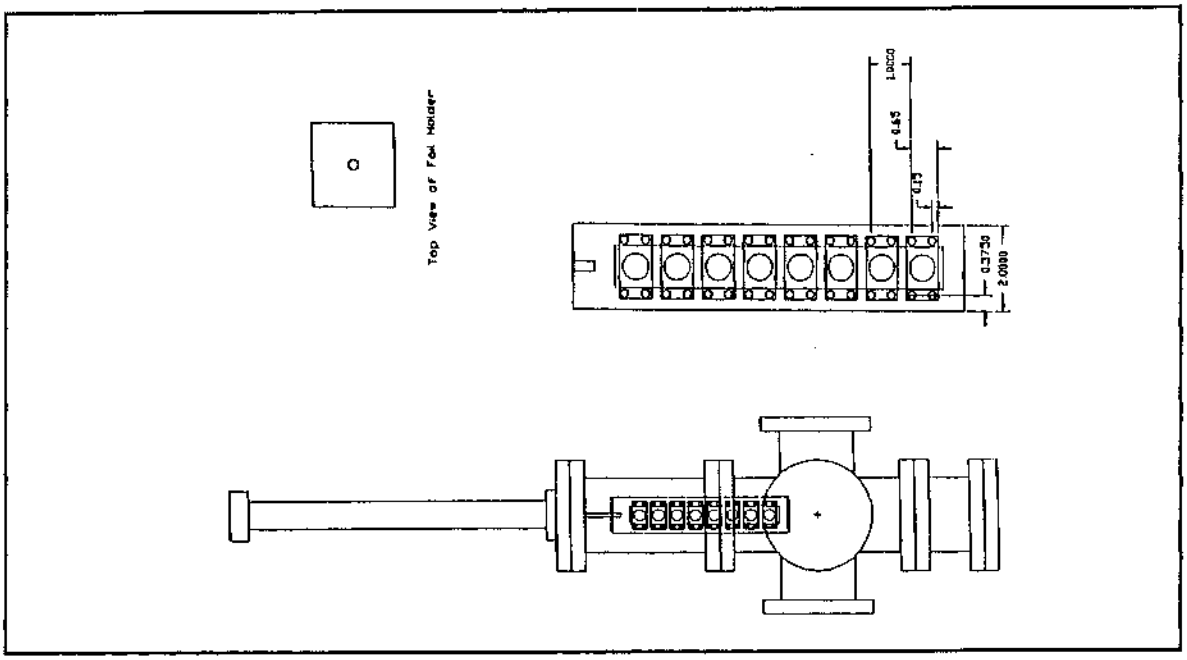

Figure 3.3 Schematic diagram of the differentially pumped gas cell placed between the tandem accelerator and analyzing magnet to increase the production yield of highly charged ions (ref: [109]).

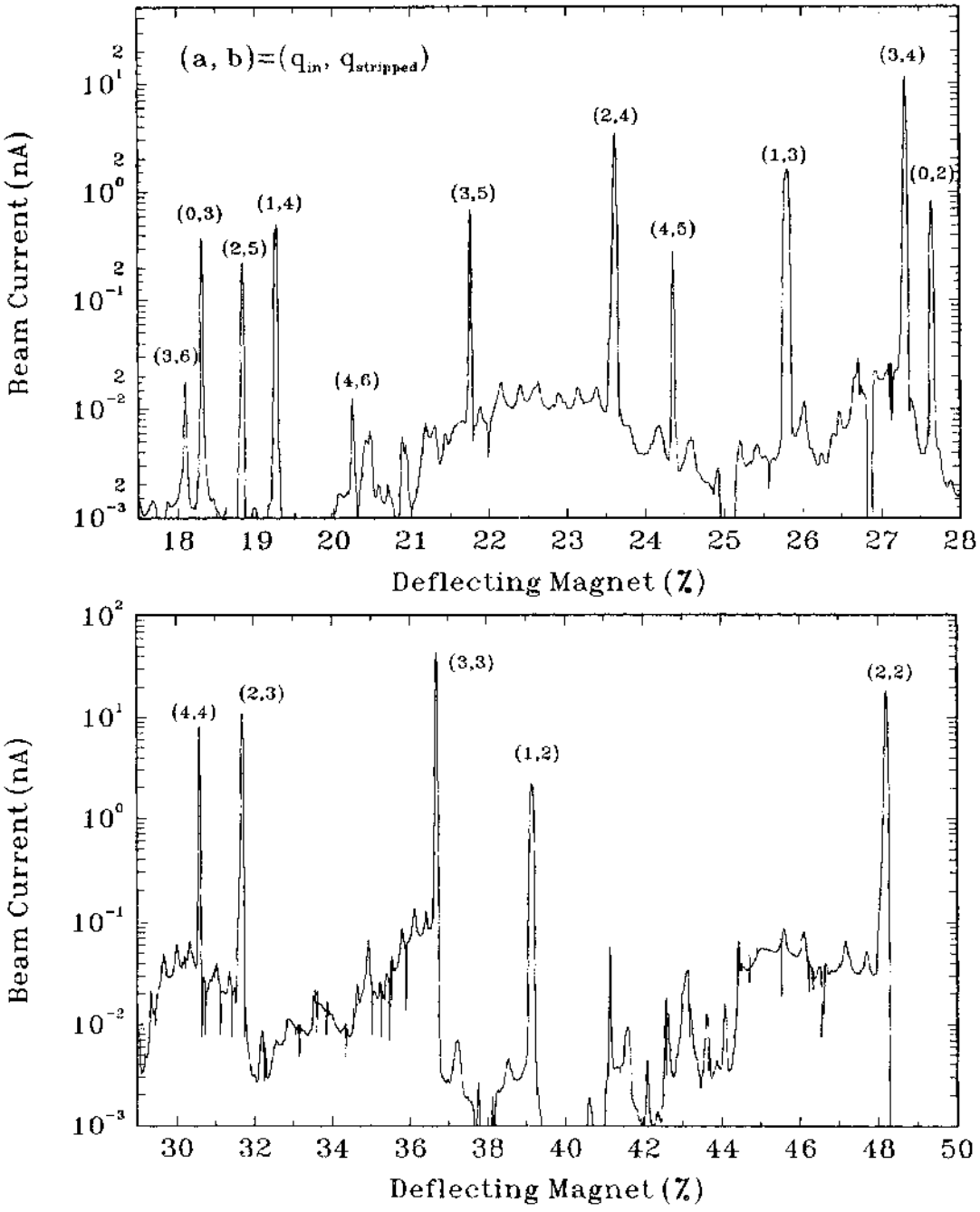

Figure 3.4 The spectra for momentum/charge scanned by the HVEC deflecting magnet for carbon ions. The terminal voltage of the accelerator is 1.983 MV for accelerating ion beam of charge q_{in}. The ion beam of charge $q_{stripped}$ is selected by the 40° HVEC magnet after the stripping in the gas cell.

Table 3.1 The beam currents that were produced with the post-accelerator gas stripper and the tandem accelerator gas stripper. In the table V_T is the tandem accelerator terminal voltage and p is pressure near the post-accelerator stripper.

E (MeV)	V_T (MV) ±.0010	q	p (Torr)	I (q) nA
2	0.6445	2+	1.5×10^{-7}	3.90
2	0.6445	3+	7.5×10^{-7}	1.60
2	0.6445	4+	1.0×10^{-6}	1.10
2	0.6445	5+	$>1.0\times10^{-6}$	-----
4	0.9832	3+	1.4×10^{-7}	8.80
4	0.9834	4+	7.6×10^{-7}	5.90
4	0.9834	5+	7.6×10^{-7}	0.22
4	0.9834	6+	7.7×10^{-7}	0.13
6	1.4830	3+	9.8×10^{-8}	240.00
6	1.4835	4+	7.1×10^{-7}	139.00
6	1.4835	5+	7.1×10^{-7}	11.50
6	1.4835	6+	7.1×10^{-7}	0.30
8	1.9830	3+	1.2×10^{-7}	720.00
8	1.9834	4+	5.9×10^{-7}	400.00
8	1.9834	5+	6.0×10^{-7}	48.00
8	1.9834	6+	6.0×10^{-7}	1.95
10	2.4830	3+	1.3×10^{-7}	600.00
10	2.4850	4+	6.3×10^{-7}	270.00
10	2.4849	5+	6.4×10^{-7}	40.00
10	2.4849	6+	6.4×10^{-7}	2.20
12	2.3865	4+	1.3×10^{-7}	135.00
12	2.3865	5+	5.9×10^{-7}	11.90
12	2.3865	6+	1.1×10^{-6}	1.00

V_T is the tandem terminal voltage in MV, q is the measured charge state, p is the pressure reading of the capacitance manometer. From the table, it can be seen that it was not possible to produce usable quantities of q=5+ and 6+ at 2 MeV and q=3+ at 12 MeV. All charge states 3+, 4+, 5+ and 6+ were obtained at the rest of the energies used in this work.

The Target Chamber

Figure 3.5 shows the schematic diagram of multi-functional target chamber used for the x-ray measurements. In front of the chamber, the beam was collimated by two sets of slits 40 cm apart. The first group of slits with a width of

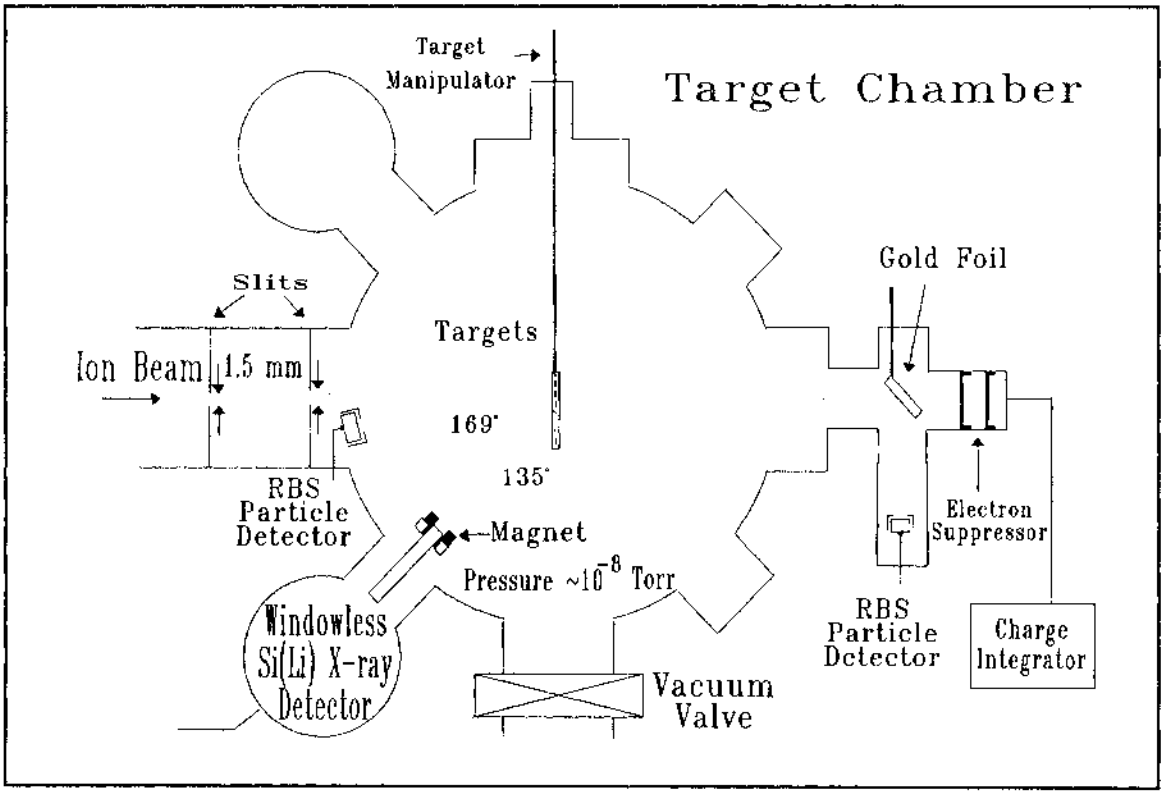

Figure 3.5 Schematic diagram of the ultra-high-vacuum target chamber that was used for the x-ray measurements.

1.5 mm was used for selecting the desired beam, and the second group with a width 0.5–1.5 mm was used to define the beam spot on the target. The target chamber was maintained at a pressure below 4×10^{-8} Torr by a cryopump, and had an interlock for target insertion. The target holder was perpendicular to the beam direction. The targets were made by evaporating the target element onto 5 $\mu g/cm^2$ thick carbon backing foils. The technique developed by the UNT group for preparing contaminant-free targets has been described in the literature, [42, 58, 67-69]. The Link Analytical windowless Si(Li) x-ray detector was mounted at 135° with respect to the beam direction. A deflecting magnet with a collimator was mounted in front of x-ray detector to eliminate scattered charged particles [114]. A Rutherford backscattering (RBS) particle detector was mounted at 169° with respect to the beam direction. The solid angle, $\Delta\Omega=A_r/R^2=6.77\times10^{-3}$ sr, of the RBS detector was calculated from the area of the defining aperture A_r and the distance R to target and was confirmed by using an National Institute of Standard and Technology calibrated ^{241}Am source. The x-ray cross section can be measured, independent of target thickness and beam fluctuations, by simultaneously measuring x-rays and scattered particles for each case. The x-ray cross section is given by

$$\sigma_X = \frac{Y_X \sigma_R \Delta\Omega\, t_X}{Y_R \varepsilon_X A_X}, \tag{3.1}$$

where Y_X and Y_R are the number of measured x rays and scattered particles, respectively, σ_R is the theoretical Rutherford cross section, t_X is dead time for the measurement of x rays, ε_X is the calibrated efficiency (intrinsic+solid angle) of x-ray detector, and A_X is target x-ray attenuation factor [115] for self absorption.

Because the heavy ions traveling through target may not be in their equilibrium charge states, the charge collected from the current integrator at the post target chamber cannot be used to determine the number of incident ions interacting with the target. In order to reduce the instrumental dead time of the windowless x-ray detector for measuring high yields of low-energy carbon x rays and bremsstrahlung, the carbon ion beam current was kept below 0.5 nA. For some of the measurements described, it took over 10 hours to get good statistics for the backscattered projectiles. This is mainly because of the $1/E^2$ dependence of the Rutherford backscattering cross section and the fact that the charge state dependence measurements can only be done with vanishingly thin targets. In order to overcome the low counting statistics for the back angle RBS detector, a separate gold scattering chamber was added (see fig. 3.5) after the main scattering chamber. In this post chamber, a 200 $\mu g/cm^2$ gold foil was used as a scattering foil that produced a large RBS yield. A second RBS detector was used to count $^{12}C^{q+}$ ions scattered from Au at 90° with respect to the beam direction. The ratio of the backangle RBS yield is always proportional to the gold scattering yield at 90°. The backangle RBS at 169° and the gold scattering RBS were measured once for each carbon energy to obtain good counting statistics. Therefore, for the high energy carbon ions, this ratio could be used to renormalize the backangle scattering where the statistics are poor.

Figure 3.6 shows the electronic set up that was used for the experiments in this thesis. The signals from x rays and Rutherford backscattered carbon ions from the target were stored in different quadrants of the same multi-channel analyzer (MCA). Pulse generators were used in both quadrants to establish the dead time corrections. As was mentioned above, for the high energy data, good

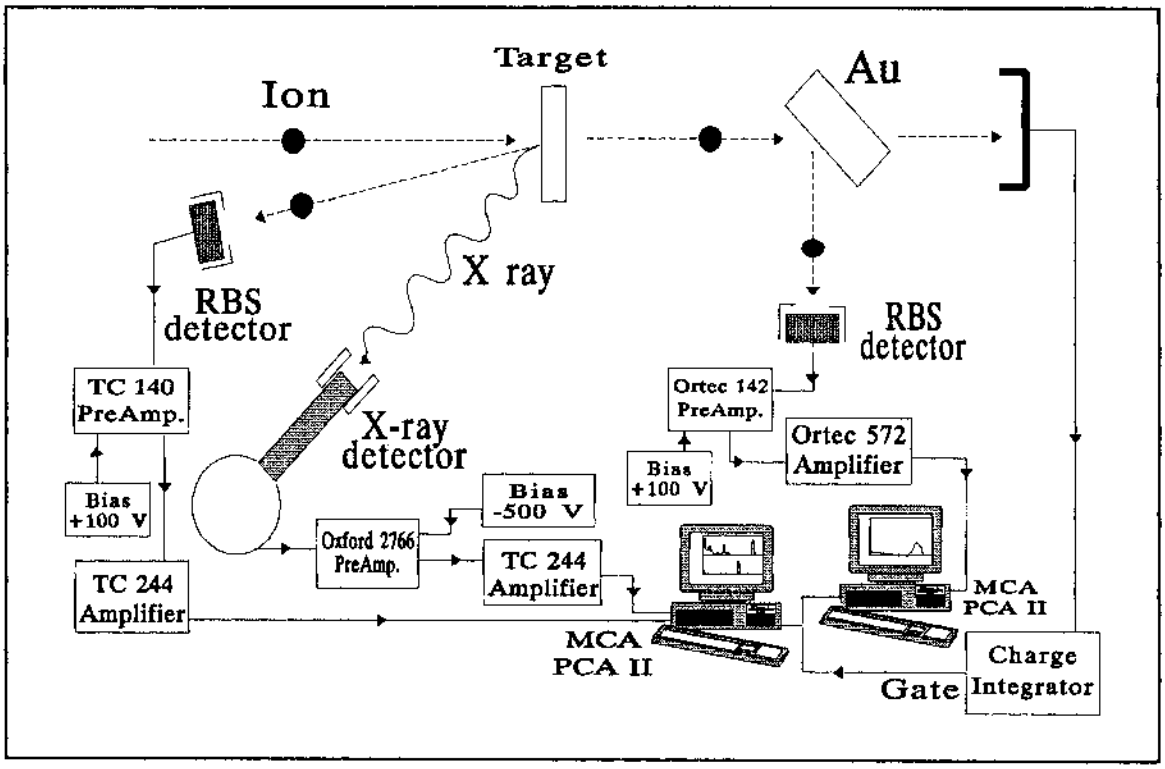

Figure 3.6 Electronics that were used to simultaneously measure x rays and Rutherford scattering particles from the target and the gold foil beam monitor.

counting statistics in the RBS detector were difficult to obtain. A second scattering chamber was added so that the beam would pass through the holmium target and then enter this gold scattering foil chamber. These scattered ions from the gold target were counted by the second RBS detector and MCA shown in figure 3.6.

3.2 The Windowless Si(Li) X-ray Detector and Its Efficiency Calibration

The windowless Si(Li) x-ray detector was important to the success of these experiments. These detectors, which are manufactured by Link Analytical Inc., are used primarily for Scanning Electron Microscopy (SEM). The quoted system

resolution for the Mn K_α line was 135 eV. The system used standard NIM electronics and hence if an electronic problem developed, it could be readily fixed in our laboratory. The advantage of the detector is that since it does not have a beryllium window, it can measure low energy x rays down to the boron K_α line at 185 eV. In general, Si(Li) x-ray detectors have a 7.6μm thick beryllium window that precludes measurements below photo energies of 1 keV. Figure 3.7 shows carbon K_α, oxygen K_α, fluorine K_α and Ho M x-ray peaks from HoF_3 target on an oxidized carbon foil. It should also be pointed out that the FWHM (resolution) of 76 eV for the $_6$C K_α peak at 0.282 keV is probably a "state of the art" resolution figure, at least according to the manufacturer of the detector. The resolution of the $_{67}$Ho $M_{\alpha\beta}$ peak was approximately 95 eV. The excellent

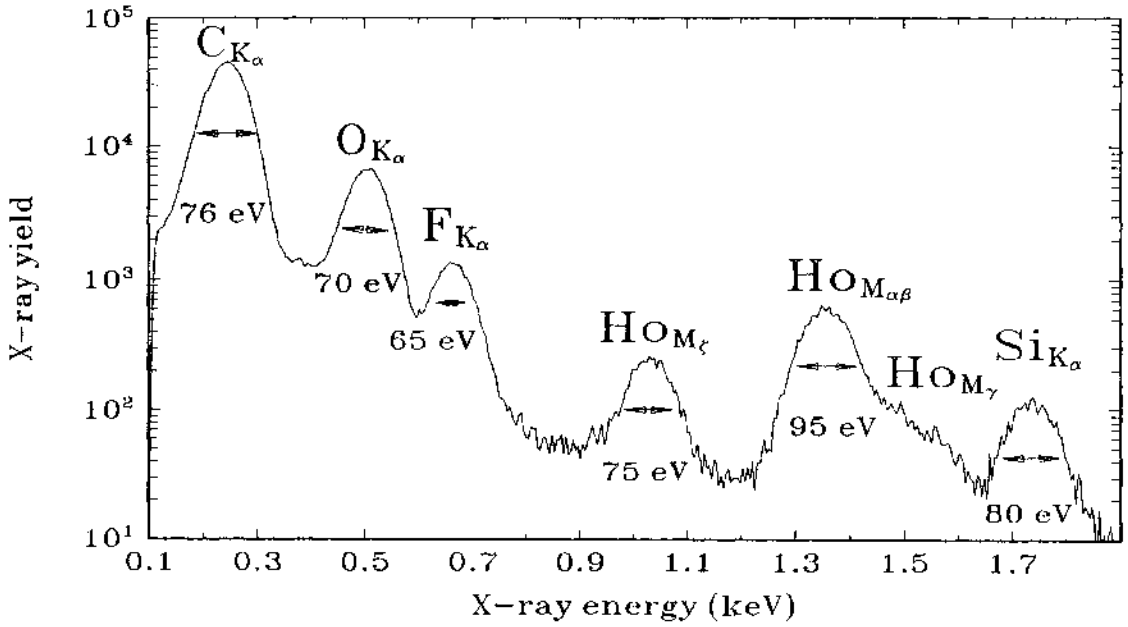

Figure 3.7 X-ray spectrum of 2 MeV protons on a HoF_3 target with a 5 $\mu g/cm^2$ carbon foil backing. The spectrum shows that the detector resolution of carbon K x-ray is 76 eV.

resolution, along with the x-ray fitting routines (GUPIX) [116], allowed us to measure the individual cross sections for the $_{67}$Ho M_{ζ}, $M_{\alpha,\beta}$, and M_{γ} x-ray transitions. In order to get better resolution, a crystal spectrometer would have to be used, however, this would be impractical for the very thin targets that had to be used for the experiments since the efficiencies of these units are at best 10% of that of a Si(Li) detector. This would give an acquisition time of 3 days per spectrum in figure 3.7.

The most difficult problem associated with the detector was in determining the efficiency of the detector as a function of photo energy. The efficiency of a Si(Li) detector depends upon the numbers of x rays absorbed by the window, if there is a window, the gold contact layer, the detector dead layer, and upon the number of photons stopped in the active region of the detector. Most Si(Li) detectors are supplied with a beryllium window. Low energy x-ray absorption by the window, the gold electrode, the Si dead layer, and depletion depth of the crystal alter the efficiency of the detector. These effects can be calculated using $I/I_0 = e^{-(\mu/\rho)\rho t}$, where I/I_0 is the fraction of X-rays transmitted through a given material having a thickness t, μ/ρ is the mass absorption coefficient of the material and ρ is the mass density of the material. The formula for calculating the absolute efficiency relative to the corresponding number of photons emitted into 4π steradians from the x-ray source is given by Campbell and McGhee [117]:

$$\varepsilon = \frac{\Omega}{4\pi}[\exp(-\sum_{1}^{4}\mu_i d_i)]\, f_E[1-\exp(-\mu_{Si}D)], \tag{3.2}$$

where i denotes the window itself, a possible ice layer, the gold electrode, and the silicon dead layer where charge collection is not complete; the d_i's are the

thicknesses of these absorbers, and the μ_i are their linear attenuation coefficients; Ω is the solid angle of the detector. The factor f_E corrects for loss of events occurring near the front surface of the crystal in which a silicon K x-ray escapes; the μ_{Si} and D are the attenuation coefficient and thickness of silicon, respectively.

There are three major techniques for measuring the efficiency of a Si(Li) x-ray detector. They are (i) standard radioactive sources for the 3.3-100 keV region [117-122], (ii) PIXE (Particle-Induced X-ray Emission) cross sections for the region below 3 keV region [123], and (iii) AFB (atomic-field bremsstrahlung) from 0.6 to 8.2 keV [124].

By the first method the efficiency is calculated from the measured ratio of the number of photons, N_m, of a characteristic x-rays to the number of photon, N_e, emitted from a source during the measuring time t. The relation is

$$\varepsilon = \frac{N_m}{N_e} = \frac{N_m}{DIt} \tag{3.3}$$

where ε is the measured efficiency of detector, D is the activity of the source at the time of the measurement, and I is the relative intensity (photons per decay). In figure 3.8 it can be seen that this method gives results that are consistent with the other methods. The data point at 3.3 keV, which comes from the ^{241}Am source, is obviously low. This x-ray comes from the M-shell internal conversion in the daughter ^{237}Np. The source is made by electro-depositing ^{241}Am onto a platinum blank. The point is probably low because of the self absorption of the 3.3 keV photon in the deposited ^{241}Am layer. As is shown in table 3.2 there are no radioactive sources with photon energies less than 3.3 keV that are practical to use. Therefore below 3.3 keV the efficiency has to be determined by the PIXE method or the Atomic Field Bremsstrahlung (AFB) method.

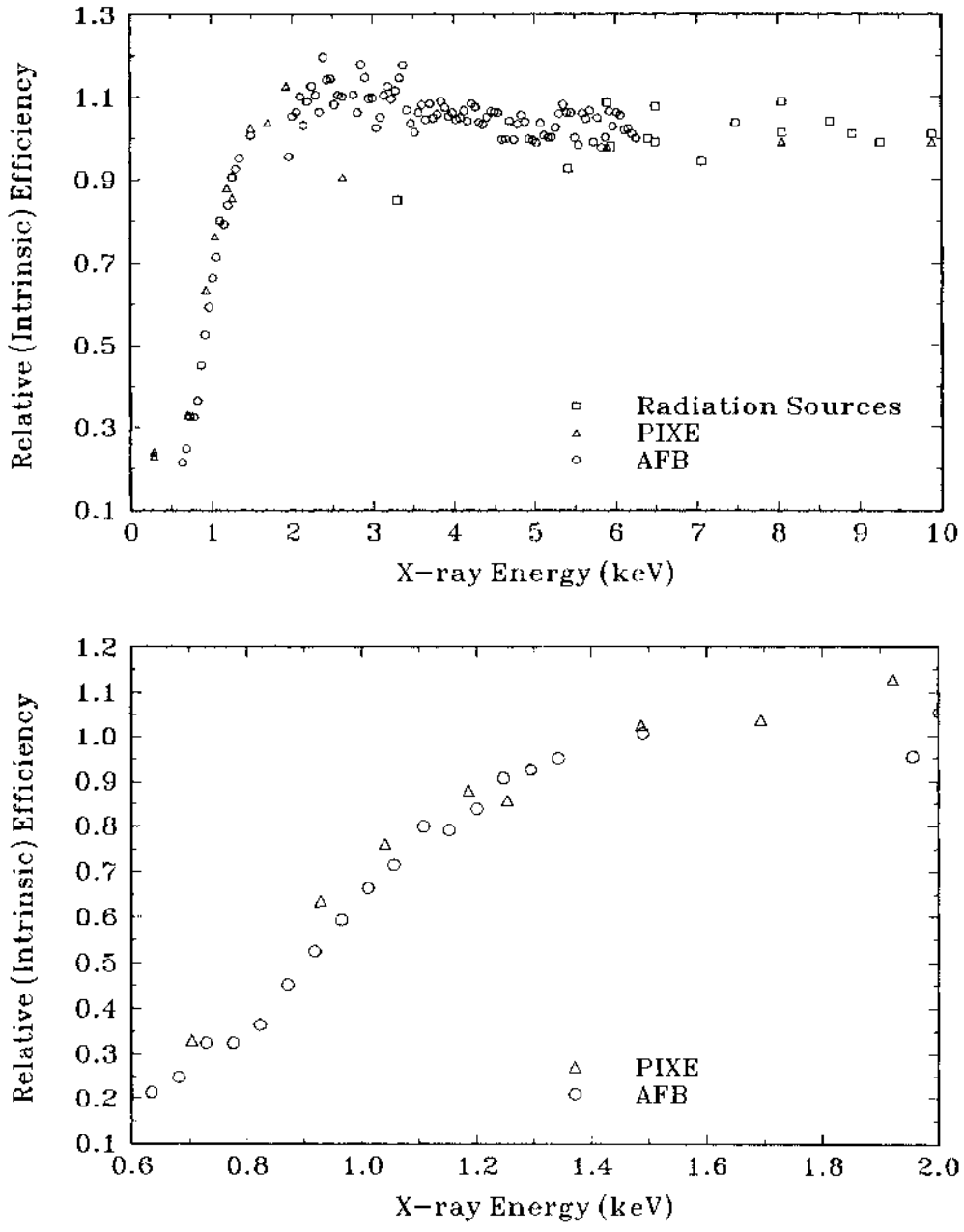

Figure 3.8 The relative efficiency data curve calibrated by the radioactive sources, the PIXE (particle induce x-ray emission) method, and the AFB (atomic field bremsstrahlung) method. The region of interest for M-shell x-ray energies are from 1.045 keV to 1.576 keV.

Table 3.2 The radioactive sources and their photon intensities per decay at different x-ray energies which were used for efficiency calibration of the x-ray detector. The half life of sources is given (d is days and y is years) [117-122].

Sources	Half Life $T_{1/2}$	Emission type	Energy (keV)	Photons per Decay	References
^{51}Cr	27.71 d	K_α	4.952	0.1988	[117]
		K_β	5.427	0.027	[117]
^{54}Mn	312.12 d	K_α	5.414	0.2234	[117]
		K_α	5.414	0.2213	[118]
		K_β	5.946	0.0305	[117]
		K_β	5.946	0.0294	[118]
^{55}Fe	2.73 y	K_α	5.898	0.245	[118]
		K_β	6.49	0.033	[118]
^{57}Co	271.8 d	K_α	6.403	0.5020	[117]
		K_α	6.403	0.494	[118]
		K_β	7.057	0.0691	[117]
		K_β	7.057	0.0663	[118]
		γ	14.41	0.093	[117]
		γ	14.41	0.0954	[118]
^{65}Zn	243.8 d	K_α	8.047	0.3439	[117]
		K_α	8.047	0.3347	[117]
		K_β	8.904	0.0479	[117]
		K_β	8.904	0.0462	[117]
^{137}Cs	30.17 y	$L_{\alpha,\beta}$	4.47+4.83	0.00815	[119]
^{155}Eu	4.71 y	L	6.06	0.08	[118]
^{241}Am	432.7 y	M	3.3	0.0634	[120]
		M	3.3	0.048	[121]
		L_η	11.88	0.0086	[122]
		$L_{\alpha1,\alpha2}$	13.95+13.76	0.133	[117]
		$L_{\eta,\beta}$	15,87+17.74	0.1946	[122]
		L_γ	20.774	0.0485	[122]

The PIXE method was originally developed by Lennard and Phillips of Western Ontario University [123]. The method involves the measurement of the K x-ray production cross sections for 1 to 2 MeV alpha-particles and protons for low Z elements and comparing these measurements with the theory. The ECPSSR theory [23-27] were used for comparison for efficiency calibration. The theoretical calculations [31] gives results that seem to be within 10-20% of the measured values from the Ge-K_α peak at 9.89 keV down to the Na-K_α peak at 1.04 keV. The triangles on the efficiency curve of figure 3.8 show the data for seven elements in this range. Below 1 keV the efficiency can not be determined by the PIXE method because of uncertainty in the fluorescence yield and photon attenuation in the target. The method that seem to be valid in this region below 3 keV is the AFB method (see fig. 3.8).

The AFB method was suggested by Dr. C.A. Quarles of Texas Christian University (TCU) and has been proven to provide the necessary data to determine the efficiency for the low energy region [125-128]. Theoretical predictions of the AFB cross section are in agreement with existing measured values down to 3 keV [128]. The theoretical calculations of differential AFB cross sections as a function of photon energy have been made, and are available in tabulated form [129]. This calculated AFB cross sections are expected to be accurate to within 11% for the lower photon energy range down to 200 eV [129]. A detector's efficiency function can be determined by comparing measured bremsstrahlung spectra with the calculated spectral distributions. In order to make these measurements, an experiment was done by Weathers *et al.* [124] at TCU using a 300 kV Cockcroft-Walton accelerator. Figure 3.9 shows the experimental arrangement from reference [124]. The collimated electron beam with an energy of 66.5 keV energy

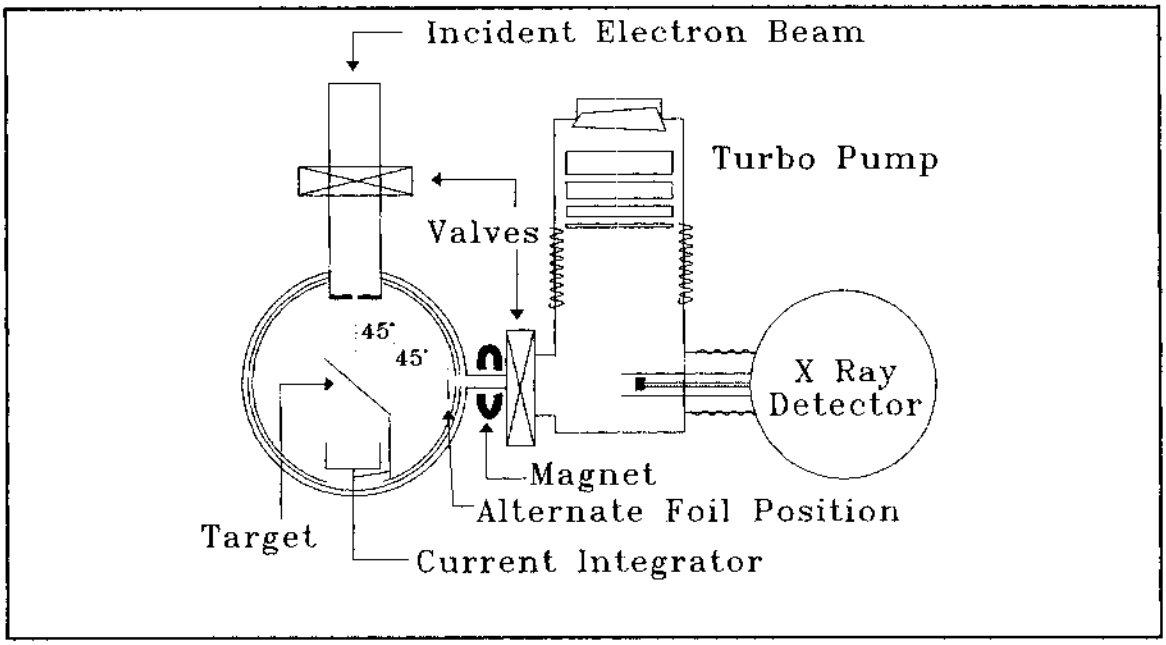

Figure 3.9 Schematic diagram of the AFB experimental configuration at Texas Christian University (ref: [124]).

was used to bombard self-supporting targets of Ag, Au, and Al mounted at a 45° angle to the beam direction to produce the bremsstrahlung spectra. To prevent scattered electrons from entering the detector, permanent magnets were mounted adjacent to the flight path between the detector and target chamber. The windowless Si(Li) x-ray detector was used to measure the energy dependence of the bremsstrahlung distribution. The experimental results were then compared with the known theory.

For this experiment [124], the measured net photon yield per incident electron, corrected for background, is approximated by

$$y_{net} \approx \epsilon(k)\Delta\Omega\Delta k\int_0^h e^{-\mu(k)x\csc\psi}\left(\frac{d^2\sigma}{d\Omega\,dk}\right)dx, \tag{3.4}$$

where k is the photon energy; ϵ(k) is the detector efficiency; $\Delta\Omega$ is the detector solid angle; Δk is the energy width of each MCA channel; h is equal to t/cosψ where t is the target thickness (atoms/cm^2); ψ is the angle between the target normal and the beam axis (nominally 45°), $d^2\sigma/d\Omega dk$ is the doubly-differential cross section for bremsstrahlung; and μ(k) is the total photon attenuation cross section for the target material (cm^2/atom).

If the target is thin enough to allow the energy loss of the electron to be neglected, then the differential bremsstrahlung cross section can be treated as a constant. The integral in equation (3.5) may then be evaluated. Integrating over the effective target thickness, the resulting expression can be solved for the detector efficiency ϵ(k) to give

$$\epsilon(k) \propto \frac{y_{net}}{\Delta\Omega\,\Delta k \left(\frac{d^2\sigma}{d\Omega\,dk}\right) h\,T(k)}, \tag{3.5}$$

where T(k) is the average photon transmission from all depths in the target:

$$T(k) = \frac{1-e^{-\left(\frac{\mu(k)t}{\sin\psi}\right)}}{\left(\frac{\mu(k)t}{\sin\psi}\right)}. \tag{3.6}$$

To evaluate T(k), tabulated values can be used for μ(k), or alternatively, the product μ(k)t can be determined from attenuation measurements. For each of the thin targets, the measured background-corrected bremsstrahlung spectrum was substituted in equation (3.6) along with the appropriate curve for the differential AFB cross section and the experimentally determined average photon transmission, T(k), to evaluate the detector efficiency. Note that the efficiency

could only be extracted from the regions of each spectrum where no characteristic x-ray lines were present. The circles of figure 3.8 show the intrinsic efficiency curve calculated by this AFB method.

These bremsstrahlung measurements gave the relative efficiency of the detector, which was then normalized to the PIXE data and radioactive source results. Table 3.3 shows the tabulation of these results. Once the intrinsic efficiency is determined, the absolute efficiency for the experimental arrangement of the detector may be determined. Using a calibrated radioactive source of ^{57}Co to measure the absolute efficiency for 6.4 keV for the K_α x-ray, the relative efficiency curve can be normalized to this point to get the absolute efficiency. For the present experiment, the region of interest is from the M_γ (1.576 keV) x ray down to M_ζ (1.045keV) x ray for $_{67}$Ho. It is estimated that the uncertainty in the absolute efficiency in this region should be at least to ±12-16%.

3.3 Target Preparation

Thin holmium targets were made by evaporating HoF_3 onto 5-10 $\mu g/cm^2$ self-supporting carbon foils. In order to reduce the bremsstrahlung background, 5 $\mu g/cm^2$ carbon foils were used. The targets were as thin as possible for three reasons, (i) the energy loss of the ion as it passes through the target is minimized, (ii) self-attenuation of the x rays produced below the surface of the target is also minimized, and (iii) most importantly, the alteration of the charge state of the incoming ion is minimized so that the charge state dependence measurements are possible.

The carbon backing foils were prepared by a method [42, 58, 67-69] developed at UNT to avoid interference of K or L x-rays from impurity elements

Table 3.3. The relative efficiency data table of the windowless Si(Li) x-ray detector.

E (keV)	Efficiency	E (keV)	Efficiency	E (keV)	Efficiency
0.55	0.573	1.00	0.822	1.45	1.019
0.56	0.577	1.01	0.829	1.46	1.020
0.57	0.581	1.02	0.837	1.47	1.022
0.58	0.585	1.03	0.844	1.48	1.024
0.59	0.589	1.04	0.851	1.49	1.026
0.60	0.594	1.05	0.857	1.50	1.027
0.61	0.598	1.06	0.864	1.51	1.029
0.62	0.602	1.07	0.870	1.52	1.030
0.63	0.607	1.08	0.877	1.53	1.032
0.64	0.611	1.09	0.883	1.54	1.033
0.65	0.616	1.10	0.889	1.55	1.034
0.66	0.621	1.11	0.894	1.56	1.035
0.67	0.625	1.12	0.900	1.57	1.036
0.68	0.630	1.13	0.906	1.58	1.037
0.69	0.635	1.14	0.911	1.59	1.038
0.70	0.640	1.15	0.916	1.60	1.039
0.71	0.644	1.16	0.921	1.61	1.040
0.72	0.649	1.17	0.926	1.62	1.041
0.73	0.654	1.18	0.931	1.63	1.042
0.74	0.659	1.19	0.936	1.64	1.043
0.75	0.665	1.20	0.940	1.65	1.043
0.76	0.670	1.21	0.945	1.66	1.044
0.77	0.675	1.22	0.949	1.67	1.045
0.78	0.680	1.23	0.953	1.68	1.045
0.79	0.686	1.24	0.958	1.69	1.046
0.80	0.691	1.25	0.962	1.70	1.046
0.81	0.696	1.26	0.965	1.71	1.047
0.82	0.702	1.27	0.969	1.72	1.047
0.83	0.707	1.28	0.973	1.73	1.048
0.84	0.713	1.29	0.976	1.74	1.048
0.85	0.719	1.30	0.980	1.75	0.938
0.86	0.725	1.31	0.983	1.76	0.938
0.87	0.730	1.32	0.986	1.77	0.939
0.88	0.736	1.33	0.989	1.78	0.939
0.89	0.742	1.34	0.992	1.79	0.939
0.90	0.748	1.35	0.995	1.80	0.939
0.91	0.754	1.36	0.998	1.81	0.939
0.92	0.760	1.37	1.000	1.82	0.939
0.93	0.766	1.38	1.003	1.83	0.939
0.94	0.774	1.39	1.006	1.84	0.939
0.95	0.783	1.40	1.008	1.85	0.940
0.96	0.791	1.41	1.010	1.86	0.940
0.97	0.799	1.42	1.012	1.87	0.940
0.98	0.807	1.43	1.015	1.88	0.940
0.99	0.815	1.44	1.017	1.89	0.940

in the M x-ray region of interest. Since the targets were very thin, impurities on the target foil, especially sodium and silicon, became a concern. The self-supported carbon substrate was obtained from a commercial manufacturer, who arc-evaporated carbon onto a glass slide that had been treated with a parting agent. The parting agent will dissolve in water, freeing the carbon from the glass slide and allowing the foil to be transferred to an aluminum frame. The parting agent and the water used to dissolve this agent have been considered to be the major source of impurities. When evaporated in this manner, the carbon foil is a chemically active surface, which readily adsorbs impurities. To reduce the impurity level, a procedure described by Weathers *et al.* [68] was followed. The parting agent was dissolved in deionized water at ~50°C, freeing the carbon foil. A cleaning procedure to reduce these impurity was then undertaken. First, the foils were floated onto a 5 % acetic acid solution, and placed into an ultrasonic bath for 4 minutes. The foil was then transferred to a fresh solution using a clean glass slide, and the ultrasonic bath treatment was repeated twice. Finally, the foil was transferred to a deionized water solution before being picked up on the target frame. The carbon foil was then placed in the evaporator and sputter-cleaned for 1 minute in a 40 mTorr argon atmosphere.

To remove the majority of the contaminants, carbon foils were washed in an ultrasonic cleaner filled with ultrapure water spiked with acetic acid. However, the survival rate of the foils in the ultrasonic cleaner was less than 25% [42]. By coating the carbon foil with collodion before floating the foil off the glass slide, the survival rate was increased in the ultrasonic cleaner to almost 100%. Collodion is cellulose dissolved in amylacetate. Because the collodion evaporates rapidly from the spot where the ion beam strikes the target, the volatile

contaminants in the collodion were also removed. Carbon foils as thin as 1 $\mu g/cm^2$ may be processed in this manner.

The effectiveness of this cleaning process was then analyzed by using PIXE. Blank carbon foils that had been floated in deionized water were compared to foils that had been cleaned with the procedure described above. Figure 3.10 shows the x-ray spectra of (a) uncleaned and (b) cleaned carbon foils bombarded by 2 MeV protons. Figure 3.11 shows the comparison of results of this cleaning procedure. As can be seen, this procedure reduced the concentration of light element impurities substantially.

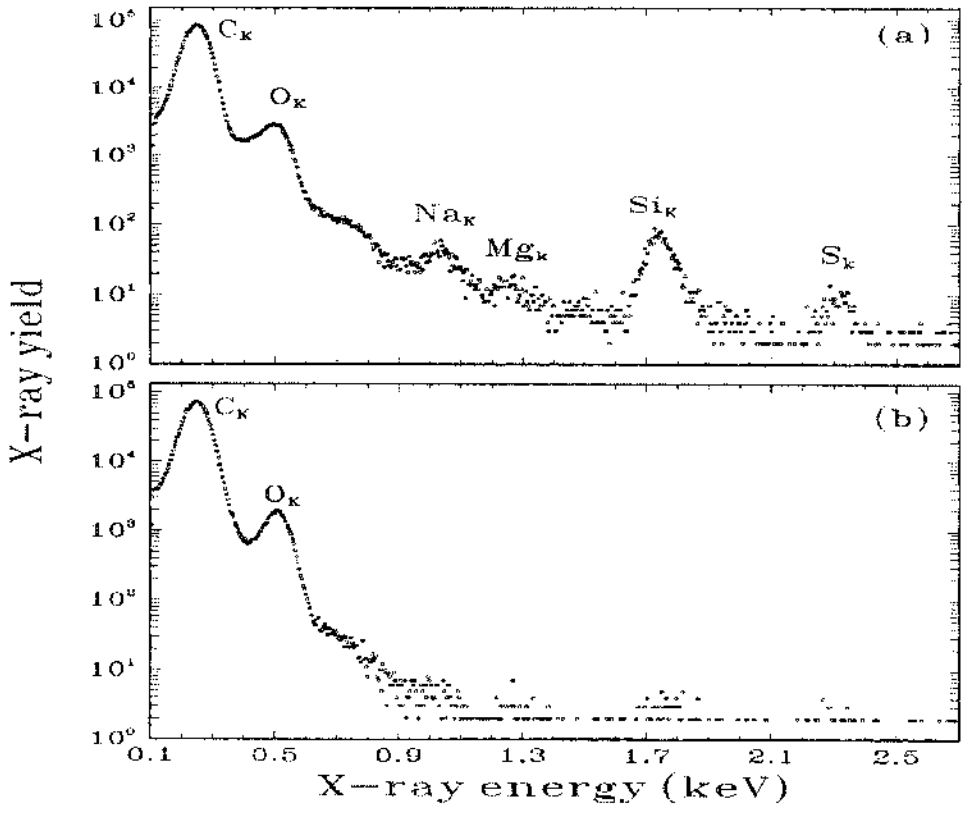

Figure 3.10 X-ray spectra of (a) uncleaned and (b) cleaned carbon foils bombarded by 2 MeV protons.

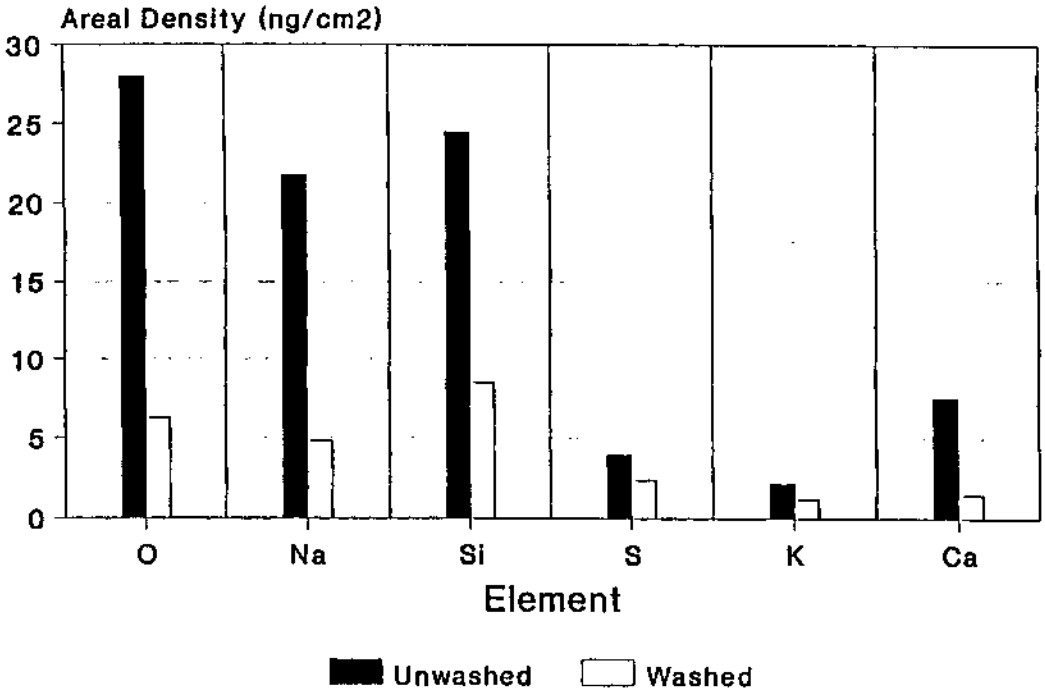

Figure 3.11 Comparison of light element concentrations for cleaned (washed) and uncleaned (unwashed) blank carbon foils (ref: [126]).

CHAPTER 4

DATA ANALYSIS AND REDUCTION

4.1 X-ray Spectrum Analysis

Figure 4.1 shows a diagram of the primary electronic transitions to the M-shell from higher atomic orbitals. Some of these transitions can not be separated in energy because of the limited resolution of the Si(Li) detector. Figure 4.2(a) shows the measured pulse height spectrum obtained from our previously published work [65] for 2 MeV protons on a thin HoF_3 target. The $_6$C-K (282 eV) and $_8$O-K (523 eV) x-ray peaks are from the oxidized carbon foil and the $_9$F-K (677 eV) x ray are from the HoF_3 target. The $_{14}$Si-K (1.74 keV) peak results from the Si(Li) x-ray detector being fluorescenced by either back scattered protons that managed to evade the deflection magnet in front of the x-ray detector (see fig. 3.5) or photons with energy greater than the Si K binding energy (1.84 keV). The three $_{67}$Ho M x rays of interest are the M_ζ, $M_{\alpha\beta}$, and M_γ peaks. With the non-linear least square curve fitting program, GUPIX [116], the area beneath the three M x-ray peaks can be easily extracted from the x-ray spectrum given in figure 4.3(a). The situation becomes more complex when the projectiles are carbon ions as is seen in figure 4.2(b). There are several effects that take place that tend to mask the peaks of interest. The most pronounced of these effects is the carbon-ion-induced bremsstrahlung produced by the target backing. This background is seen for all of the energies of interest in present work.

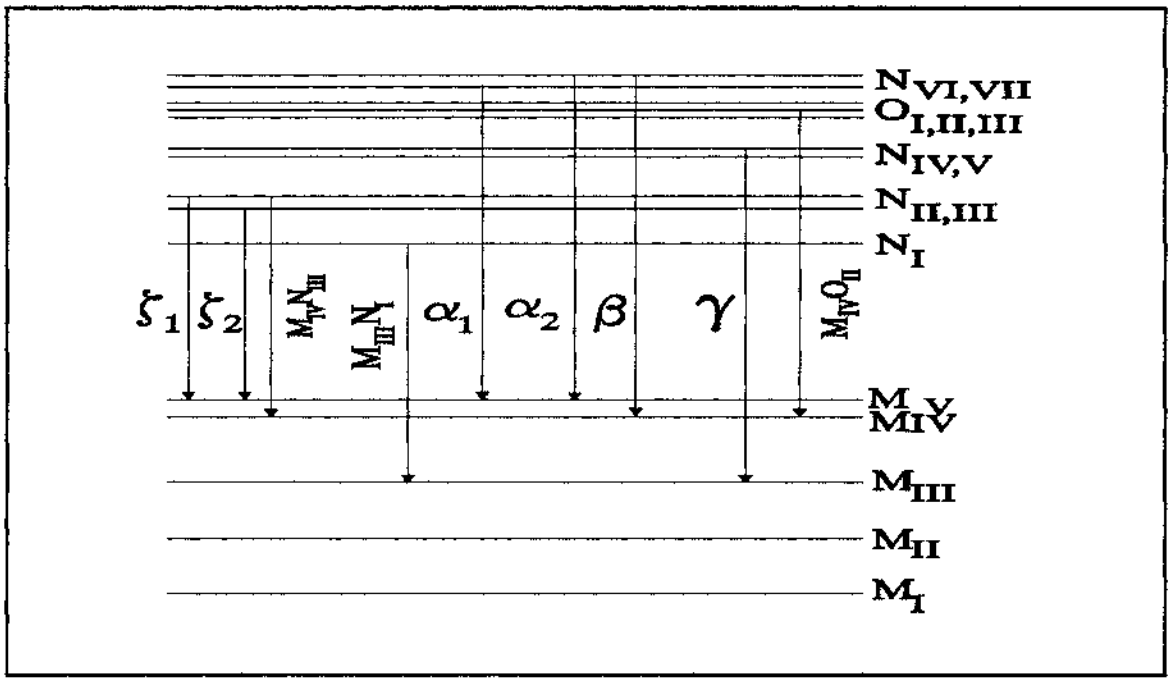

Figure 4.1 Diagram of all the possible electron transitions for the M shell.

Bremsstrahlung

For x-ray measurements, Folkman [131] mentioned that the characteristic x-ray peaks are always superimposed on a continuous background of electromagnetic radiation which is either (1) bremsstrahlung from secondary electrons, (2) bremsstrahlung from the projectiles, (3) Compton scattering of γ-rays, or (4) from contaminant characteristic x-ray peaks. The secondary electron bremsstrahlung causes the largest contribution to the background. The higher the atomic mass and energy of the incident projectile ions, the higher the level of bremsstrahlung in the x-ray spectrum. This high yield of bremsstrahlung produced by heavy ion collisions gives a problem for the detector system. When the counting rate were too high, the dead time for the x-ray measurement became

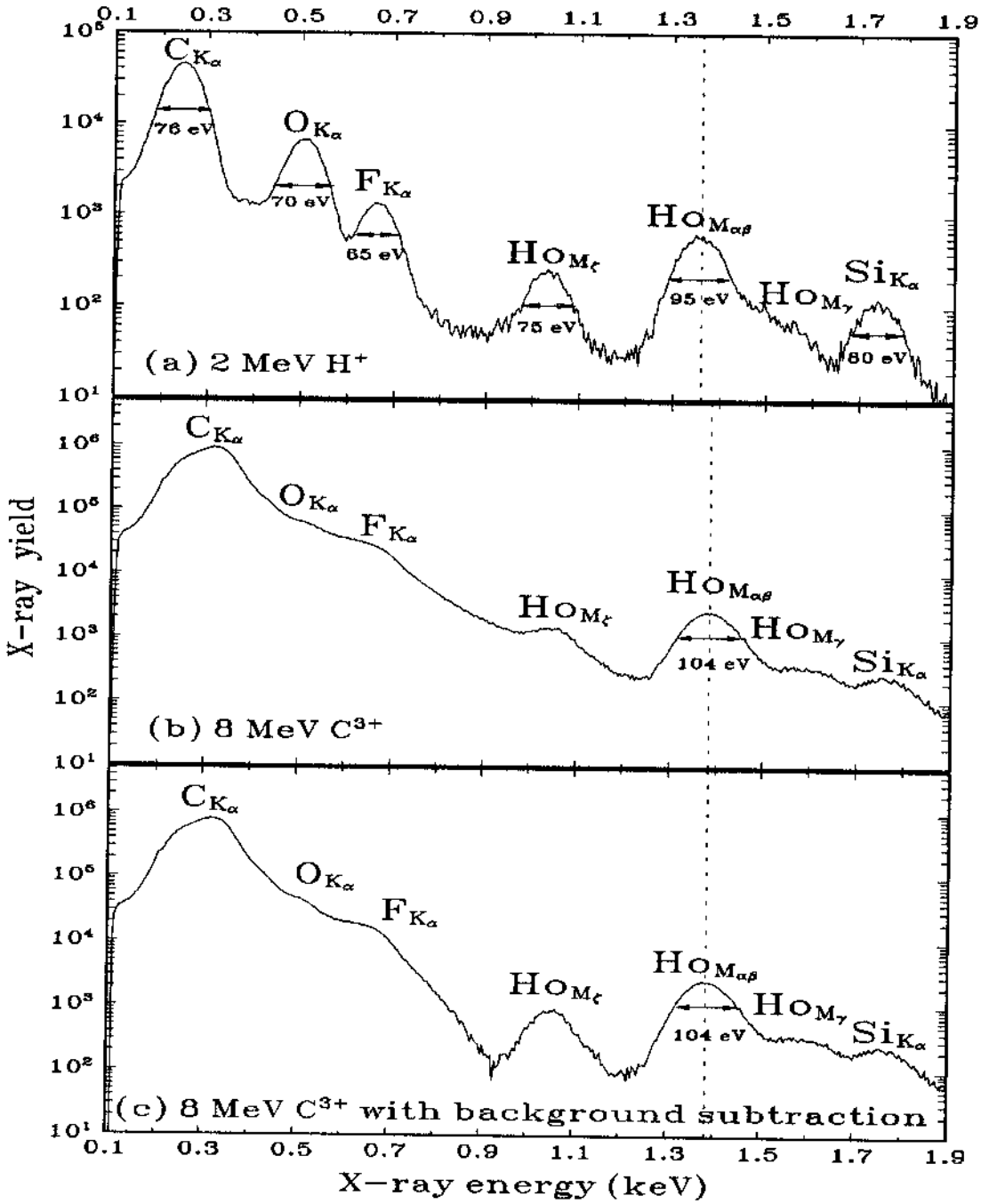

Figure 4.2 (a) and (b) are x-ray spectra of HoF_3 produced by 2 MeV H^+ and 8 MeV C^{3+} bombardment, respectively, (c) is a spectrum of (b) with the bremsstrahlung background subtracted.

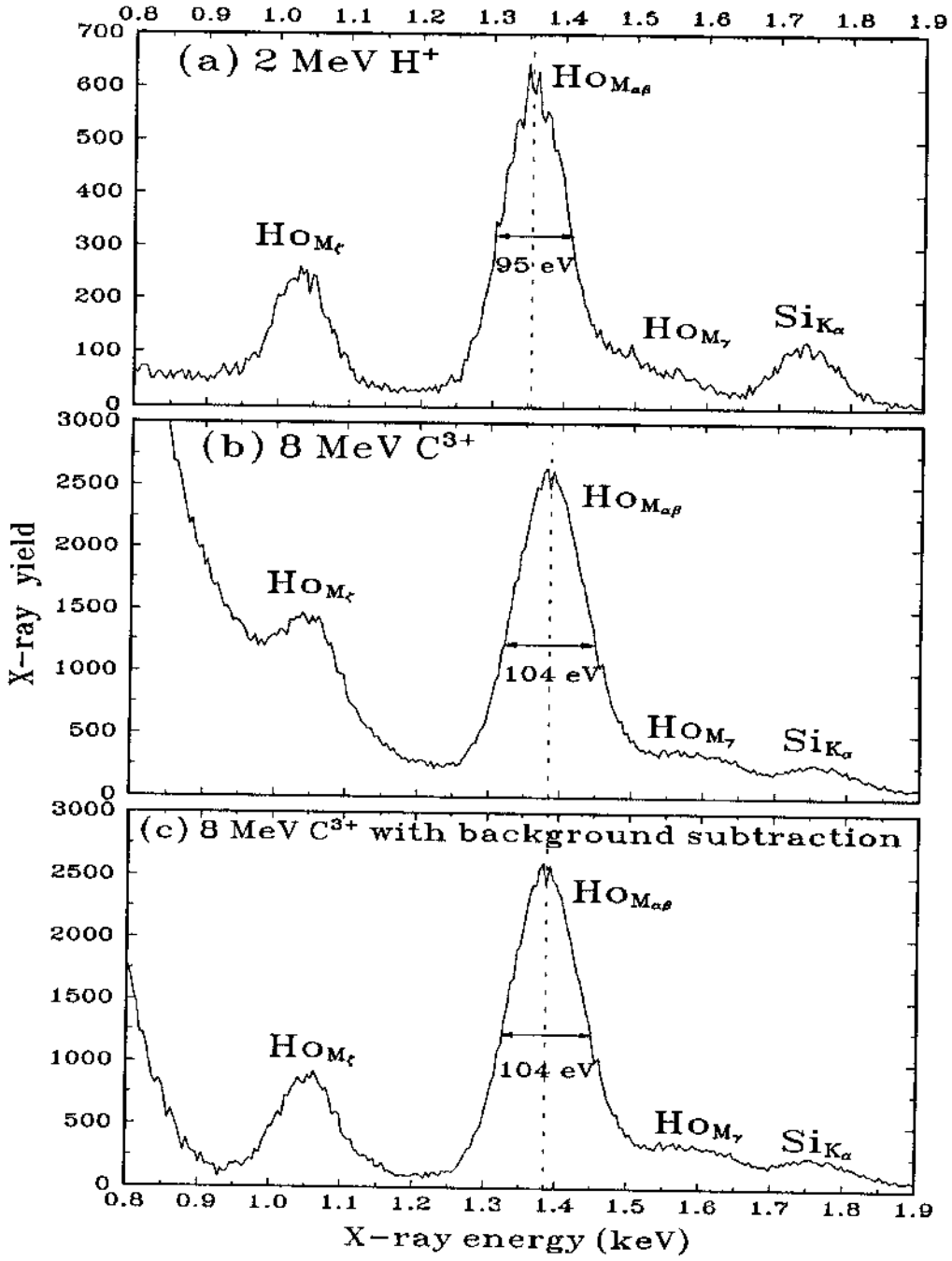

Figure 4.3 (a), (b), and (c) are x-ray spectra in linear scale for Ho M-shell x-ray region of figure 4.2.

large, and the pulse pile-up effects gave high background in x-ray spectrum. For the present experiment, reducing the beam current on the target decreased the total count rate which in turn lowered the background in the x-ray spectrum. However, reducing the beam current had the disadvantage of prolonging the time needed in getting a good counting statistics in the RBS spectrum from vanishingly thin target. In order to reduce the background further, it was necessary to measure the background spectrum produced by the carbon foil to subtract it from the target x-ray spectrum.

Figure 4.4 shows the measured bremsstrahlung background for a thin carbon foil as a function of incident carbon energy. From the figure, it can be seen that the bremsstrahlung spectrum extends out to about 1.3 keV for 2 MeV carbon ions and to almost 2.1 keV for 12 MeV carbon ions. There is obviously some bremsstrahlung produced by the HoF_3 part of the target but for the charge state dependence studies, with 0.34 $\mu g/cm^2$ Ho targets, this background bremsstrahlung was certainly minimized.

The other effects that tend to complicate the $_{67}$Ho pulse height spectrum shown in figure 4.2(b) and 4.3(b) are the long x-ray tails from the carbon backing and the broadening and shifting of the peaks to higher energies, probably due to some small amount of multiple ionization. In order to account for the tailing and bremsstrahlung effects, the appropriate carbon foil spectrum shown in figure 4.4 was subtracted from the pulse height spectrum for the carbon plus HoF_3 foil in figure 4.2(b) to give the result shown in figure 4.2(c) and 4.3(c). The resultant pulse height spectrum shows a pronounced M_ζ peak and, with the GUPIX x-ray stripping program, $M_{\alpha,\beta}$ and M_γ could be extracted.

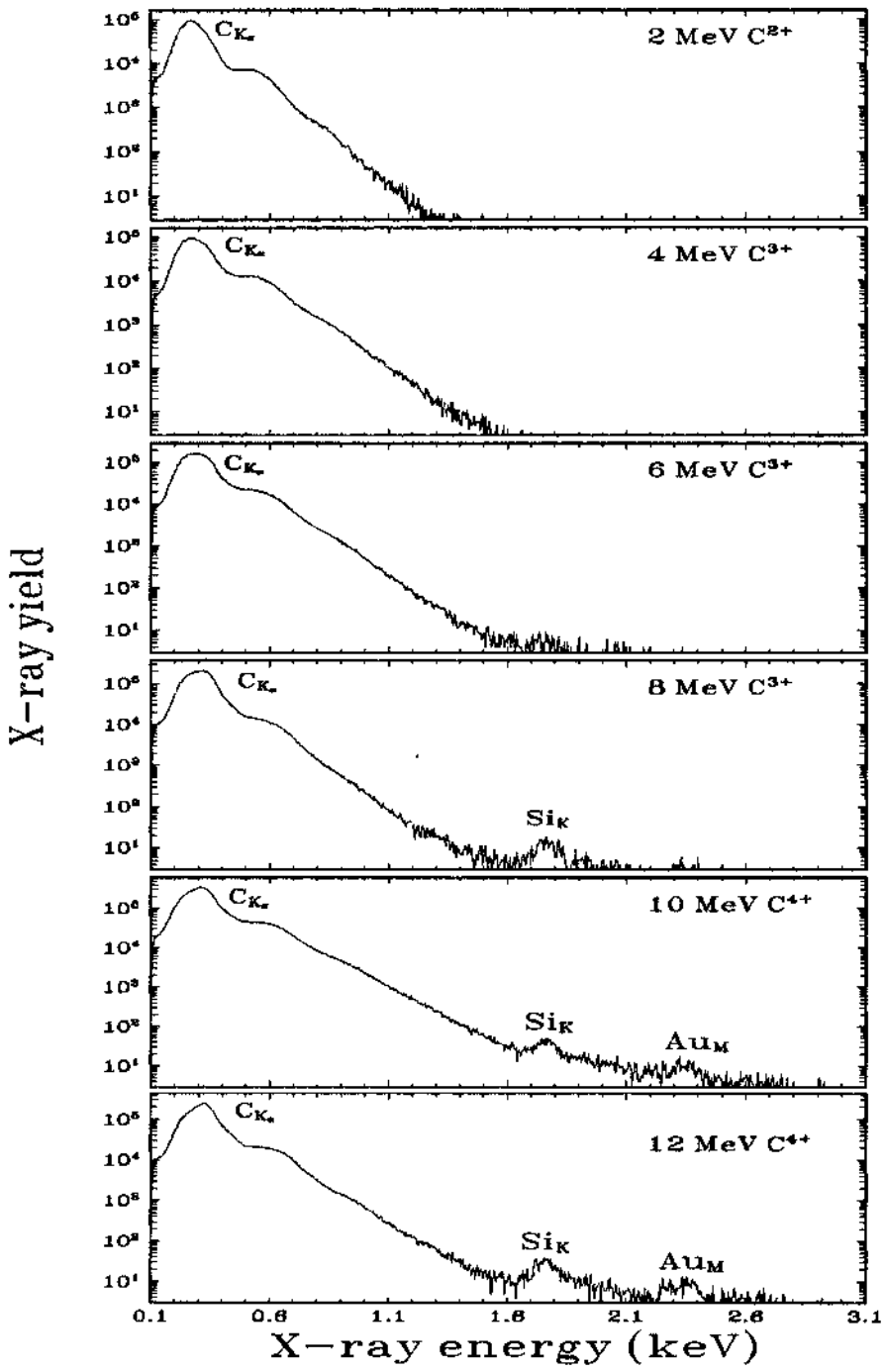

Figure 4.4 The background spectra from a carbon foil for 2-12 MeV carbon ions bombardment.

Multiple Ionization and Energy Shifts

Multiple ionization can be explained as simultaneous loss of several target electrons via direct ionization and electron capture processes by the incident projectiles. This implies an additional change of the electron configuration and as a consequence, a possible change of the fluorescence yield. Benka [132] and Czuchlewski *et al.* [133] explained that additional inner-shell vacancies may increase the fluorescence yield by reducing the probability for Auger transitions. The single hole fluorescence yield is inadequate when a large amount of multiple ionization of the target atom is caused by heavy ion impact. Multiple ionization may influence the chemical binding effect since it reduces the screening of the nuclear charge by electrons and generates specific energy levels. Oslen *et al.* [134] showed that the multiple inner-shell vacancies produced by heavy ion-atom collisions can cause the energy shift of the emitted x rays. The energy shifts increase with atomic number and the energy of the projectile.

As can be seen from figure 4.3, the $M_{\alpha\beta}$ peak goes from a FWHM of 95 eV for incident protons to 104 eV for 8 MeV carbon ions. It is also observed that the $M_{\alpha\beta}$ peak is shifted by ~30 eV to higher energies when bombarded by carbon ions. Both of these phenomena indicate that there is some small amount of multiple ionization that is taking place. The main question to be answered is whether this degree of multiple ionization changes the effective fluorescence yield, which would in turn give a different value for the inner-shell ionization cross section, σ_I, since $\sigma_X = \omega\sigma_I$, where σ_X is the x-ray production cross section and ω is the x-ray fluorescence yield. As it turns out, there is no exhaustive set of data in the literature to make the case either way [135, 136]. Multiple ionization as well as the x-ray fluorescence yield vary with the type of primary ion and depend on its

charge state and energy. Tawara *et al.* [137] showed that the K-shell fluorescence yield was fairly constant for a solid ^{28}Si target but did show variation for SiH_4 gas targets for incident $^{9}F^{q+}$ ions. A host of other studies have been made [89, 135, 138, 139] but the most convincing set of experimental data for the current case was presented by Tunnell *et al.* [140]. In this study, they showed the energy dependence of the fluorescence yield of a solid Ti target for incident ions $_{1}H$ through $_{17}Cl$ with projectile energies 0.5 through 4.5 MeV/u. It was observed that for incident ^{12}C ions, ω varied from 0.225 to 0.243. This is only an 8% variation and hence not a serious problem. But it is obvious that further study is required to gain deeper insight for the observed variations of fluorescence yields.

In the experiment, when the measured x-ray cross sections are reduced to inner-shell ionization cross sections, the uncertainty of the fluorescence yields should be taken into account if it is well known. For the M-shell x-ray production, the M-shell fluorescence yields are more complicated than the ones of K and L shells and are still not well measured for each projectile-target pair. In this thesis, single-hole fluorescence yields [3] were used to reduce x-ray production cross sections to ionization cross sections.

4.2 X-ray Production Cross Section Calculation

The x-ray production cross section, σ_X, can be experimentally calculated using the relation

$$\sigma_X = \frac{Y_X\, t_X}{N_1 N_0 \epsilon_X A_X}, \tag{4.1}$$

where Y_X is x-ray yield; t_X is the dead time correction (real time/live time) for the

x-ray measurement; ϵ_X is the absolute efficiency that includes the intrinsic efficiency and the solid angle as mentioned in section 3.2 of the x-ray detector; N_1 is the number of incident ions that can be determined from the integrated charge in the Faraday cup (see fig. 3.5) if the entering charge state fractions are well known; N_0 is target thickness (atoms/cm^2) that represents the number of target atoms; and A_X is correction factor for self-absorption of target x rays, which depends on the target thickness. Since the target thickness must be exactly measured and the equilibrium charge state of the ion beam entering the Faraday cup must be well known, the usefulness of equation (4.1) is limited to a normalization role.

An alternative approach for determining the x-ray production cross section exists when the scattering of the incident ion by the target atom is known to obey the Rutherford scattering law. The experimental Rutherford scattering cross section is given as

$$\sigma_R = \frac{Y_R t_R}{N_1 N_0 \Delta\Omega}, \tag{4.2}$$

where Y_R is backscattering particle yield, $\Delta\Omega$ is solid angle of the particle detector, and t_R is the dead time correction for the RBS measurement. By simultaneously measuring x-rays and scattered particles and taking t_R=1 because of very low counting rate, the x-ray production cross section is calculated using equation (3.1),

$$\sigma_X = \frac{Y_X \sigma_R \Delta\Omega t_X}{Y_R \varepsilon_X A_X}.$$

If equation (4.1) and (4.2) are combined and the term N_0N_1 can be eliminated.

This simultaneous measurement minimized nonuniform target thicknesses as well as charge integration uncertainties because of charge state changes of the ion in passing through the HoF_3 and carbon foil.

Anisotropy Property of X Rays

The assumption of isotropic x ray emission may not be true for the present M-shell measurement. The anisotropy of x rays resulted from the ion-induced inner-shell alignment. Both direct ionization and electron capture gave contributions to the inner-shell alignment. Jitschin [141] reviewed the alignment studies in inner-shell processes. For heavy projectile ions, he pointed out that the alignment effects became monotonously small in the high impact velocity region, $v_i/v_{2e}>0.1$, where v_i and v_{2e} denoted the projectile velocity and target inner-shell electron velocity, respectively.

Until now, no detailed experimental study has been performed for heavy-ion induced M-shell alignment for both DI and EC. In order to prove whether M-shell x rays are emitted isotropically, the angular dependence of M-shell x-ray emission yield need to be studied in future experiments.

Normalization Methods for the RBS Detector

As was mentioned earlier, the combination of vanishingly thin targets and low Rutherford backscattering for the high energy data gave long run times for each data point. Sometimes as much as a ten hour measurement period was required to obtain adequate statistics in the RBS peak. In order to overcome this problem, a small gold foil scattering chamber (see fig. 3.5) was placed in a position following the holmium+carbon target. The carbon ions therefore passed

through the holmium+carbon foil and then through the 200 $\mu g/cm^2$ gold foil before entering the Faraday cup. Since the holmium target and its carbon backing foil were very thin, the beam did not show an appreciable increase in diameter at the gold foil. Carbon ions that scattered from the gold foil were measured at 90° with a surface barrier detector with a fairly large solid angle. The ^{12}C scattering is Rutherford for all of the energies used for both holmium and gold, and hence the ratio of scattered ions in the holmium peak at 169° is always proportional to the gold Rutherford peak at 90°. The backangle RBS scattering of carbon ions at 169° and the gold RBS scattering of carbon ions at 90° were measured once for each carbon energy to obtain good counting statistics. Then, for the high energy carbon ions, this ratio could be used to renormalize the backangle scattering where statistics are poor.

Rutherford Scattering Cross section Calculation

The Rutherford backscattering cross section (in barns per sr) used in equation (3.1) can be calculated as a function of the laboratory scattering angle θ of the ion and its incident energy E_1 (in MeV) in the laboratory from [142]

$$\sigma_R(\theta) = \frac{d\sigma}{d\Omega} = \frac{\left(\frac{Z_1 Z_2 e^2}{4E_1}\right)^2 \frac{4}{\sin^4(\theta)} \left\{ \sqrt{\left[1-\left(\frac{M_1}{M_2}\sin(\theta)\right)^2\right]} + \cos(\theta) \right\}^2}{\sqrt{\left[1-\left(\frac{M_1}{M_2}\sin(\theta)\right)^2\right]}}, \tag{4.3}$$

where M_1 and Z_1 are the respective mass and atomic number of incident ion, and M_2 and Z_2 are the target mass and atomic number.

The derivation of the Rutherford scattering cross section is based on a Coulomb interaction potential between the projectile Z_1 and the target atom Z_2. For the experiment, scattering is due to the repulsion of two positively charged nuclei of atomic number Z_1 and Z_2. This may have deviations from the following two sources: (i) screening effects due to the surrounding electrons at low energy bombardment, or (ii) resonant nuclear scattering at high energy bombardment. In order to use the Rutherford scattering cross section shown in equation (4.3), it was necessary to estimate whether the RBS measurements are Rutherford scattering without interference.

For low energy heavy ion collisions, if the incident ion does not completely penetrate through the target electron shells, the innermost electrons screen the charge Z_2 of target atom and change the interaction potential. The scattering is then not Rutherford. Using an analytic approximation as a function of E_{CM}, the center-of-mass energy for the incident ion, by Andersen *et al.* [143], the screening effects can be included to give the scattering cross section

$$\sigma_{SCREEN} = \sigma_R \frac{[1+y]^2}{\left\{1+2y+\left[\frac{y}{\sin\left(\frac{\theta_{CM}}{2}\right)}\right]^2\right\}^2}, \tag{4.4}$$

where θ_{CM} is the center-of-mass scattering angle and $y=V_1/E_{CM}$, where

$$V_1 = 48.73 \frac{Z_1 Z_2}{\left(Z_1^{\frac{2}{3}}+Z_2^{\frac{2}{3}}\right)^{\frac{1}{2}}} (eV). \tag{4.5}$$

At high energies, when the energy of the ion is greater than the Coulomb barrier, which would generate nuclear resonances, the elastic scattering is non-Rutherford. The use of the Rutherford scattering cross section for x-ray normalization is then inadequate. Bozion *et al.* [144, 145] have developed a formula that predicts the energy where the scattering cross section begins to deviate significantly (>6%) from the Rutherford scattering cross section. The formula is given by

$$E_{NR} = \frac{\alpha_C \left[1 + \sin^{-1}\left(\frac{\chi}{2}\right)\right]}{-2R_0 \ln\left\{ \alpha_C \left[2\alpha_N \left(\frac{Z_1^2}{A_1}\right)^x \right]^{-1} \right\}}, \tag{4.6}$$

where E_{NR} and χ are the projectile kinetic energy and scattering angle in the center-of-mass frame, respectively, $R_0 = r_0 A_2^{1/3}$ with $r_0 = 1.3$ fm, $\alpha_C = 1.44\ Z_1 Z_2$ MeV-fm, $\alpha_N = 390$ MeV-fm, and $x = Z_1/Z_2$. Here, A_1 and A_2 are the mass numbers of the two nuclei involved in the collision.

4.3 X-ray Production Cross Section Produced by Electron Capture to the Ion

Electron capture contributions to the holmium M-shell x-ray production cross sections were calculated using the charge state dependence of the data for vanishingly thin targets approximating single collision conditions ($<1\mu g/cm^2$). Electron capture to the *n*-th (K-, L-, M-, ...) shell of an incident ion can only occur if the ion has a vacancy in that shell. In this case, the M-shell x-ray production cross section due to direct ionization (DI) plus electron capture (EC) for the carbon ion with charge state *q* is given by

$$\sigma_{MX}^{TOTAL(C^{q+})} = \sigma_{MX}^{DI} + \sigma_{MX}^{EC(C^{q+})} . \tag{4.7}$$

Since the direct ionization contribution are the same for carbon ions with different charge states assuming that the electron correlation effect between the projectile electron and the target electron is small, the M-shell x-ray production cross section due to electron capture to double K-vacancies in the carbon ion is given by

$$\sigma_{MX}^{EC(K\text{-}shell)} = \sigma_{MX}^{EC(K\text{-},L\text{-},M\text{-}...shells)+DI} - \sigma_{MX}^{EC(L\text{-},M\text{-}...shells)+DI} , \tag{4.8}$$

and the M-shell x-ray production cross section due to electron capture to one K-vacancy is given by

$$\sigma_{MX}^{EC(\frac{1}{2}K\text{-}shell)} = \sigma_{MX}^{EC(\frac{1}{2}K\text{-},L\text{-},M\text{-}...shells)+DI} - \sigma_{MX}^{EC(L\text{-},M\text{-}...shells)+DI} , \tag{4.9}$$

where ½K and K represent a half vacant and completely vacant K-shell for the incident carbon ion, respectively. This assumes the DI is the same and independent of the number of electrons on the ions.

Metastable States

A helium-like ion with one K-vacancy, which is at 1s2s metastable state, can be formed after passing through the post-accelerator stripper [146, 147]. If the metastable ion's lifetime is longer than its transient time to bombard the target, then this metastable ion with charge state q (=Z_2-2) may give some electron capture contributions similar to that of the q=1+ ion during collision. Depending on the gas target thickness, the percentage of ions left in a metastable

state can be 10-20% [39].

Electron Correlation

Electron-correlation effects refers to ionization of a target atom by a projectile carrying electrons. Usually, the incident electrons play a passive role in screening the projectile nuclear charge and, thus, decreases the ionization probability. However, an incident electron may also participate actively in the collision by ejecting a target electron in a binary electron-electron collision [148-150]. The effect of the electron carried by the projectile ion incident on the target electron, which corresponds to an increase in the ionization probability, may be considered as electron-correlation process. This process has been studied and proven by experiment. [151-155].

The inner-shell ionization probability due to direct Coulomb ionization for different charge state ions with same atomic mass may be different because of electron correlation. However, the contribution from the interaction between electrons is not comparable to that between projectile nucleus and target electron. Therefore, the electron-correlation effect is neglected in this study.

CHAPTER 5

RESULTS AND DISCUSSION

When a highly charged ion, such as a fully stripped carbon ion, enters a thick target it will lose or gain electrons until the rates are equal and the ion will continue through the target with an equilibrium charge state [156]. For the electron capture measurements discussed earlier, it is important that the incident ion be essentially in the single collision realm. This phenomenon can be studied by measuring the effective cross section of holmium target M-shell x-ray production for various charge states as a function of target thickness. Figure 5.1 shows the result for 8 MeV $^{12}C^{q}$ ions (q = 3+ to 6+) incident on $_{67}$Ho targets of thickness varying from 0.34 to 41 $\mu g/cm^2$. From figure 5.1, it can be seen that at a thickness of approximately 14 $\mu g/cm^2$ the cross section for all incident ions is constant (at about 40 kilobarns). Therefore, for targets thicker than 14 $\mu g/cm^2$ all incident $^{12}C^{3+-6+}$ ions reach an average equilibrium charge state. The most important region of figure 5.1 is the portion that shows the plateau for each charge state. From figure 5.1, it can be seen that for targets with thicknesses below ~2 $\mu g/cm^2$ the single collision condition is reached. To be certain of single collision conditions, all of the electron capture data reported in the present thesis were done for $_{67}$Ho target of 0.34 $\mu g/cm^2$ thickness. This thickness gives an areal density of 1.24×10^{15} atoms/cm^2, which is between 1 and 2 atomic layers.

The x-ray yield is a strong function of the target thickness. This fact was

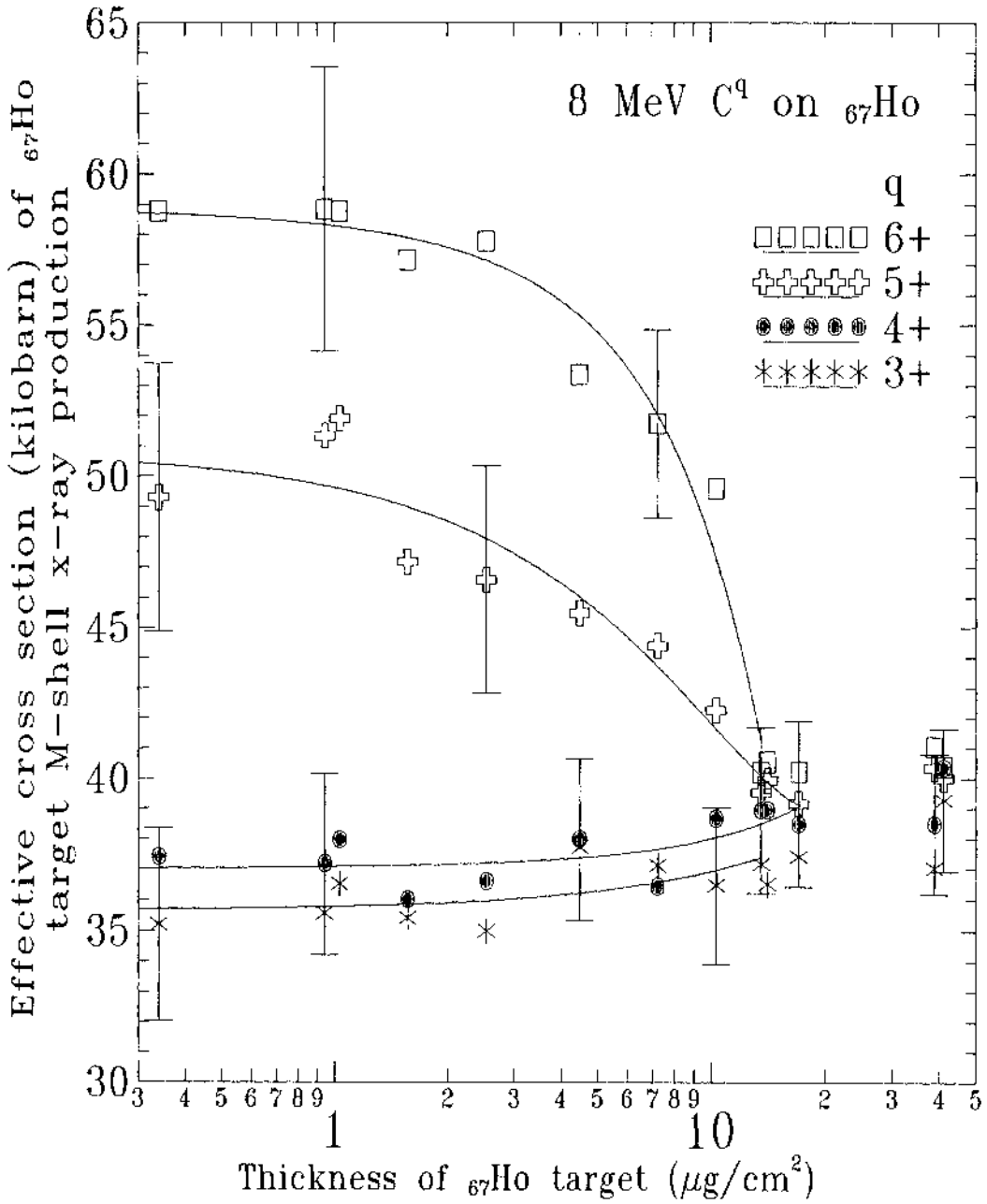

Figure 5.1 The effective cross sections of $_{67}$Ho target M-shell x-ray production by 8 MeV carbon ions for various charge state as a function of target thickness. The solid curves are polynomial fitting of data trend.

not included in most of the publications reported prior to 1976 or even in some papers published after 1976 [156]. The target thickness effect as a function of charge state was reported by Gray *et al.* [60] and McDaniel *et al.* [39] when they measured K-shell x-ray yields as a function of target thickness for projectiles with zero, one and two K-shell vacancies. They found that the variation in target x-ray production with its thickness could be explained in terms of the number of K-vacancies in the projectile. Hence, charge state dependence of the x-ray production cross section can be extracted in the limit of zero target thickness [156].

Figure 5.1 shows that the x-ray production at ~zero thickness depends on the charge state of the incident ion. Since direct ionization doesn't depend appreciably on the charge state of the ion if one neglects electron correlation effect (*note: electrons on the ion also produce a small amount of ionization as mentioned in chapter 4), this effect must be due to the electron capture process. As discussed in chapter 2, when the ion goes through the target, it is possible for the target electron to be captured to a bound state of the ion if a vacancy exists in the ion. When the ion velocity approximately matches the target electron velocity, the capture probability is near maximum. The probability that such a transfer occurs depends on the number of vacancies in the ion and the energy levels involved.

Table 5.1 contains a comprehensive summary of all of the data measured for this thesis. It includes the M_ζ, $M_{\alpha,\beta}$, and M_γ x-ray contributions and the total M-shell x-ray production cross sections. The experimental uncertainties were computed from all terms related to the experiment. For the measured efficiency of the x-ray detector, the error was estimated to be 12-16% after calibration by

Table 5.1 M-shell x-ray production cross sections (in kilobarn) of $_{67}$Ho by $^{12}_{6}C^{q}$ ions with energies, E_1, from 2 to 12 MeV, in charge state q. $\sigma_{M(\zeta)}$, $\sigma_{M(\alpha,\beta)}$, and $\sigma_{M(\gamma)}$ are experimental x-ray production cross sections of M_ζ, $M_{\alpha,\beta}$, and M_γ, respectively, which were extracted from x-ray spectrum after GUPIX program [116] curve fitting. σ_{MX} is the measured M-shell x-ray production cross section and σ_{MX}^{ECPSSR} and σ_{MX}^{FB} the theoretical calculation of M-shell x-ray production cross sections for the ECPSSR theory and the first Born approximation, respectively. The inner-shell ionization cross section of the M-shell, σ_{MI}, can be calculated by $\sigma_{MI}=\sigma_{MX}/\omega_{MX}$, with $\omega_{MX}=0.011$ [3] as an effective M-shell x-ray fluorescence yield in $_{67}$Ho.

E_1	q	$\sigma_{M(\zeta)}$	$\sigma_{M(\alpha,\beta)}$	$\sigma_{M(\gamma)}$	σ_{MX}	$\sigma_{MX}/\sigma_{MX}^{FB}$	$\sigma_{MX}/\sigma_{MX}^{ECPSSR}$
2	2	0.43±0.07	2.55±0.37	0.12±0.03	3.10±0.38	0.29	4.07
2	3	0.46±0.08	2.62±0.38	0.12±0.04	3.20±0.39	0.28	4.11
2	4	0.57±0.09	2.68±0.37	0.11±0.04	3.36±0.38	0.28	4.24
4	2	1.55±0.20	9.03±1.04	0.44±0.08	11.0±1.1	0.29	1.41
4	3	1.84±0.28	9.21±1.19	0.59±0.12	11.6±1.2	0.29	1.44
4	4	1.89±0.34	9.26±1.20	0.60±0.15	11.7±1.3	0.27	1.41
4	5	3.37±0.49	14.3±1.59	0.86±0.17	18.6±1.7	.076	0.40
4	6	5.53±1.29	22.5±4.23	1.33±0.49	29.4±4.4	.066	0.35
6	3	3.55±0.54	15.9±1.97	1.59±0.30	21.0±2.1	0.32	1.00
6	4	3.94±0.51	16.1±2.08	1.62±0.32	21.7±2.2	0.31	1.00
6	5	5.96±0.81	24.3±2.68	2.88±0.37	32.6±2.8	0.12	0.47
6	6	8.34±1.13	33.3±3.57	3.27±0.69	45.0±3.8	.097	0.38
8	3	6.68±0.83	25.8±3.41	2.87±0.47	35.4±3.5	0.43	1.06
8	4	6.81±0.95	26.8±3.65	3.02±0.67	36.6±3.8	0.43	1.07
8	5	8.78±1.59	35.1±5.11	3.69±0.82	47.6±5.4	0.18	0.56
8	6	11.4±1.59	42.5±5.77	4.67±0.92	58.6±6.1	0.13	0.43
10	3	9.43±1.40	30.4±3.95	3.24±0.51	43.1±4.2	0.46	0.96
10	4	10.3±1.52	32.0±4.22	3.50±0.70	45.8±4.5	0.47	0.95
10	5	12.0±1.81	36.4±4.80	4.32±0.84	52.7±5.2	0.20	0.56
10	6	16.0±2.41	45.8±6.22	5.16±1.19	67.0±6.8	0.16	0.47
12	4	10.5±1.91	40.5±5.76	4.25±0.68	55.2±6.1	0.52	0.97
12	5	10.5±3.04	45.5±6.37	4.75±0.73	60.7±7.1	0.23	0.59
12	6	15.8±3.96	51.1±9.57	7.54±1.66	74.5±10.5	0.18	0.51

several methods. The solid angle of the particle detector was measured by ^{241}Am source with a 1.3% uncertainty. Since the current studies are considerably below the Coulomb barrier at 205 MeV calculated from equation (4.6), the scattering is assumed to be surely Rutherford in nature. The screening effect at 2 MeV was estimated from equation (4.4) as 0.5%. The error in the backscattering cross section is below 2% after considering the beam energy fluctuation. The uncertainty in the number of backscattered particles increased with the projectile energy from 3% to 7% due to counting statistics. The curve fitting procedure for the x-ray spectra was the major source of uncertainties. To minimize the uncertainties, the following precautions were taken. The long tail of the carbon K x-ray peak was subtracted from the M_ζ peak. Similarly, the M_γ peak had to be stripped from the pronounced $M_{\alpha\beta}$ peak. The Si K_α peak was also subtracted from the M_γ region. Hence, as shown in table 5.1, the uncertainties associated with each x-ray, ranged from 14 to 37%. The uncertainty from M-shell x-ray isotropy which is not clear at this impact velocity range for carbon ion was not estimated. Also shown in table 5.1 are the ratios of experimental M-shell x-ray production cross sections to the theoretical calculations of the first Born and ECPSSR theories for $^{12}C^q$ (q = 2+ to 6+) and carbon ion energies between 2 and 12 MeV.

Figure 5.2 shows the projectile charge state dependence of the total M-shell x-ray production cross sections of $_{67}Ho$ for 2 to 12 MeV carbon ions. The cross sections for q=2+ to 4+ are almost flat, indicating that the electron capture contribution for carbon ions without K vacancies is small. For carbon ions with K vacancies (q=5+ and 6+) the M-shell x-ray production cross section jumps from 10% (at 12 MeV q=5+) to 150% (at 4 MeV q=6+) compared to the data for

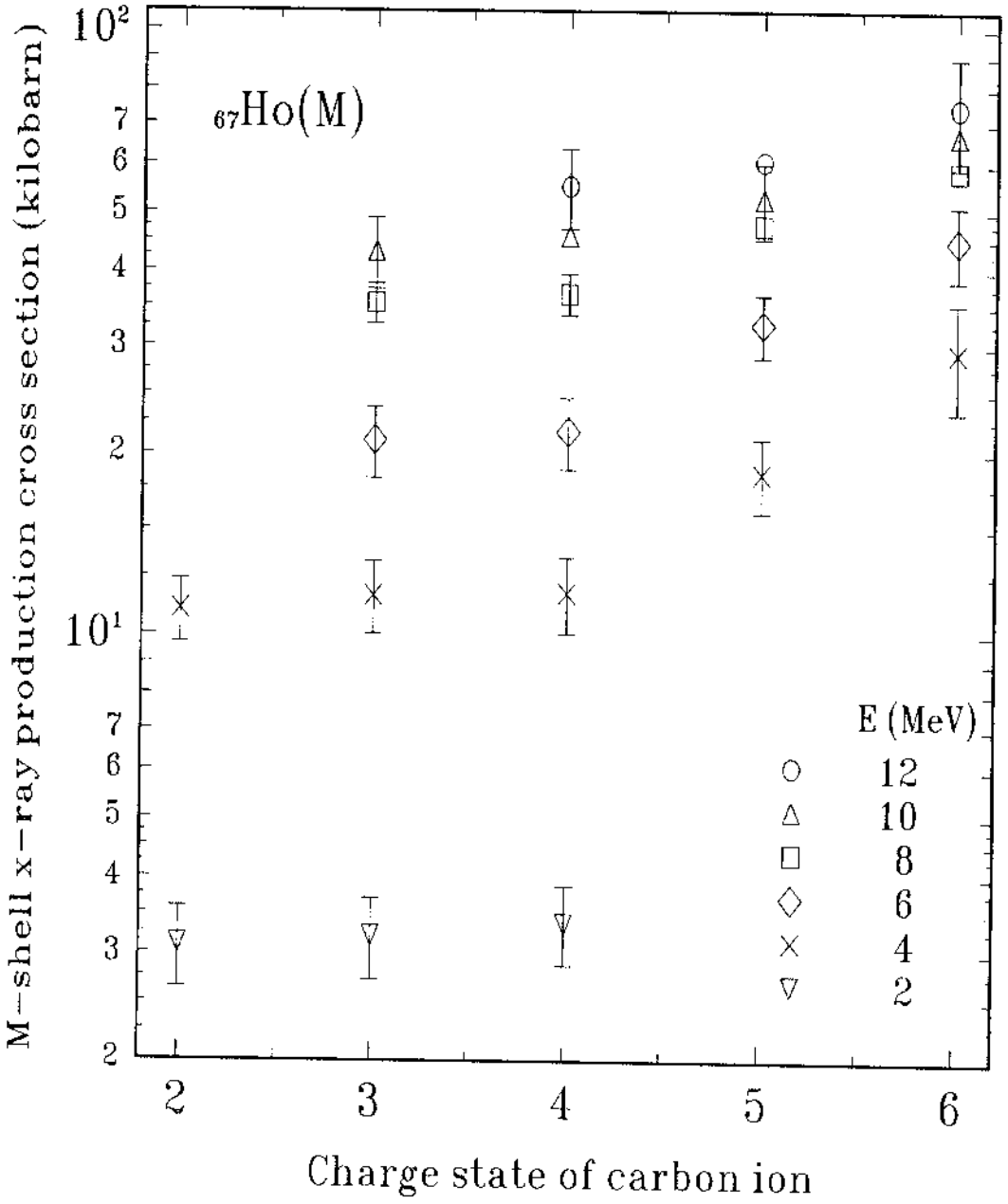

Figure 5.2 Charge state dependence of M-shell x-ray production in a 0.34 $\mu g/cm^2$ $_{67}$Ho target for 2-12 MeV carbon ions in charge state from 2+ to 6+.

q=4+.

Figure 5.3 shows a plot of the M-shell x-ray production cross section as a function of energy for four charge states used in this study. Also shown in the figure are the theoretical predictions of the first Born and ECPSSR theories. It can be seen that the ECPSSR theory fits the charge state 3+ and 4+ data (DI+EC) quite well for the carbon energies of from 6 to 12 MeV and overpredicts the data at lower energies. However, it overpredicts the charge state 5+ and 6+ data at all energies by 170–290%. The first Born approximation is seen to overpredict all the experimental data at all energies by a significant amount up to 15 times.

In the appendix, M-shell ionization and x-ray production cross sections of $_{67}$Ho bombarded by carbon ions with charge state from 2+ to 6+ are tabulated for the first Born approximation and the ECPSSR theory that include the contribution of both direct ionization and electron capture.

Table 5.2 shows a tabulation of all the measured M-shell x-ray production cross sections for electron capture and the corresponding ECPSSR and first Born theories. In table 5.2, the M-shell x-ray production cross sections for all the q=4+ data of 2 to 12 MeV and for all the q=3+ data of 2 to 10 MeV were used for subtraction. These electron capture contributions were obtained by subtracting the M-shell x-ray production cross sections for q=3+ or 4+ from those of q=5+ and 6+ as mentioned in section 4.2 using equations (4.8) and (4.9). This difference should give the contribution of electron capture into the hydrogen-like (q=5+) or bare (q=6+) carbon ions. Figure 5.4 shows the extracted electron capture cross sections for carbon ions with charge states 5+ and 6+. The results with q=4+ subtracted from the data may be lower than the

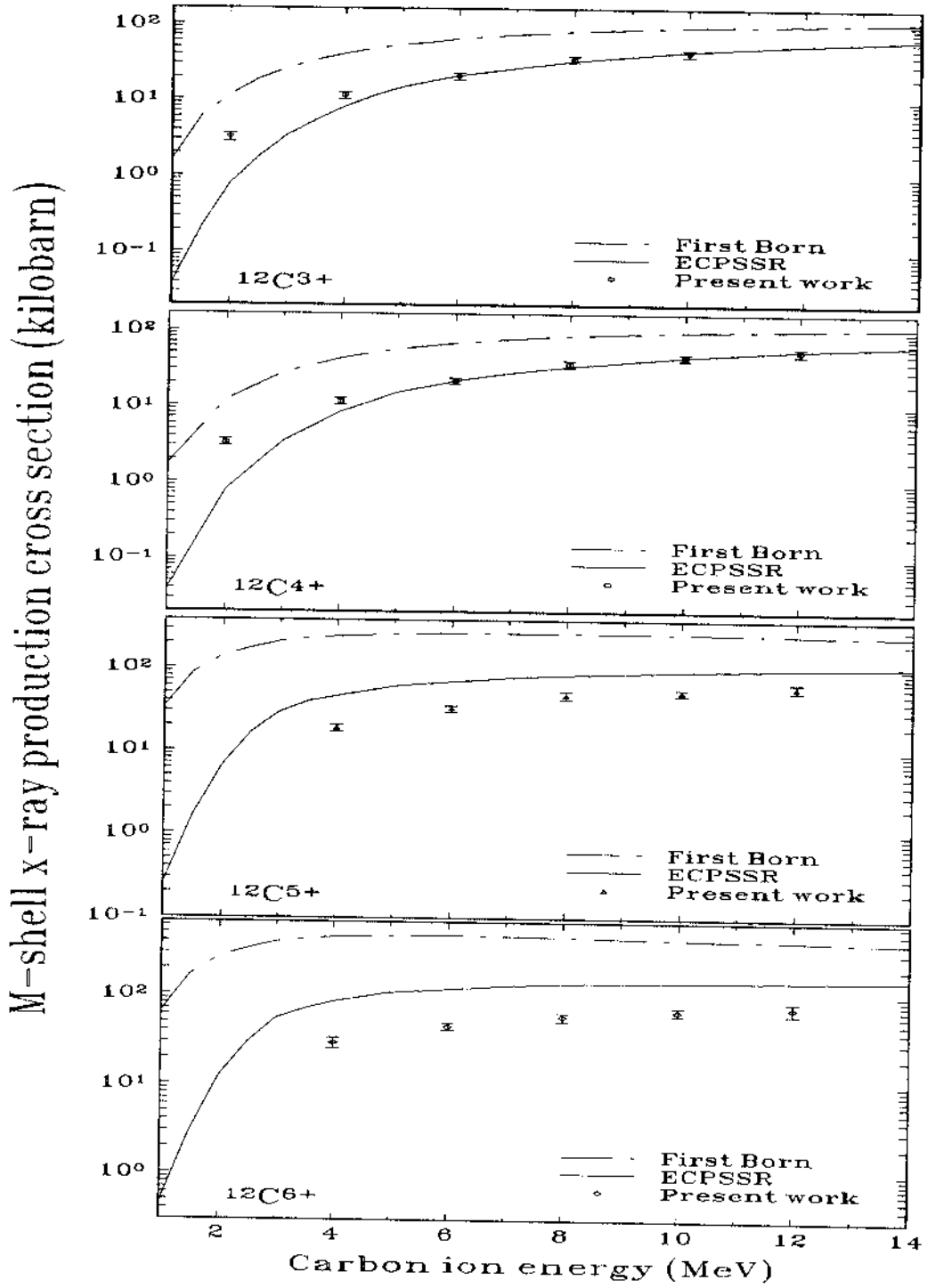

Figure 5.3 M-shell x-ray production in $_{67}$Ho by carbon ions in charge state 3+, 4+, 5+, and 6+ with theoretical calculations of the first Born approximation (dashed-dot curve) and the ECPSSR theory (solid curve).

Table 5.2 Contribution of electron capture to M-shell x-ray production cross sections (in kilobarn) in Ho by carbon ions with K vacancies (q=5+ and 6+) at energies, E_1=4–12 MeV. The experimental M-shell x-ray production cross sections due to electron capture, σ_{MX}^{EC}, were calculated from the difference of Ho total M-shell x-ray cross sections for carbon ions with and without K vacancies. $\sigma_{MX}^{EC\text{-}ECPSSR}$ and $\sigma_{MX}^{EC\text{-}FB}$ are the theoretical contributions of electron capture from the ECPSSR theory and the first Born approximation, respectively.

E_1	q	$\sigma_{MX}^{EC}(q)=\sigma_{MX}(q)-\sigma_{MX}(4+)$	$\sigma_{MX}^{EC}(q)/\sigma_{MX}^{EC\text{-}FB}(q)$	$\sigma_{MX}^{EC}(q)/\sigma_{MX}^{EC\text{-}ECPSSR}(q)$
4	5+	6.9±2.1	0.030	0.17
4	6+	17.7±4.6	0.041	0.22
6	5+	10.9±3.6	0.045	0.19
6	6+	23.3±4.4	0.053	0.22
8	5+	11.0±6.6	0.048	0.18
8	6+	22.0±7.2	0.053	0.20
10	5+	6.9±6.9	0.032	0.11
10	6+	21.2±8.2	0.056	0.19
12	5+	5.5±9.36	0.028	0.10
12	6+	19.3±12.1	0.055	0.19

E_1	q	$\sigma_{MX}^{EC}(q)=\sigma_{MX}(q)-\sigma_{MX}(3+)$	$\sigma_{MX}^{EC}(q)/\sigma_{MX}^{EC\text{-}FB}(q)$	$\sigma_{MX}^{EC}(q)/\sigma_{MX}^{EC\text{-}ECPSSR}(q)$
4	5+	7.0±2.1	0.030	0.17
4	6+	17.8±4.6	0.041	0.23
6	5+	11.6±3.5	0.048	0.21
6	6+	24.0±4.3	0.055	0.23
8	5+	12.2±6.4	0.053	0.20
8	6+	23.2±7.0	0.056	0.21
10	5+	9.6±6.7	0.044	0.17
10	6+	23.9±8.0	0.063	0.22

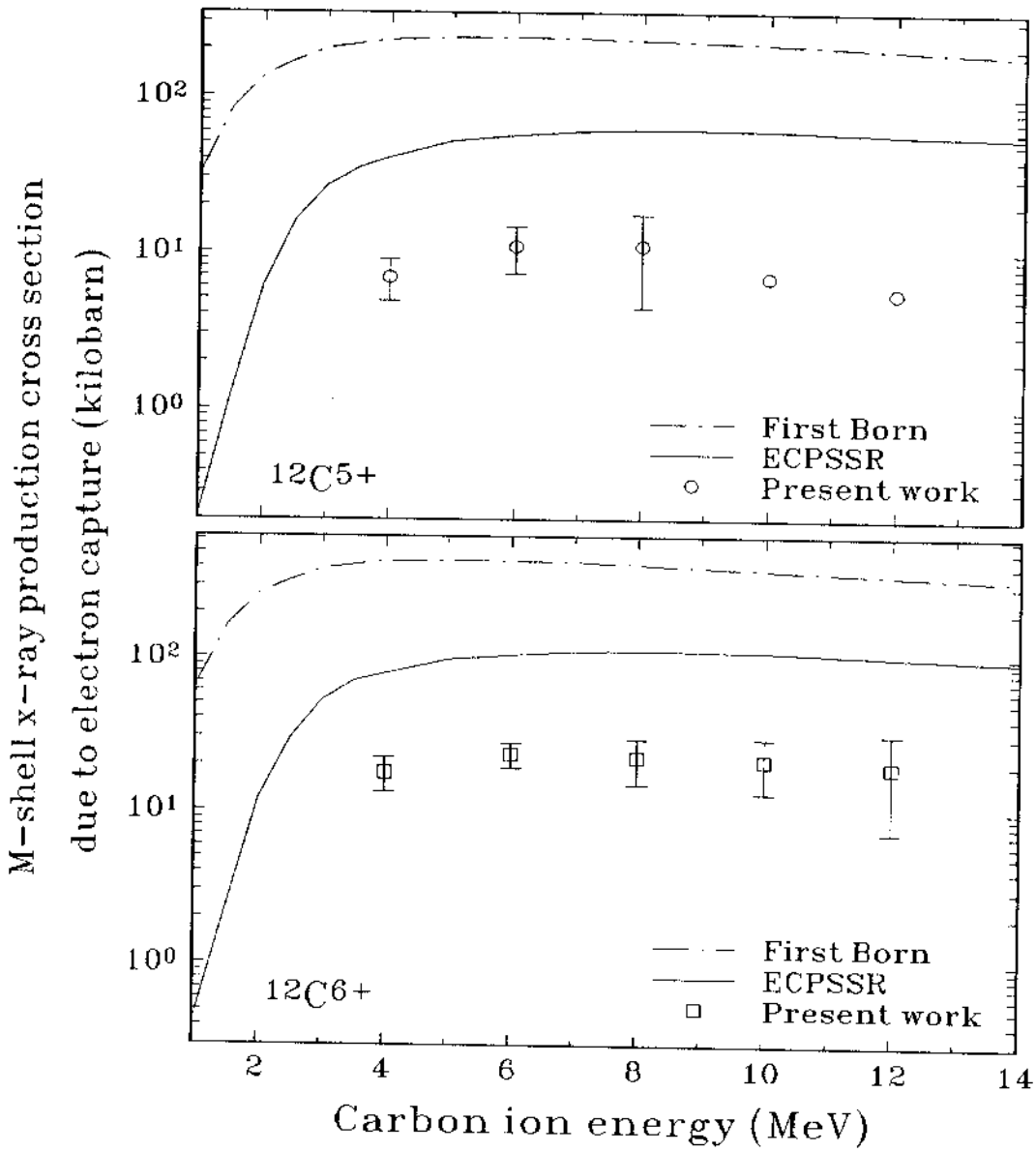

Figure 5.4 M-shell x-ray production due to electron capture to the ion as a function of incident carbon ion energy from 4 to 12 MeV for H-like and fully-stripped carbon ions. The first Born approximation (dashed-dot curve) and the ECPSSR theory (solid curve) for the electron capture overestimate the data.

results with q=3+ subtracted from the data (see table 5.2) because the experimental cross sections of q=4+ might be slightly higher than that of q=3+, when He-like carbon ion is in a metastable state with one electron in the Is state and another one in the 2s state. This metastable state condition of a helium-like carbon ion (q=4+) may contribute a small enhancement to the x-ray production cross section due to electron capture. Also shown in figure 5.4 are the theoretical predictions of the first Born and ECPSSR theories. The ECPSSR theory is seen to overpredict the measurements by a factor of 4-10 while the first Born calculations are at least a factor of 16 higher than the experimental results.

Table 5.3 shows a tabulation of all the measured M-shell x-ray production cross sections for direct ionization of q=3+ and 4+ and the corresponding ECPSSR and first Born theories. Table 5.1 shows that the data of q= 3+ and 4+ are close to the data of q=2+ and 3+ (at 2 and 4 MeV) and much lower than the data of q=5+ and 6+ (at 4 to 12 MeV). It is shown that DI gives most of the contribution to q=2+ to 4+ data that include both DI and EC to the L-, M-,... shells. Thus, the q=2+ to 4+ data of the M-shell x-ray production cross sections can be used for comparison with the theories for direct ionization. Figure 5.5 shows the experimental data and the first Born and ECPSSR theoretical calculation curves of the direct ionization contribution to the M-shell x-ray production cross sections. As seen in the figure, the first Born theory overestimates the data by a small factor at low energies while it gives agreement at high energies. The ECPSSR theory underestimates all the data about by 20-76%.

For the direct ionization, the first Born theory overestimates the data by a factor of from 6% to 40%. The first Born approximation was originally calculated

Table 5.3 Contribution of direct ionization to M-shell x-ray production cross sections (in kilobarn) in Ho by carbon ions without K vacancies (q=3+ and 4+) at energies, E_1=2–12 MeV. The experimental M-shell x-ray production cross sections due to direct ionization, σ_{MX}^{DI}, were measured for the Ho total M-shell x-ray cross sections for the carbon ions without K vacancy (q=3+ and 4+), which were assumed without electron capture contribution. $\sigma_{MX}^{DI\text{-}ECPSSR}$ and $\sigma_{MX}^{DI\text{-}PB}$ are the theoretical contributions of direct ionization from the ECPSSR theory and the first Born approximation, respectively.

E_1	q	$\sigma_{MX}^{DI}(q)$	$\sigma_{MX}^{DI}(q)/\sigma_{MX}^{DI\text{-}FB}(q)$	$\sigma_{MX}^{DI}(q)/\sigma_{MX}^{DI\text{-}ECPSSR}(q)$
2	2+	3.10±0.03	0.60	5.00
2	3+	3.20±0.04	0.62	5.16
2	4+	3.36±0.08	0.65	5.42
4	2+	11.0±1.3	0.72	1.99
4	3+	11.6±1.6	0.75	2.09
4	4+	11.7±1.7	0.76	2.11
6	3+	21.0±2.8	0.79	1.57
6	4+	21.7±2.9	0.82	1.62
8	3+	35.4±3.5	0.93	1.54
8	4+	36.6±3.8	0.96	1.60
10	3+	43.1±4.2	0.88	1.30
10	4+	45.8±4.5	0.94	1.38
12	4+	55.2±6.1	0.94	1.27

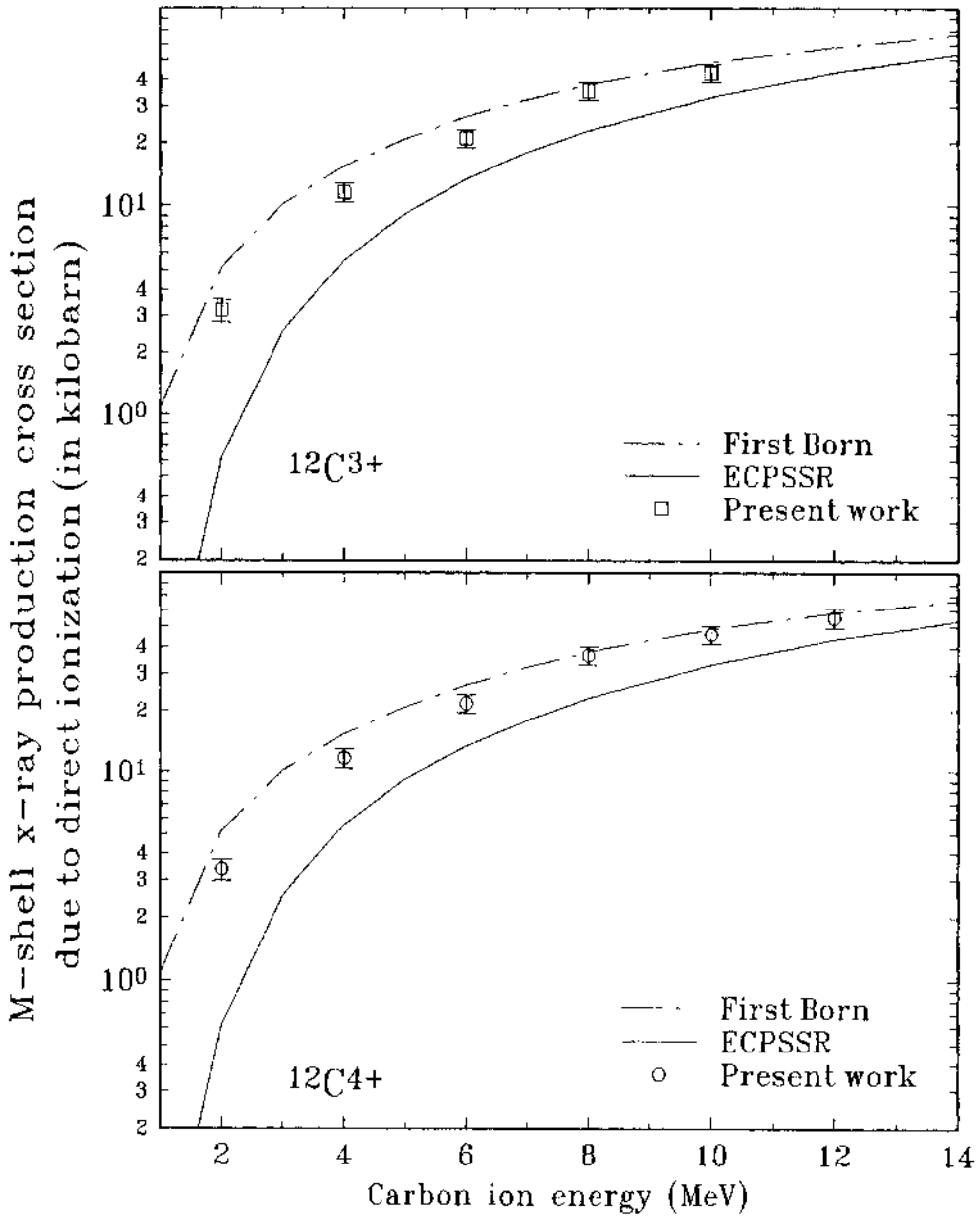

Figure 5.5 M-shell x-ray production due to direct ionization and a small contribution of EC to L-,M-, ... shells as a function of the incident carbon ion energy for 2 to 12 MeV. The data for the q=3+ and 4+ (without K-vacancy) are assumed to give much less electron capture contribution compared to the data for q=5+ and 6+. The first Born approximation (dashed-dot curve) overestimates the data and the ECPSSR theory (solid curve) underestimates the data.

for high velocity ion-atom collisions. At an impact range $0.17 \leq v_i/v_{2M} < 0.42$, the carbon ion velocity is less than the M-shell electron velocity, hence it is reasonable for the first Born theory to give an overestimation in this velocity range. However, the ECPSSR theory seems to underestimate all the data. As mentioned in chapter 2, the ECPSSR theory includes several modifications, particularly in the low ion velocity region, which reduce the cross sections from the first Born theory. The lower value predicted by the ECPSSR theory may be accounted for by its overcorrection of the M-shell ionization cross section of electron correlation effects which are not accounted for in the theory.

In figure 5.4 for the electron capture, however, the ECPSSR theory overestimates all the data at least a factor of five although the modifications were considered for low ion velocities. The first Born theory predictions overestimate the data by at least a factor of twenty-two.

In figure 5.3, the ECPSSR theory shows fortuitously good agreement to the sum of direct ionization and electron capture obtained from the total M-shell x-ray production cross sections for q=3+ and 4+ at energies 6 to 12 MeV because the overestimation of EC makes up for the underestimation of DI. The ECPSSR theory still underestimates the data at 2 and 4 MeV. This may be caused by: (1) the correction factors reduces the cross section too much in this low energy region, (2) some multiple ionization at slow heavy ion bombardment [4], or (3) quasi-molecular orbit effects exist at this region, $Z_1/Z_2=0.09$ and $0.17 \leq v_i/v_{2e} < 0.42$. Similarly to the EC cross sections, the ECPSSR theory overpredicts all the q=5+ and 6+ data for the total M-shell x-ray cross sections.

For the first Born theory, the OBKN approximation overpredicts all the data for the EC cross sections for this thesis as well as elsewhere [39-43, 55-58]

and the PWBA theory overpredicts most of the data for the DI cross sections at low impact velocity. The ECPSSR theory shows good agreement to the DI cross sections of K- and L-shell for light ions that do not have a comparable amount of EC [31-33 37, 38] and gives good agreement to the EC cross sections for the K- and L-shell [39, 40, 43], but overpredicts the K-shell measurement of McDaniel *et al* [42]. For M-shell measurements, the ECPSSR theory overpredicts the EC cross section measurements of Andrew *et al.* [43, 55] and has no consistency in the measurement of Mehta *et al.* [56-58], but gives agreement to the total M-shell x-ray production that contains the DI+EC cross sections for all the measurements.

The M-shell ionization measurements are more complicated than the K- and L-shell measurements for several reasons. For example, the fluorescence yield may not be well known and is affected by multiple ionization, which depends on the type of projectile ion and energy as mentioned in chapter 4. The experimental difficulty, such as producing high charge state ions, measuring low energy M-shell x rays, and making thin and contaminant-free targets, may give higher uncertainties for the results. The electron correlation effects for different charge state ions were not considered. The M-shell x-ray isotropy was not measured although both DI and EC may cause the alignment for M-shell ionization. Actually, there are too few M-shell measurements, particularly for electron capture, for a complete comparison with the ECPSSR theory. It is hard to judge whether the ECPSSR theory can give good predictions to the direct ionization and electron capture cross sections for heavy ion collision over a large energy range.

CHAPTER 6

CONCLUSION

The effective cross sections of target Ho M-shell x-ray production for various charge states as a function of target thicknesses were measured. It is clear from these studies that single collision conditions exist for target thickness less than 2 $\mu g/cm^2$. To be certain of single collision conditions, all of the cross section measurements for charge state dependence of the M-shell x-ray production reported in this study were done with a $_{67}$Ho target that was 0.34 $\mu g/cm^2$ thick, which is approximately 1–2 atomic layers. The data were found to be reproducible for these thin targets, which implies that the targets were fairly uniform in thickness. The x-ray production cross section was then measured in this single collision regime for $^{12}C^q$ (q=2+ to 6+) ions from 2 to 12 MeV (see fig. 5.2). It was not possible to reach charge states 5+ and 6+ for the 2 MeV data since the stripping cross sections are simply too low. The cross sections for q=2+ to 4+ (no K vacancy) are seen to be significantly lower than those for q=5+ and 6+, indicating in the latter cases contributions to the inner-shell ionization from electron capture into the K-shell of ^{12}C.

The numerical value of the measured electron capture cross section was determined by subtracting the q=3+ or 4+ data from the q= 5+ and q= 6+ data for vanishingly thin targets. The electron capture cross sections were then compared to the theoretical calculations of the first Born and ECPSSR theories

(see fig. 5.4). The ECPSSR theory seems to be on average about a factor of 4-10 higher than the experimental results while the first Born theory gave results that were at least about a factor of 16 higher than the measured results.

The direct ionization cross sections was determined from the M-shell x-ray production cross section for q=3+ and 4+. The first Born theory overpredicts the data by a small factor at 2 to 6 MeV and gives agreement to the data at 8 to 12 MeV while the ECPSSR theory underestimates the data by about 20-76%.

For the total M-shell x-ray production cross sections, the ECPSSR theory gives a good fit to the experimental data for average charge states near the equilibrium value (see fig. 5.3) at 6 to 12 MeV due to compensation of overestimation of EC to underestimation of DI. It still underestimates the data at 2 and 4 MeV. In the low energy region, the molecular orbit (MO) effect and multiple ionization may become important and should contribute to higher ionization cross section. The first Born theory, however, overpredicts the experimental data by about a factor of 5 over most of the energy range.

In this thesis, it has been shown that electron capture (EC) is a major contributor to the M-shell ionization in addition to direct Coulomb ionization (DI). Here, the theories give a close prediction to the DI cross sections, but do not give an accurate prediction to EC for the region $Z_1/Z_2=0.09$ and $0.17 \leq v_i/v_{2e} < 0.42$. Inner-shell ionization is a very complicated process which is related to several mechanisms and varies for different collision systems. Further study for M-shell ionization by heavy ions is required for those unknown terms which include the MO effect at low energy, the electron correlation contribution to both DI and EC, the multiple ionization and all the parameters related to fluorescence yields, and the M-shell x-ray isotropy.

APPENDIX

M-shell ionization cross sections (DI+EC) and x-ray production cross sections (X-RAY) of the first Born approximation and the ECPSSR theory.

Z1=6 Z2=67 A1=12 A2=164.9 q=6

Fluorescence yields (ω): .00108 .00185 .00145 .0067 .0106

S12	S13	S23	S14	S24	S34	S15	S25	S35	S45
.266	.527	.106	.061	.667	.145	9.000001E-02	.12	.751	.408

M-SHELL IONIZATION CROSS SECTIONS AND
X-RAY PRODUCTION CROSS SECTIONS (barn)

	The First Born Approximation				The ECPSSR Theory				
E_1	DI	EC	DI+EC	X-RAY	DI	EC	DI+EC	X-RAY	ω
1.00+0	9.99+4	5.97+6	6.07+6	6.52+4	2.93+3	3.95+4	4.24+4	4.64+2	1.09-2
2.00+0	4.76+5	2.44+7	2.48+7	2.67+5	5.72+4	1.09+6	1.15+6	1.24+4	1.08-2
3.00+0	9.30+5	3.57+7	3.66+7	3.94+5	2.33+5	4.83+6	5.06+6	5.44+4	1.08-2
4.00+0	1.41+6	4.00+7	4.14+7	4.47+5	5.08+5	7.30+6	7.80+6	5.41+4	1.08-2
5.00+0	1.91+6	4.07+7	4.26+7	4.61+5	8.43+5	9.02+6	9.87+6	1.87+5	1.08-2
6.00+0	2.43+6	4.05+7	4.29+7	4.65+5	1.23+6	9.67+6	1.09+7	1.18+5	1.08-2
7.00+0	2.96+6	3.93+7	4.23+7	4.60+5	1.65+6	1.02+6	1.18+7	1.28+5	1.08-2
8.00+0	3.48+6	3.80+7	4.15+7	4.52+5	2.10+6	1.03+7	1.24+7	1.35+5	1.09-2
1.00+1	4.47+6	3.50+7	3.95+7	4.31+5	3.04+6	1.01+7	1.31+7	1.43+5	1.09-2
1.20+1	5.36+6	3.22+7	3.76+7	4.12+5	3.99+6	9.39+6	1.34+7	1.46+5	1.09-2
1.40+1	6.15+6	2.96+7	3.58+7	3.93+5	4.88+6	8.83+6	1.37+7	1.50+5	1.09-2
1.60+1	6.84+6	2.75+7	3.43+7	3.77+5	5.68+6	7.71+6	1.34+7	1.46+5	1.09-2
1.80+1	7.41+6	2.57+7	3.31+7	3.64+5	6.40+6	7.33+6	1.37+7	1.50+5	1.09-2
2.00+1	7.88+6	2.41+7	3.19+7	3.52+5	7.01+6	6.77+6	1.38+7	1.51+5	1.09-2

Z1=1 Z2=67 A1=12 A2=164.9 q= 5

Fluorescence yields (ω): .00108 .00185 .00145 .0067 .0106

S12	S13	S23	S14	S24	S34	S15	S25	S35	S45
.266	.527	.106	.061	.667	.145	9.000001E-0	2 .12	.751	.408

M-SHELL IONIZATION CROSS SECTIONS AND
X-RAY PRODUCTION CROSS SECTIONS (barn)

	The First Born Approximation				The ECPSSR Theory				
E_1	DI	EC	DI+EC	X-RAY	DI	EC	DI+EC	X-RAY	ω
1.00+0	9.99+4	3.01+6	3.11+6	3.35+4	2.93+3	2.01+4	2.30+4	2.51+2	1.09-2
2.00+0	4.76+5	1.25+7	1.30+7	1.40+5	5.72+4	5.55+5	6.12+5	6.60+3	1.08-2
3.00+0	9.30+5	1.86+7	1.96+7	2.11+5	2.33+5	2.46+6	2.69+6	2.89+4	1.08-2
4.00+0	1.41+6	2.13+7	2.27+7	2.45+5	5.08+5	3.78+6	4.29+6	4.62+4	1.08-2
5.00+0	1.91+6	2.20+7	2.40+7	2.59+5	8.43+5	4.80+6	5.65+6	6.10+4	1.08-2
6.00+0	2.43+6	2.22+7	2.46+7	2.67+5	1.23+6	5.22+6	6.45+6	6.98+4	1.08-2
7.00+0	2.96+6	2.18+7	2.48+7	2.69+5	1.65+6	5.55+6	7.20+6	7.81+4	1.08-2
8.00+0	3.48+6	2.12+7	2.47+7	2.69+5	2.10+6	5.68+6	7.78+6	8.45+4	1.09-2
1.00+1	4.47+6	1.98+7	2.42+7	2.65+5	3.04+6	5.64+6	8.68+6	9.47+4	1.09-2
1.20+1	5.36+6	1.83+7	2.37+7	2.59+5	3.99+6	5.31+6	9.30+6	1.02+5	1.09-2
1.40+1	6.15+6	1.69+7	2.31+7	2.53+5	4.88+6	5.03+6	9.90+6	1.08+5	1.09-2
1.60+1	6.84+6	1.58+7	2.26+7	2.48+5	5.68+6	4.46+6	1.01+7	1.11+5	1.09-2
1.80+1	7.41+6	1.47+7	2.21+7	2.43+5	6.40+6	4.22+6	1.06+7	1.16+5	1.09-2
2.00+1	7.88+6	1.38+7	2.17+7	2.39+5	7.01+6	3.91+6	1.09+7	1.19+5	1.09-2

Z1=6 Z2=67 A1=12 A2=164.9 q=4

Fluorescence yields (ω): .00108 .00185 .00145 .0067 .0106

S12	S13	S23	S14	S24	S34	S15	S25	S35	S45
.266	.527	.106	.061	.667	.145	9.000001E-02	.12	.751	.408

M-SHELL IONIZATION CROSS SECTIONS AND
X-RAY PRODUCTION CROSS SECTIONS (barn)

	The First Born Approximation				The ECPSSR Theory				
E_1	DI	EC	DI+EC	X-RAY	DI	EC	DI+EC	X_RAY	ω
1.00+0	9.99+4	5.98+4	1.60+5	1.73+3	2.93+3	6.17+2	3.54+3	3.90+1	1.10-2
2.00+0	4.76+5	6.35+5	1.11+6	1.20+4	5.72+4	1.58+4	7.30+4	7.93+2	1.09-2
3.00+0	9.30+5	1.61+6	2.54+6	2.74+4	2.33+5	8.89+4	3.22+5	3.49+3	1.08-2
4.00+0	1.41+6	2.59+6	3.99+6	4.31+4	5.08+5	2.61+5	7.69+5	8.31+3	1.08-2
5.00+0	1.91+6	3.38+6	5.29+6	5.72+4	8.43+5	5.82+5	1.42+6	1.54+4	1.08-2
6.00+0	2.43+6	3.94+6	6.36+6	6.89+4	1.23+6	7.79+5	2.00+6	2.17+4	1.08-2
7.00+0	2.96+6	4.26+6	7.22+6	7.82+4	1.65+6	9.20+5	2.57+6	2.78+4	1.08-2
8.00+0	3.48+6	4.45+6	7.92+6	8.60+4	2.10+6	1.06+6	3.16+6	3.43+4	1.08-2
1.00+1	4.47+6	4.53+6	9.00+6	9.79+4	3.04+6	1.19+6	4.24+6	4.61+4	1.09-2
1.20+1	5.36+6	4.39+6	9.76+6	1.06+5	3.99+6	1.23+6	5.22+6	5.68+4	1.09-2
1.40+1	6.15+6	4.22+6	1.04+7	1.13+5	4.88+6	1.22+6	6.10+6	6.64+4	1.09-2
1.60+1	6.84+6	4.00+6	1.08+7	1.18+5	5.68+6	1.20+6	6.88+6	7.51+4	1.09-2
1.80+1	7.41+6	3.79+6	1.12+7	1.22+5	6.40+6	1.11+6	7.52+6	8.20+4	1.09-2
2.00+1	7.88+6	3.61+6	1.15+7	1.26+5	7.01+6	1.05+6	8.07+6	8.80+4	1.09-2

Z1=6 Z2=67 A1=12 A2=164.9 q=3

Fluorescence yields (ω): .00108 .00185 .00145 .0067 .0106

S12	S13	S23	S14	S24	S34	S15	S25	S35	S45
.266	.527	.106	.061	.667	.145	9.000001E-02	.12	.751	.408

M-SHELL IONIZATION CROSS SECTIONS AND
X-RAY PRODUCTION CROSS SECTIONS (barn)

	The First Born Approximation				The ECPSSR Theory				
E_1	DI	EC	DI+EC	X_RAY	DI	EC	DI+EC	X_RAY	ω
1.00+0	9.99+4	5.43+4	1.54+5	1.67+3	2.93+3	5.62+2	3.49+3	3.84+1	1.10-2
2.00+0	4.76+5	5.80+5	1.06+6	1.14+4	5.72+4	1.44+4	7.16+4	7.78+2	1.09-2
3.00+0	9.30+5	1.47+6	2.40+6	2.59+4	2.33+5	8.18+4	3.14+5	3.40+3	1.08-2
4.00+0	1.41+6	2.37+6	3.78+6	4.07+4	5.08+5	2.38+5	7.46+5	8.07+3	1.08-2
5.00+0	1.91+6	3.10+6	5.01+6	5.41+4	8.43+5	5.34+5	1.38+6	1.49+4	1.08-2
6.00+0	2.43+6	3.61+6	6.04+6	6.54+4	1.23+6	7.14+5	1.94+6	2.10+4	1.08-2
7.00+0	2.96+6	3.92+6	6.87+6	7.45+4	1.65+6	8.45+5	2.49+6	2.70+4	1.08-2
8.00+0	3.48+6	4.09+6	7.56+6	8.21+4	2.10+6	9.75+5	3.07+6	3.33+4	1.08-2
1.00+1	4.47+6	4.16+6	8.64+6	9.40+4	3.04+6	1.10+6	4.14+6	4.50+4	1.09-2
1.20+1	5.36+6	4.04+6	9.41+6	1.03+5	3.99+6	1.13+6	5.12+6	5.58+4	1.09-2
1.40+1	6.15+6	3.88+6	1.00+7	1.10+5	4.88+6	1.12+6	6.00+6	6.54+4	1.09-2
1.60+1	6.84+6	3.68+6	1.05+7	1.15+5	5.68+6	1.11+6	6.79+6	7.40+4	1.09-2
1.80+1	7.41+6	3.49+6	1.09+7	1.19+5	6.40+6	1.03+6	7.43+6	8.10+4	1.09-2
2.00+1	7.88+6	3.32+6	1.12+7	1.23+5	7.01+6	9.70+5	7.98+6	8.70+4	1.09-2

Z1=6 Z2=67 A1=12 A2=164.9 q=2

Fluorescence yields (ω): .00108 .00185 .00145 .0067 .0106

S12	S13	S23	S14	S24	S34	S15	S25	S35	S45
.266	.527	.106	.061	.667	.145	9.000001E-02	.12	.751	.408

M-SHELL IONIZATION CROSS SECTIONS AND
X-RAY PRODUCTION CROSS SECTIONS (barn)

	The First Born Approximation				The ECPSSR Theory				
E_1	DI	EC	DI+EC	X_RAY	DI	EC	DI+EC	X-RAY	ω
1.00+0	9.99+4	4.89+4	1.49+5	1.61+3	2.93+3	5.08+2	3.43+3	3.78+1	1.10-2
2.00+0	4.76+5	5.25+5	1.00+6	1.08+4	5.72+4	1.30+4	7.02+4	7.62+2	1.09-2
3.00+0	9.30+5	1.33+6	2.26+6	2.44+4	2.33+5	7.38+4	3.06+5	3.32+3	1.08-2
4.00+0	1.41+6	2.15+6	3.56+6	3.84+4	5.08+5	2.16+5	7.24+5	7.82+3	1.08-2
5.00+0	1.91+6	2.82+6	4.73+6	5.11+4	8.43+5	4.86+5	1.33+6	1.44+4	1.08-2
6.00+0	2.43+6	3.29+6	5.71+6	6.18+4	1.23+6	6.50+5	1.88+6	2.03+4	1.08-2
7.00+0	2.96+6	3.57+6	6.52+6	7.07+4	1.65+6	7.70+5	2.42+6	2.62+4	1.08-2
8.00+0	3.48+6	3.72+6	7.20+6	7.82+4	2.10+6	8.88+5	2.98+6	3.24+4	1.09-2
1.00+1	4.47+6	3.80+6	8.27+6	9.00+4	3.04+6	1.00+6	4.05+6	4.40+4	1.09-2
1.20+1	5.36+6	3.69+6	9.05+6	9.87+4	3.99+6	1.03+6	5.02+6	5.47+4	1.09-2
1.40+1	6.15+6	3.55+6	9.70+6	1.06+5	4.88+6	1.03+6	5.90+6	6.43+4	1.09-2
1.60+1	6.84+6	3.36+6	1.02+7	1.11+5	5.68+6	1.01+6	6.69+6	7.30+4	1.09-2
1.80+1	7.41+6	3.19+6	1.06+7	1.16+5	6.40+6	9.38+5	7.34+6	8.01+4	1.09-2
2.00+1	7.88+6	3.04+6	1.09+7	1.19+5	7.01+6	8.85+5	7.90+6	8.61+4	1.09-2

BIBLIOGRAPHY

1. T. Mukoyama, International Journal of PIXE, Vol. 1, No. 3, 209 (1991).

2 W. Jitschin in *Coherence in Atomic Collision Physics* edited by H.J. Beyer, K. Bhem, and R. Hippler, (Plenum Press, New York, 1988), p. 171.

3. E.J. McGuire, Phys. Rev. A **5**, 1043 (1972).

4. G. Lapicki, R. Mehta, J.L. Duggan, P.M. Kocur, J.L. Price, and F.D. McDaniel, Phys. Rev. A **34**, 3813 (1986).

5. E. Merzbzcher and H. Lewis, Handbuch der Physik, ed. S. Flugge, vol. **34** (Springer, Berlin, 1958) p. 166.

6. D.H. Madison and E. Merzbacher in *Atomic Inner-Shell Process*, edited by B. Crasemann (Academic Press, New York, 1975), Vol. I, pp. 1-72.

7. G. Lapicki and W. Losonsky, Phys. Rev. A **15**, 896 (1977); *ibid.* **20**, 481 (1979).

8. G. Lapicki and F.D. McDaniel, Phys. Rev. A **22**, 1896 (1980); *ibid.* **23**, 975 (E) (1981).

9. U. Fano and W. Lichten, Phys. Rev. Lett. **14**, 627 (1965).

10. W. Lichten, Phys. Rev. **164**, 131 (1967).

11. M. Barat and W. Lichten, Phys. Rev. A **6**, 211 (1972).

12. W. Meyerhof, Phys. Rev. A **18**, 414 (1978); *ibid.* **20**, 2235 (1979).

13. R. Anholt, Rev. Mod. Phys. **57**, 995 (1985).

14. G. Lapicki and W. Lichten, Phys. Rev. A **31**, 1354 (1985).

15. J.D. Garcia, E. Gerjuoy, and J.W. Welker, Phys. Rev. **165**, 68 (1968).

16. J.D. Garcia, Phys. Rev. A **1**, 280 (1970). *ibid.* A 1, 1402 (1970).

17. J.D. Garcia, Phys. Rev. A **4**, 955 (1971).

18. J. Bang and J.M. Hansteen, Mat.-Fys. Medd. Danske Vidensk. Selsk. **31**, No. 13, 1 (1959).

19. H. Bethe, Ann. Phys., (Leizig), **5**, 325 (1930).

20. N. Bohr, Phil. Mag. **25**, 10 (1913).

21. N. Bohr, Phil. Mag. **30**, 581 (1915).

22 J.M. Hansteen, O.M. Johnson, and L. Kocbach, At. Data. Tables **15**, 305 (1975).

23. W. Brandt and G. Lapicki, Phys. Rev. A **20**, 465 (1979); *ibid.* A **23**, 1717 (1981).

24. G. Basbas, W. Brandt, R. Laubert, and A. Schwarzschild, Phys. Rev. Lett. **27**, 171 (1971).

25. G. Basbas, W. Brandt, and R. Laubert, Phys. Rev. Lett. **34A**, 277 (1971).

26. G. Basbas, W. Brandt and R. Laubert, Phys. Rev. A **7**, 983 (1973).

27. G. Basbas, W. Brandt and R. Laubert, Phys. Rev. A 17, 1655 (1978).

28. G. Lapicki and A.R. Zander, Phys. Rev. A **23**, 2072 (1981).

29. G. Basbas, W. Brandt and R.H. Ritchie, Phys. Rev. A **7**, 1971 (1973).

30. D.E. Johnson, G. Basbas, and F.D. McDaniel, At. Data Nucl. Data Tables **24**, 1(1979).

31. G. Lapicki, Phys. Chem. Ref. Data **18**, 111 (1989).

32. Y.C. Yu, M.R. McNeir, D.L. Weathers, D.K. Marble, J.L. Duggan, F.D. McDaniel, and G. Lapicki, Nucl. Instrum. Methods B**56/57**, 1188 (991).

33. Y.C. Yu, M.R. McNeir, D.L. Weathers, J.L. Duggan, F.D. McDaniel, and G. Lapicki, Phys. Rev. A **44**, 5702 (1991).

34. J.R. Oppenheimer, Phys. Rev. **31**, 349 (1928).

35. H.C. Brinkman and H.A. Kramers, *Proc. Acad. Sci.* (Amsterdam) **33**, 973 (1930).

36. V. S. Nikolaev, Zh. Eksp. Teor.Fiz. **51**, 1263 (1966) [Sov. Phys. JETP **24**, 847 (1967)].

37. M.R. McNeir, Y.C. Yu, D.L. Weathers, D.K. Marble, J.L. Duggan, F.D. McDaniel, and G. Lapicki, Nucl. Instrum. and Methods B**56/57**, 26 (1991).

38. M.R. McNeir, Y.C. Yu, D.L. Weathers, J.L. Duggan, F.D. McDaniel, and G. Lapicki, Phys. Rev. A **44**, 4372 (1991).

39. F.D. McDaniel, J.L. Duggan, G. Basbas, P.D. Miller, and G. Lapicki, Phys. Rev. A **16**, 1375 (1977).

40. F.D. McDaniel, A. Toten, R.S. Peterson, J.L. Duggan, S.R. Wilson, J.D. Gressett, P.D. Miller, and G. Lapicki, Phys. Rev. A **19**, 1517 (1979).

41. F.D. McDaniel, J.L. Duggan, G. Lapicki, and P.D. Miller, Nucl. Instrum. Methods **B42**, 485 (1989).

42. F.D. McDaniel, D.K. Marble, J.L. Duggan, M.R. McNeir, Y.C. Yu, Z.Y. Zhao, D.L. Weathers, R.M. Wheeler, R.P. Chaturvedi, and G. Lapicki, Nucl. Instrum. Methods **B53**, 531 (1991).

43. M.C. Andrews, F.D. McDaniel, J.L. Duggan, P.D. Miller, P.L. Pepmiller, H.F. Krause, T.M. Rosseel, L.A. Rayburn, R. Mehta, and G. Lapicki, Phys. Rev. A **36**, 3699 (1987).

44. J.R. Macdonald, L. Winters, M.D. Brown, T. Chiao, and L.D. Ellsworth, Phys. Rev. Lett. **29**, 1291 (1972).

45. J.R. Macdonald, L. Winters, M.D. Brown, L.D. Ellsworth, T. Chiao, and E.W. Pettus, Phys. Rev. Lett. **30**, 251 (1973).

46. A.M. Halpern and J. Law, Phys. Rev. Lett. **31**, 4 (1973); *ibid.* **31**, 620E (1973).

47. R.L. Kauffman, F. Hopkins, C.W. Woods, and P. Richard, Phys. Rev. Lett. **31**, 621 (1973).

48. J.R. Macdonald, C.L. Cocke, and W.W. Edison, Phys. Rev. Lett. **32**, 648 (1974).

49. J.R. Mowat, I.A. Sellin, P.M. Griffin, D.J. Pegg, and R.S. Peterson, Phys. Rev. A **9**, 644 (1974).

50. S.J. Czuchlewski, J.R. Macdonald, and L.D. Ellsworth, Phys. Rev. A **11**, 1108 (1975).

51. J.R. Macdonald, M.D. Brown, S.J. Czuchlewski, L.M. Winters, R. Laubert, I.A. Sellin, and J.R. Mowat, Phys. Rev. A **14**, 1997 (1976).

52. J.A. Guffey, L.D. Ellsworth, and J.R. Macdonald, Phys. Rev. A **15**, 1863 (1977).

53. U. Schiebel, T.J. Gray, R.K. Gardner, and P. Richard, J. Phys. B **10**, 2189 (1977).

54. B. Doyle, U. Schiebel, J.R. Macdonald, L.D. Ellsworth, Phys. Rew. A **17**, 523 (1978).

55. M.C. Andrews, F.D. McDaniel, J.L. Duggan, P.D. Miller, P.L. Pepmiller, H.F. Krause, T.M. Rosseel, L.A. Rayburn, R. Mehta, and G. Lapicki, Nucl. Instrum. Methods **B10/11**, 186 (1985).

56. R. Mehta, J.L. Duggan, F.D. McDaniel, M.C. Andrews, R.M. Wheeler, R.P. Chaturvedi, P.D. Miller, and G. Lapicki, IEEE Trans. Nucl. Sci. **NS-28**, No. 2, 1 (1981).

57. R. Mehta, J.L. Duggan, F.D. McDaniel, M.C. Andrews, G. Lapicki, P.D. Miller, L.A. Rayburn, and A.R. Zander, IEEE Trans. Nucl. Sci. **NS-30**, 906 (1983).

58. R. Mehta, J.L. Duggan, F.D. McDaniel, M.C. Andrews, G. Lapicki, P.D. Miller, L.A. Rayburn, and A.R. Zander, Phys. Rev. A **28**, 2722 (1983).

59. F. Hopkins, Phys. REv. Lett **35**, 270 (1975).

60. T.J. Gray, P. Richard, R.K. Gardner, K.A. Jamison and J.M. Hall, Phys. Rev. A **14**, 1333 (1976).

61. R.K. Gardner, T.J. Gray, P. Richard, C. Schmiedekamp, K.A. Jamison, and J.M. Hall, Phys. Rev. A **15**, 2202 (1977).

62. H. Tawara, P. Richard, T.J. Gray, J. Newcomb, K.A. Jamison, C. Schmiedekamp, and J.M. Hall, Phys. Rev. A **18**, 1373 (1978).

63. C. Schmiedekamp, T.J. Gray, B.L. Doyle, and U. Schiebel, Phys. Rev. A **19**, 2167 (1979).

64. T.J. Gray, P. Richard, G. Gealy, and J. Newcomb, Phys. Rev. A **19**, 1424 (1979).

65. H.L. Sun, J.F. Kirchhoff, A.R. Azordegan, J.L. Duggan, F.D. McDaniel, R.M. Wheeler, R.P. Chaturvedi, and G. Lapicki, Nucl. Instrum. Methods **B79**, 194 (1993).

66. H.L. Sun, J.F. Kirchhoff, A.R. Azordegan, J.L. Duggan, F.D. McDaniel, R.M. Wheeler, R.P. Chaturvedi, and G. Lapicki, Nucl. Instrum. Methods **B79**, 186 (1993).

67. D.K. Marble, Ph.D. thesis (University of North Texas, 1991) (unpublished).

68. D.L. Weathers, J.L. Duggan, R.B. Escue, and F.D. McDaniel, Nucl. Instrum. Mehtods **A303**, 69 (1991).

69. P. M. Kocur, J.L. Duggan, R. Mehta, J. Robbins, and F.D. McDaniel, IEEE Trans. Nucl. Sci. **NS-30**, 1580(1983).

70. H.A. Bethe and R.W. Jackiw, *Intermediate Quantum Mechanics*, (Benjamin/Cummings Co., Menlo Park, Ca, 1986) p. 243-253.

71. A. Messiah, *Quantum Mechanics*, Vols. I and II, (Wiley, New York, 1962), p.p. 832-844.

72. L.I. Schiff, *Quantum Mechanics*, 3rd ed., (McGraw-Hill, New York, 1968) p. 324.

73. G.S. Khandelwal, B.-H. Choi, and E. Merzbacher, At. Data Nucl. Data Tables **1**, 103 (1969).

74. B.-H. Choi, E. Merzbacher, and G.S. Khandelwal, At. Data **5**, 291 (1973).

75. R. Rice, G. Basbas, and F.D. McDaniel, At. Data Nucl. Data Tables **20**, 503 (1977).

76. J.C. Slater, Phys. Rev. **36**, 57 (1930).

77. J.D. Jackson and H. Schiff, Phys. Rev. **89**, 359 (1953).

78. R.M. May, Phys. Rev. **11**, 34 (1964).

79. J.S. Briggs, J. Phys. B. **10**, 3075 (1977).

80. R.M. Drisko, Ph. D. thesis (Carnegie Institute of Technology, 1955) (unpublished).

81. R. Shakeshaft and L. Spruch, Rev. Mod. Phys. V **51**, No. 2, 369 (1979).

82. Dž. Belkić, R. Gayet and A. Sallin, Phys. Rept. **56**, 279 (1979).

83. B.-H. Choi, Phys. Rev. A **4**, 1002 (1971).

84. J.M. Hansteen and O.P. Mosebekk, Phys. Rev. Lett. **29**, 1361 (1972).

85. J.C. Ashley, R.H. Ritchie, and W. Brandt, Phys. Rev. B **5**, 2323 (1972).

86. K.W. Hill and E. Merzbacher, Phys. Rev. A **9**, 156 (1974).

87. W. Brandt and G. Lapicki, Phys. Rev. A **10**, 474 (1974).

88. J.M. Hansteen and O.P. Mosebekk, Z. Physik. **234**, 281 (1970).

89. C.D. Lin and P. Richard, in *ADVANCES IN ATOMIC AND MOLECULAR PHYSICS*, edited by S.D. Bates and B. Bederson (Academic Press, New York, 1981), pp. 275-353.

90. R.K. Gardner, T.J. Gray, P. Richard, C. Schmiedekamp, K.A. Jamison, and J.M. Hall, Phys. Rev. A **19**, 1896 (1979).

91. J. Eichler and H. Narumi, Z. Phys. A **295**, 209 (1980).

92. J.F. Reading, A.L. Ford, G.L. Swafford, and A. Fitchard, Phys. Rev. A **20**, 130 (1979).

93. V.P. Shevelko, Z. Phys. A **287**, 19 (1978).

94. R. Shakeshaft, Phys. Rev. Lett. **44**, 442 (1980).

95. L. Kocbach, J.M. Hansteen, and R. Gundersen, Nucl. Instrum. Methods. **169**, 281 (1980).

96. J.D. Garcia, R.J. Fortner, T.M. Kavanagh, Rev. Mod. Phys. **45**, 111 (1973).

97. J.S. Hansen, Phys. Rev. A **8**, 822 (1973).

98. J.H. McGuire and P.Richard, Phys. Rev. A **8**, 1374 (1973).

99. J.H. McGuire, Phys. Rev. A **9**, 286 (1974).

100. J.H. McGuire and K. Omidvar, Phys. Rev. A **10**, 182 (1974).

101. J. Macek and K. Taulberg, Phys. Rev. Lett. **46**, 170 (1981).

102. H.D. Betz in *METHODS OF EXPERIMENTAL PHYSICS: ATOMIC PHYSICS, ACCELERATOR* edited by P. Richard, (Academic Press, New York, 1980), Vol. 17, pp. 73-148.

103. R.A. Mapleton, Proc. Phys. Soc. Lond. **83**, 895 (1964).

104. J.P. Coleman, *Case Studies in Atomic Collision Physics I*, edited by E. W. McDaniel and M.R.C. McDowell (North-Holland, Amsterdam, 1969) p.99.

105. L.H. Thomas, Proc. R. Soc. **114**, 561 (1927).

106. I.M. Cheshire, Proc. Phys. Soc. Lond. **82**, 113 (1963); *ibid.* **84**, 89 (1964).

107. C.D. Lin, S.C. Soong, and L.N. Tunnell, Phys. Rev. A **17**, 1646 (1978).

108. C.D. Lin and L.N. Tunnell, J. Phys. B **12**, L485 (1979).

109. C.D. Lin and L.N. Tunnell, Phys. Rev. A **22**, 76 (1980).

110 W. Fritsch and C.D. Lin, Phys. Rep. **202**, 1 (1991).

111. H.D. Betz, Rev. Mod. Phys. **44**, 465 (1972).

112. J.B. Marion and F.C. Young, *Nuclear and Atomic Reaction Analysis*, (John wiley, New York, 1968), pp. 41-46.

113. Y.D. Kim, Ph.D. thesis (University of North Texas, 1994) (unpublished).

114. R.G. Musket, Nucl. Instrum. Methods **B15**, 735 (1986).

115. WM. J. Veigele, At. Data Tables **5**, 51 (1973).

116. J.A. Maxwell, J.L. Campbell, and W.J. Teesdale, Nucl. Instrum. Methods **B43**, 218 (1989).

117. J.L. Campbell and P.L. McGhee, Nucl. Instrum. Methods **A248**, 393 (1986).

118. S.J. Cipolla and S.M. Watson, Nucl. Instrum. Methods **B10/11**, 946 (1985).

119. W.J. Gallagher and S. Cipolla, Nucl. Instrum. Methods **122**, 405 (1974).

120. E.-J. Kartunnen, H.-U. Freund, and R.W. Fink, Phys. Rev. A **4**, 1695 (1971).

121. D.D. Cohen, Nucl. Instrum. Methods **178**, 481 919800.

122. J.L. Campbell and L.A. McNelles, Nucl. Instrum. Methods **125**, 205 (1975).

123. W.N. Lennard and D. Phillips, Nucl. Instrum. Methods **166**, 521 (1979).

124. D.L. Weathers, J.L. Duggan, M.R. McNeir, Y.C. Yu, F.D. McDaniel, C.A. Quarles, H. Lehtihet, and D. Kahler, Nucl. Instr. and Methods B **56/57**, 964 (1991).

125. J. Pálinkás and B. Schlenk, Nucl. Instrum. Methods **169**, 493 (1980).

126. C.A. Quarles and L. Estep. IEEE Trans. Nucl. Sci. **NS-30**, 1518 (1983).

127. J.C. Altman, R. Ambrose, C.A. Quarles, and G.L. Westbook, Nucl. Instrum. Methods **B24/25**, 1028 (1987).

128. L. Estep and C.A. Quarles, Physica **C145**, 369 (1987).

129. L. Kissel, C.A. Quarles, and R.H. Pratt, Atom. Data Nucl. Data Tables **28** 381 (1983).

130. M.R. McNeir, Ph.D. thesis (University of North Texas, 1992) (unpublished).

131. F. Folkmann, C. Gaarde, T. Huus, and K. Kemp, Nucl. Instrum. Methods **116**, 487 (1974).

132. O. Benka, Nucl. Instr. Methods B**4**, 279 (1984).

133. S.J. Czuchlewski, J.R. Macdonald, and L.D. Ellsworth, Phys. Rev. A **11**, 1108 (1975).

134. D.K. Oslen, C.F. Moore, and P. Richard, Phys. Rev. A **7**, 1277 (1973).

135. D. Burch, N. Stolterfoht, D. Schneider, H. Wieman, and J.S. Risley, Phys. Rev. Lett. **32**, 1151 (1974).

136. L. Winters, J.R. Macdonald, M.D. Brown, T. Chiao, L.D. Ellsworth, and E.W. Pettus, Phys. Rev. A **8**, 1835 (1973).

137. H. Tawara, P. Richard, T.J. Gray, J.R. Macdonald, and R. Dillingham, Phys. Rev. A **19**, 2131 (1979).

138. J.R. Mowat, D.J. Pegg. R.S. Peterson, P.M. Griffin, and I.A. Sellin, Phys. Rev. Lett **29**, 1577 (1972).

139. J.R. Mowat, D.J. Pegg, R.S. Peterson, P.M. Griffin, and I.A. Sellin, Phys. Rev. A **9**, 644 (1974).

140. T.W. Tunnell, C. Can, and C.P. Bhalla, IEEE Trans. Nucl. Sci. **NS-26**, 1124 (1979).

141. W. Jitschin, in *X-ray and Atomic Inner-Shell Physics - 1982*, edited by B. Crasemann, (American Institute of Physics, 1982), pp. 74-84.

142. W.K. Chu, J.W. Mayer, and M.-A. Nicolet, *Backscattering Spectrometry* (Academic Press, New York, 1978).

143. H.H. Andersen, F. Besenbacher, P. Loftager, and W. Möller, Phys. Rev. A **21**, 1891 (1980).

144. M. Bozoian, K.M. Hubbard, and M. Nastasi, Nucl. Instrum. Methods, **B51**, 311 (1990).

145. M. Bozoian, Nucl. Instrum. Methods. **B56/57**, 740 (1991).

146. I.A. Sellin, Adv. At. Mol. Phys. **12**, 215 (1977).

147. C.D. Lin, W.R. Johnson, and A. Dalgarno, Phys. Rev. A **15**, 154 (1977).

148. D.R. Bates and G.W. Griffing, Proc. Phys. Soc. London **66A**, 961 (1953).

149. J.S. Briggs and K. Taulbjerg, in *Structure and Collisions of Ions and Atoms*, edited by I.A. Sellin, (Springer Verlag, Heidelberg, 1978) p. 105.

150. J.H. McGuire, N. Stolterfoht, P.R. Simony, Phys. Rev. A **24**, 97 (1981).

151. A. Tanis, E.M. Bernstein, W.G. Graham, M.P. Stöckli, M. Clark, R.H. McFarland, T.J. Morgan, K.H. Berkner, A.S. Schlachter, and J.W. Stearns, Phys. Rev. Lett. **53**, 2551 (1984).

152. L.H. Anderson, M. Frost, P. Hvelplund, H. Knudsen, and S. Date, Phys. Rev. Lett. **52**, 518 (1984).

153. N. Stolterfoht, C.C. Havener, R.A. Phaneuf, J.K. Swenson, S.M. Shafroth, and F.W. Meyer, Phys. Rev. Lett. **57**, 74 (1986).

154. J.F. Reading and A.L. Ford, Phys. Rev. Lett. **58**, 543 (1987).

155. F.W. Meyer, D.C. Griffin, C.C. Havener, M.S. Huq, R.A. Phaneuf, J.K. Swenson, and N. Stolterfoht, Phys. Rev. Lett. **60**, 1821 (1988).

156. T.J. Gray in *Methods of Experimental Physics*, edited by P. Richard (Academic, New York, 1980) Vol. **17**, p. 193.